POLITECNICO DI TORINO

Dottorato di Ricerca in Fisica
XXVII Ciclo

TESI DI DOTTORATO

FIRST experiment: measurements of differential cross sections in ^{12}C fragmentation for hadrontherapy and space applications.

Candidata
FRANCESCA BALESTRA

Tutor
PROFESSOR FELICE IAZZI

2012 − 2014

FACOLTÁ DI APPARTENENZA:
INGEGNERIA DEL POLITECNICO DI TORINO

DIPARTIMENTO:
DISAT (DIpartimento di Scienza Applicata e Tecnologia)

SETTORE DISCIPLINARE:
FIS/01

To Riccardo,
my rock and my love.

Contents

Summary

The aim of the present work is to describe some preliminary results obtained within the experiment FIRST (Fragmentation of Ions Relevant for Space and Therapy).

This experiment main goal is to measure the differential cross-sections in energy and angle of nuclear fragmentation processes, in a wide energy range (between 100 and 1000 MeV/n). The knowledge of these cross sections will be useful for cancer therapy and space radiation protection. This experiment was carried out because there is a strong need of high-quality experimental data concerning ^{12}C, ^{16}O and ^{56}Fe fragmentation on different targets.

The first data taking has been performed at SIS (Heavy Ion Synchrotron) accelerator of GSI Laboratory in Darmstadt (Germany) during August 2011. Different sets of data have been collected using a 400 MeV/n carbon beam impinging on carbon and gold targets.

Experimental data of single and double-differential cross sections for C-ions at energies less or equal to 400 MeV/n are needed to improve treatment plannings in particle-therapy. In particular accurate measurements of cross sections of light ions are urgently needed for improving transport codes to be used in cancer therapy. Algorithms that deal with the transport of charged particle in matter are essential for accurate treatment plannings, in order to evaluate possible long term side effects of dose released in healthy tissue. Unfortunately, the production of light fragments and their angular distributions are affected by large uncertainties and various Monte Carlo codes may differ up to one order of magnitude in their predictions.

Moreover, codes used for space radiation transport in shielding materials need more information on the fragmentation effects. Recently, NASA completed a large database of these measurements and observed that there are ion species and kinetic energy ranges not yet evaluated.

The FIRST experiment aims to contribute to the knowledge of these nuclear processes and to investigate the secondary effects on human tissues of hadron's irradiation. In fact, most of the measurements carried out in the past are limited to fragment yields and to total fragmentation cross-sections,

while the required measurements of single or double-differential cross-sections are deficient.

Hadron-therapy is, at present, a valid alternative to radiotherapy in cancer treatment. Protons and carbon ions have been used for treating many different solid cancers. High-energy beams of charged nuclear particles (protons and heavier ions) in fact, offer significant advantages for the treatment of deeply-seated local tumors, in comparison to conventional mega-volt radiation-therapy. A detailed description of the hadron-therapy technique, together with its advantages with respect to radiation-therapy, is given in chapter 1. In the same chapter, an illustration of the risks due to radiation effects, on people and equipments, during space missions can be found, as well as the improvements that an experiment like FIRST can produce in this field.

Chapter 2 contains the description of the whole FIRST experimental setup and of all the sub-detectors.

Chapter 3 is dedicated to a particular detector, the ToF-Wall (Time of Flight Wall), which is fundamental for retrieving the most important information concerning the fragments: time of flight, impact point horizontal and vertical coordinates and energy release in the detector (from which information about the fragment charge can be obtained). In this chapter are described the ToF-Wall efficiency and calibration processes together with the fragment charge identification algorithm and some preliminary results on scattered carbon particles.

In chapter 4 and 5 the Monte Carlo codes and the tracking algorithms, developed within the FIRST collaboration, fundamental for the achievement of the experiment results, are illustrated minutely.

Chapter 6 describes some preliminary but important results obtained, on the cross sections, by the FIRST collaboration.

Finally, in chapter 7, the conclusions, summarizing the results of the FIRST experiment, are given.

Chapter 1

Introduction

1.1 Hadrontherapy

Cancer is, nowadays, one of the most fatal diseases worldwide. It is characterized by alterations in the expression of multiple genes, leading to a not regular cellular program for cell division and differentiation. This results in an imbalance of cell replication and cell death that favors the growth of a tumor cell population. These ill cells can invade tissues and metastasize to distant sites, causing significant morbidity and, if untreated, death of the host.

Cancer can be caused by several factors both external (tobacco, radiations, viruses) and internal (inherited or metabolism produced mutations, hormones, immune conditions).

Worldwide, one in eight deaths is due to cancer; grouping countries according to economic development, cancer is the leading cause of death in developed countries and the second leading cause of death in developing countries (following heart diseases) as described in table 1.1 [1]. According to estimates from the International Agency for Research on Cancer (IARC[1]), in 2008 only, there were 12.7 million new cancer cases worldwide, of which 5.6 million occurred in economically developed and 7.1 million in economically developing countries. The corresponding estimates for total cancer deaths were 7.6 million: 2.8 million in economically developed countries and 4.8 million in economically developing countries.

By 2030, the global burden is expected to grow to 21.4 million new cancer cases and 13.2 million cancer deaths.

Therefore, the development of innovative medical treatments able to fight

---

[1]In appendix 1, a list of the acronyms used in this work is given, in alphabetical order, together with their meaning.

Table 1.1: Leading causes of death worldwide and in developing and developed countries, 2004 (thousands) [1].

	Worldwide			Developing			Developed		
	Rank	Deaths	%	Rank	Deaths	%	Rank	Deaths	%
Heart diseases	1	8,923	15.1	1	7,342	14.5	2	1,563	19.3
Malignant neoplasms	2	7,424	12.6	2	5,255	10.4	1	2,154	26.6
Cerebrovascular diseases	3	5,712	9.7	3	4,949	9.8	3	757	9.4
Lower respiratory infections	4	4,177	7.1	4	3,910	7.7	4	305	3.8
Perinatal conditions*	5	3,180	5.4	5	3,141	6.2		35	0.4
Chronic obstructive pulmonary disease	6	3,025	5.1	6	2,737	5.4	5	285	3.5
Diarrhoeal diseases	7	2,163	3.7	7	2,148	4.2		14	0.2
HIV/AIDS	8	2,040	3.5	8	2,018	4.0		20	0.2
Tuberculosis	9	1,464	2.5	9	1,448	2.9		15	0.2
Road traffic accidents	10	1,275	2.2	10	1,158	2.3		114	1.4
Diabetes mellitus	11	1,141	1.9		914	1.8	7	221	2.7
Malaria	12	889	1.5		888	1.8		0	0.0
Suicide	13	844	1.4		707	1.4	9	118	1.5
Cirrohsis of the liver	14	772	1.3		655	1.3	10	116	1.4
Nephritis and nephrosis	15	739	1.3		611	1.2	8	126	1.6
All causes		58,772	100.0		50,582	100.0		8,095	100.0

The number zero in a cell indicates a non-zero estimate of less than 500.

* Includes "causes arising in the perinatal period" as defined in the International Classification of Diseases, principally low birthweight, prematurity, birth asphyxia, and birth trauma, and does not include all causes of deaths occurring in the perinatal period.

Source: World Health Organization, The global burden of disease: 2004 update.

this dangerous disease is a "state of the art" research field.

The aim of a cancer therapy is to destroy the tumor cells while preserving as much as possible the healthy tissues. Unfortunately, all the therapies developed until now (chemotherapy, surgery, X-ray therapy and also particle beam therapy) induce collateral damages; however radiation therapy can be considered the most effective and cost effective treatment modality for all types of solid malignancies.

It is estimated that about 45% of the cancer patients can be cured. The radiation therapy contributes in curing around 23% of all the patients affected by cancer: 12% if used alone, 6% in combination with surgery and 5% in combination with chemotherapy-immunotherapy. Therefore, about 50% of the cancer patients cured with radiation therapy benefit from it [2].

History has shown that the major improvements in the efficacy of radiation therapy were always associated with significant progress in technology: the improvements in the physical selectivity, from X-rays to ^{60}Co and high energy

linear accelerators together with more effective diagnostic tools and radiation delivery methods have continuously improved the results of this kind of therapy [3, 4].

1.1.1   History and evolution of hadrontherapy

The history of hadrontherapy is long and can be divided in different temporal periods or "eras".

It begins with the X-rays discovery [5], in 1895, by Wilhelm Conrad Röntgen. Shortly after this discovery, in the first few months of 1896, X-rays were being used to treat skin lesions (prior to any understanding of the beam physical or biological effects).
Again in 1896, Antoine Henri Becquerel discovered radioactivity and in 1898 and 1902, Marie and Pierre Curie identified two new radioactive elements Polonium and Radium. These discoveries introduced the idea that radioactivity could be also used to treat diseases; the so called "Curietherapy", a form of radiotherapy where a small, encapsulated radionuclide source is placed inside or next to the area requiring treatment (nowadays referred to as brachytherapy) was invented.
However, the lack of knowledge of the biological effects and mechanisms of actions of the new phenomena (radioactivity and X-rays) led to much morbidity and poor cancer control. This first period, lasting the early 1920's, can be referred to as the "discovery era". In this era, the radiation therapy remained an empirical science. Nevertheless, two main features begun to be understood: the clinical results were improved by a greater conformity of the applied radiation to the target volume and by an increased biological effectiveness of the radiation.

During the 1920's, the invention of a sealed-off vacuum X-ray tube able to operate at energies of $180 - 200$ keV, by W.D.Coolidge [6], started a new era in the radiation treatments: the "kilovoltage era". Unfortunately, the X-rays generated by the new machine were fairly soft. This, from the medical point of view, was actually disadvantageous since the maximum dose would be delivered at the skin surface and then would rapidly fall off with the depth in the tissue. In this era, generally, the physical limitations of dose distribution severely prevented the developing of radiotherapy, since, with energies between 50 keV and 200 keV, it was very difficult to deliver sufficient doses into deep-seated tumours, mainly due to the associated unavoidable skin toxicity.
It became clear that higher energy beams were necessary.
One of the most important developments in radiotherapy was the invention, by R. Van de Graaff, of a high voltage accelerator [7] in 1932. In 1937, the

first hospital-based accelerator of this type, a 1 MeV air-insulated machine, was installed in Boston.

Starting from the 1940's, new ideas for higher energy devices, such as the megavoltage linear electron accelerators, begun to circulate giving rise to the "megavoltage era". In 1943, thanks to the development of the betatron, by D.W. Kerst [8], the high energy X-rays and electron beam therapy became feasible. Betatrons were widely used till 1970's when their application started to diminish due to some drawbacks like the relatively low intensity of the X-ray beams produced, the small treatment field area and their relevant weight. In the meanwhile, new developments in Physics and Engineering opened the possibility to use microwave generators for electron acceleration and, as a consequence, to the birth of the first radio-frequency linear accelerators designed by C.W. Miller [9], destined to become the prevalent ones on the world market of medical accelerators.

Nowadays, the sources of radiation for modern radiotherapy with collimated beams are the electron LINear ACcelerators (LINAC). Such accelerators are capable of producing both electron and photon beams with energy varying between 3 and 25 MeV. The first kind of particles is effective in the treatment of on-surface or semi-deep tumors, while the photon beams can be applied for a very efficient treatment of tumors situated at a depth of many centimeters inside the body with respect to the skin surface.

However, some tumors ("radioresistant tumors") that are not affected by photon treatments exist. Moreover, sometimes even non-radioresistant tumors, located near critical body parts, can not be given a tumorocidal dose because of the unavoidable dose to the surrounding normal tissues. In this context, the searching of an increased biological effectiveness drove to the idea of using different kinds of particles like neutrons, protons and other ions. The "hadrontherapy" was born.

The first attempt to use hadrons was performed, in the 1930's, using fast (with kinetic energy of few tens of MeV) neutrons. This was possible thanks to the invention of the cyclotron, by Ernest Lawrence and Stanley Livingston in 1930 [10]. Neutrons act through scattering onto ions, which are mainly protons in biological tissues. These ions are ejected from their molecule at low energy: as a consequence the neutrons produce a greater biological damage with respect to photons. Unfortunately, a poor depth dose profile compensates the increased biological effectiveness of neutrons producing severe late effects in normal tissues. For this reason neutron therapy did not develop and also nowadays it is mostly restricted, in some laboratories, for the treatment of radio resistant tumors of the salivary glands.

The application of high-energy beams of heavy charged particles to radiotherapy was first considered by Robert R. Wilson, who in 1946, proposed that

accelerated protons could be used for localized cancer therapy [11], thanks to their favorable tissue depth–dose distribution [12]. Charged particles deposit little energy at the body's surface, when their velocity is high, and instead deposit most of their energy just before they come to rest. This release of energy is termed the Bragg peak (see figure 1.1). Due to the Bragg peak, the dose can be concentrated on the tumor target sparing healthy tissues better than what can be done with X-rays. In fact, the X-rays release their energy inside the tissue in an exponential way (see figure 1.3) making them situable only for curing skin tumors.

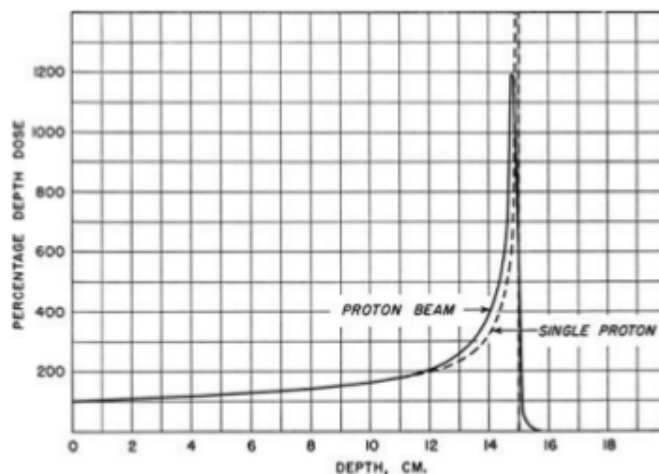The cancer therapy with heavy ions started later, in the 1970's in Berkeley,

Figure 1.1: The original picture from Robert R. Wilsons paper on proton-therapy [11].

where Cornelius A. Tobias proposed that particles heavier than protons could give additional advantages [13]. Heavy ions have reduced lateral scattering compared with protons, which leads to a further improvement in the dose distribution to the target area. Moreover, the main potential advantages of heavy ions are in their radio-biological effects on tissues [14]. Several different charged particles, He, Ar, Si, Ne, were tried to improve the effectiveness, in particular, against radioresistant tumors. However, problems arose owing to non-tolerable side effects in the normal, healthy tissues.

Only in the early 1990's carbon ions were recognized as the optimal ion choice. In fact their effects in the tissue entrance are similar to those of X-rays and protons, while just at the end of their path in matter, ionization density is definitely larger and not repairable damages are produced to the cellular systems.

It has to be remarked that the first hadrontherapy treatments were performed by means of particle accelerators that had originally been built for nuclear physics experiments and were then adapted to tumor therapy. This was the case in Berkeley. As far as all the treatment facilities were located in physics laboratories, the irradiation condition was far from ideal. Although many times it was felt that hadrontherapy field could not develop without dedicated equipment, this step took almost 20 years. The first hospital-based centre was built at the Loma Linda University Center (California), which signed an agreement with Fermilab (founded and directed for many years by Robert Wilson) and treated the first patient in 1990.

In 1994 the Heavy Ion Medical Accelerator (HIMAC) dedicated to radiotherapy started treatments with carbon ions at National Institute of Radiological Science (NIRS) in Chiba (Japan) [15]. By the end of 2007 more than 4000 patients have been treated at the HIMAC facility showing that, among light ions, a better tumor control rate can be achieved with carbons.

At the same time, new technical solutions were developed almost in parallel at the Gesellschaft für SchwerIonenforschung (GSI) in Darmstadt, Germany. Here a new concept was developed, differing significantly from the previous designs (HIMAC): moving a narrow pencil beam slice by slice over the target volume (raster scan) a tumor conform treatment can be achieved to a high degree, restricting the biologically most effective ions to the target volume and minimizing the dose to the surrounding normal tissue [16].

Up to now (December 2013), more than 120000 patients have been treated worldwide [17]. New facilities are under construction and more technologies are developed everyday for new accurate delivery of the dose to the patient.

1.1.2 Physical and biological aspects of oncology therapy with ion beams

Dose and therapeutic ratio

The fundamental aim in radiation oncology is the local control of the tumor. In order to achieve this important result, it is necessary to deliver to the tumor region a dose high enough to destroy it but, at the same time, the dose deposited in surrounding healthy tissues must be the lower possible.

The dose deposited in tissues is the most important physical quantity in radiotherapy. The definition of the absorbed dose D in a mass element dm is found in [18]:

$$D = \frac{d\epsilon}{dm} \tag{1.1}$$

where $d\epsilon$ is the mean energy imparted by ionizing radiation to the elementary piece of matter dm.

The absorbed dose is measured in Gray (Gy): 1 Gy= 1 J/kg, i.e. the absorbed energy of 1 Joule in 1 kilogram of matter.

A typical radiation regimen for a localized solid cancer consists of 60-70 Gy delivered to the tumor in 30-35 daily fractions of 2 Gy over 6-7 weeks [19].

To evaluate the probability of tumor local control, the so called "dose-effect curves" are used by radiotherapists. An example of "dose-effect curves" is given in figure 1.2. These sigmoid curves have different meanings if referred
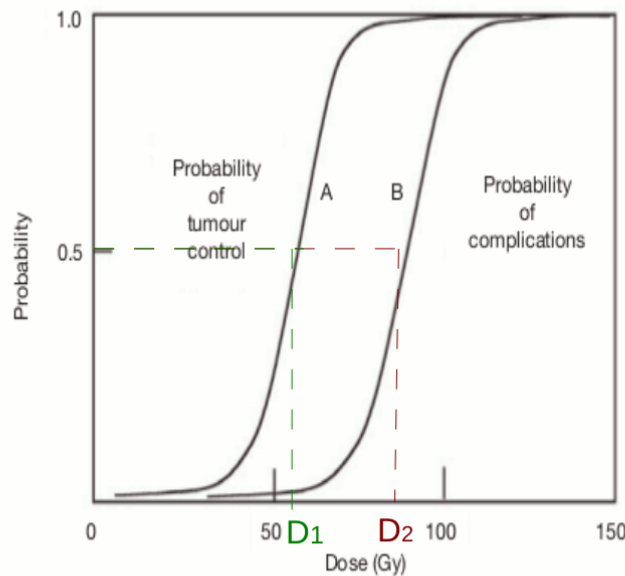
Figure 1.2: Hypothetical dose-effect curves for neoplastic, i.e. tumoral (A) and normal (B) tissues.

to tumor or healthy tissues: for tumor tissue, they describe the possibility of obtaining the desired effect as a function of the delivered dose and are called TCP, Tumor Control Probability; for healthy tissues, instead, they represent the probability of producing serious or irreversible damage, always as a function of the absorbed dose by the same tissue; in this case they are called NTCP, Normal Tissue Complication Probability [20]. From figure 1.2, it is clear that the absorbed dose necessary to achieve a probability close to 100% of obtaining local control of the tumor corresponds also to a very high probability of producing serious complications in the healthy tissue. Therefore,

in practice, it is necessary to reach a compromise between the possible onset of complications and the tumor local control: the possibility to find such a compromise can be expressed quantitatively by the therapeutic ratio, i.e. the ratio D_2/D_1 (shown in figure 1.2) between the dose corresponding to a 50% probability of producing complications, D_2 and the dose corresponding to a 50% probability of obtaining the local control of the tumor, D_1 [21].

The best choice in the radiation dose delivery technique is, of course, the maximization of TCP and the simultaneous minimization of the NTPC. Typically, in good radiotherapy treatments, TCP$\geq$0.5 and NTPC$\leq$0.05.

The curves described in figure 1.2 are ideals; in reality, the therapeutic ratio varies with many factors, such as the dose rate and the Linear Energy Transfer (LET, see Section 1.1.2) of the irradiation, the presence of radiosensitizers or radioprotectors, the design of the treatment plan and the precision of implementation of the treatment plan.

The stopping power of ions in matter:
the inverse depth-dose profile and the spread out Bragg peak

As outlined in the previous section, one of the most important reason in the use of charged particles in hadrontherapy is their inverse dose profile, that is the increase in the energy deposition in tissues with the penetration depth. This phenomenon was firstly described by W. H. Bragg in 1905 [22], for α particles in air; for this reason the depth-dose profiles are also known as "Bragg curves".

A comparison of depth-dose profiles for electromagnetic radiation (X-rays and megavolt photon beams) and carbon ion beams is displayed in figure 1.3 [23].

In the figure, it can be seen that the behaviors in the depth-dose profiles are different for the photons and the charged ions; this is due to the peculiar physical processes, which characterize respectively electromagnetic radiation and charged particle interaction with matter.

The photon interaction with matter acts through three processes: photoelectric effect, Compton scattering and pair (e^- – e^+) production. The relative probability of each of these interaction mechanisms is a function of the incident photon energy and the atomic number Z of the absorbing material. In figure 1.3, it is possible to see that for low-energy photons the stochastic absorption due to photoelectric and Compton processes yields an exponential decay of absorbed dose with penetration depth and the beam doesn't show a path of finite lenght. For higher photon energies, the produced Compton electrons are strongly forwardly scattered and transport some of the transferred energy from the surface to deeper layers, yielding an increase in dose in
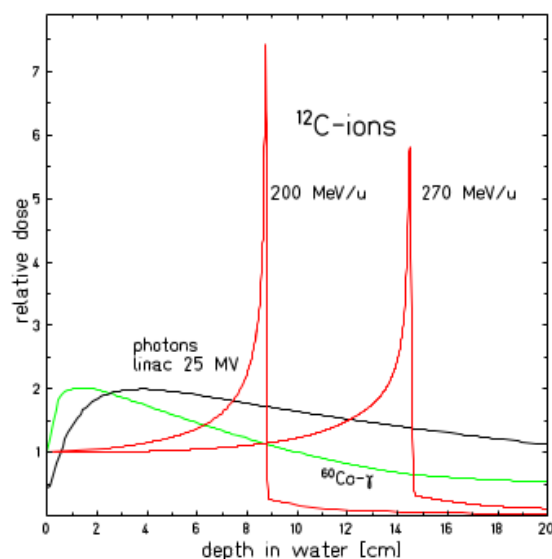
Figure 1.3: Depth-dose profiles of low energy γ rays from ^{60}Co, high energy photons from LINAC at 25 MV and ^{12}C ions at different energies (200 and 270 MeV/u) in water [23].

the first few centimeters. For high energy bremsstrahlung radiation, mostly used in conventional therapy, this maximum is shifted a few centimeters from the surface of the patient body, improving the target-to-entrance dose and sparing the very radiosensitive skin.

Charged particles, instead, mainly dissipate their energy trough interaction with the target material electrons (emitted as δ electrons). The interaction strength is proportional to the interaction time, therefore, at high velocities the energy transfer to the target is small but grows when the particles are slowed down. The rate of average energy loss per unit path length for a given target medium increases with decreasing particle velocity, giving rise to a sharp maximum in ionization near the end of the range. Thus the depth-dose distribution is characterized by a relatively low dose in the entrance region (plateau) near the skin and a sharply elevated dose at the end of the range (Bragg peak). The Bragg peak position is energy dependent; this is a further advantage as the peak position can be precisely adjusted to the desired depth in tissue by changing the kinetic energy of the incident ions. As a consequence, in the healthy tissues surrounding the Bragg peak region of deposition, the dose released is minimized with respect to the target volume. However, it must be underlined that, from the practical applications point of view, a monoenergetic beam creates a Bragg peak very narrow, able to irra-

diate a very small and localized region within the body. Indeed, the tumor volume to be treated is normally much larger than the width of the Bragg peak and the lateral spot of the particle beam. To overcome this problem, it is necessary to spread-out the Bragg peak in the longitudinal direction. This is achieved by superimposing several Bragg peaks at different depths obtained by suitably selecting the projectile energy distributions. The result, shown in figure 1.4, is the so called "Spread Out Bragg Peak" (SOBP), an "extended" Bragg peak area which has to accurately overlap the target volume.

The final dose distribution allows tumor conform treatments of enhanced quality with respect to those obtained by applying photons [24].
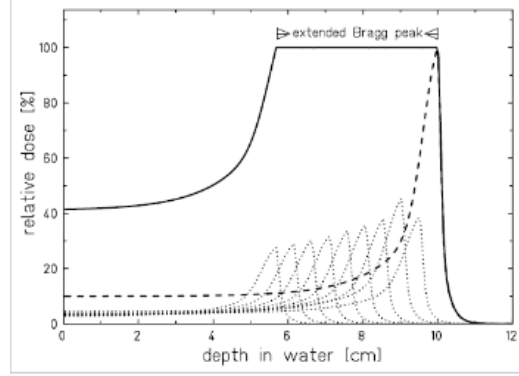
Figure 1.4: Construction of an extended Bragg peak by superposition of single Bragg peaks of different energy [24].

For deep–seated tumor therapy, ion beam ranges in tissues up to 30 cm are needed, corresponding to specific energies of ≈ 220 MeV/n for protons and helium ions, ≈ 430 MeV /n for carbons and ≈ 600 MeV/n for neon ions with particle velocities $\beta \equiv \frac{v}{c} \simeq 0.7$ [23]. The slowing down process, at these velocities, is dominated by inelastic collisions with the target electrons (electronic stopping power), therefore the energy released per unit length $\frac{dE}{dx}$ can be described by the Bethe-Bloch formula[2] [25, 26] here reported in the relativistic version [27], including the density effect correction term $\frac{\delta}{2}$:

$$\frac{dE}{dx} = k * \rho * \frac{Z_p^2}{\beta^2} * \frac{Z_t}{A} * [\frac{1}{2}ln(\frac{2m_e c^2 * \beta^2 * \gamma^2 * T_{max}}{<I>^2}) - \beta^2 - \frac{\delta}{2}] \qquad (1.2)$$

---

[2]A description on how the Bethe-Bloch formula has been obtained is given in appendix 2, considering only the non-relativistic case.

$k = 4\pi N_{Av} r_e^2 m_e c^2$ contains only universal constants: m_e is the mass of the electron, N_{Av} is the Avogadro's number, $r_e = \frac{e^2}{4\pi\epsilon_0 m_e c^2}$ is the classical electron radius in which e is the electron charge. Z_p and Z_t denote the nuclear charges of the projectile and target, $< I >$ is the mean ionization energy of the target atom or molecule and $T_{max} = \frac{2m_e c^2 * \beta^2 * \gamma^2}{1 + \frac{2\gamma m_e}{M} + (\frac{m_e}{M})^2}$ is the maximum energy transfer in a single collision during the energy loss, M is the mass of the incident particle.

The energy loss depends on the factor $\frac{1}{\beta^2}$ therefore it increases with decreasing particle energy.

At high velocities (in the relativistic energy domain) the atomic electrons are completely stripped off and the projectile charge is equal to the atomic charge number.

At lower velocities – non-relativistic energies (for light ions below ~ 10 MeV/n) – the mean charge state decreases due to the interplay of ionization and recombination processes. In this case Z_p has to be replaced by the effective charge Z_{eff}, which can be described by the Barkas empirical formula [28]:

$$Z_{eff} = Z_p[1 - exp(-125\beta Z_p^{-2/3})] \qquad (1.3)$$

Considering these dependencies, the energy loss rate grows up as the kinetic energy of the projectile decreases along the penetration depth, particularly in the last few millimetres of the particle path where it shows a much steeper rise. For this reason the distribution of the ionizing density produced by the charged particle along the track is characterized by a rather constant plateau, followed by a sharp maximum towards the end, where gives rise to the Bragg peak. At the end of the path, the stopping power drops quickly to zero because of the rapid reduction of the effective charge Z_{eff} for very low energy values.

The Bragg peak is reached when the projectile velocity v reaches a specific value, given by:

$$v = Z_p^{2/3} v_0 \equiv v_p \qquad (1.4)$$

where $v_0 = e^2/\hbar$ is the Bohr velocity.

The maximum energy loss rate corresponding to the Bragg peak, for ^{12}C ions, occurs at a specific energy: $E_p \approx 0.35$ MeV/n [23].

At still lower projectile energies ($E_p \leq 0.10$ MeV/n) elastic collisions with target nuclei begin to contribute significantly to the energy loss and dominate the stopping process at the very end of the particle path (the last few μm). This mechanism of ion energy loss is commonly called nuclear stopping power. However, the dose contribution associated to this last phenomenon is very small and can be neglected in radiotherapy applications [29].

Range straggling and lateral beam spread

If the stopping power is known, it is possible to calculate the distance that a charged particle travels inside a medium, before stopping: the range R.

$$R(E_0) = \int_0^{E_0} (\frac{dE}{dx})^{-1} dE \qquad (1.5)$$

being E_0 the ion incident energy.

This definition, for heavy charged projectiles, is nearly the same as the mean range R, i.e., the average traversed absorber thickness, because heavy ions are very little scattered and travel almost on a straight line.

In figure 1.5, ranges of different ion beams in water are shown. The range,
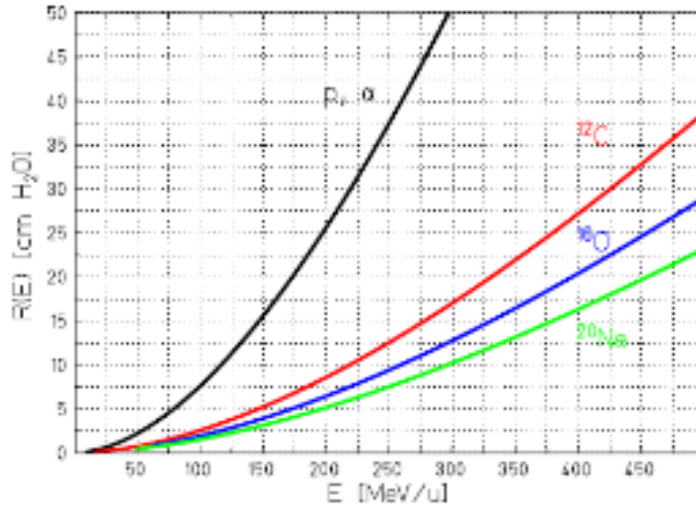
Figure 1.5: Mean range of heavy ions in water [30].

for particles with the same energy per nucleon, scales with a factor A/Z^2 (A and Z are the ion mass and atomic number).

According to the Bethe-Bloch formula 1.2, the energy loss of a single carbon ion plotted as a function of the absorber depth would result in a very sharp peak near the stopping point. However, statistical fluctuations of the energy loss, ΔE (energy loss straggling), due to the large number of collisions of the slowing-down process, cause a broadening of the Bragg peak for an ion beam consisting of many particles. These fluctuations are the cause of a dispersion of the path length, which is called "range straggling".

They are described, for charged particles passing through thin layers, by the

asymmetric Vavilov distribution [31], which in the limit of many collisions can be approximated by a Gaussian expression [32]:

$$f(\Delta E) = \frac{1}{\sqrt{2\pi}\sigma}e^{\frac{(\Delta E - <\Delta E>)^2}{2\sigma^2}} \qquad (1.6)$$

σ is the straggling parameter and expresses the half width at the height $1/e$; $<\Delta E>$ represents the mean energy loss by a charged particle into a thin layer.

The statistical fluctuations of energy loss, therefore, produce a smearing of the stopping range of the particle beam and, consequently, a larger width of the Bragg peak experimentally measured.

Range straggling effects for ion beams vary approximately with $\frac{1}{\sqrt{A}}$ and increase as the penetration depth grows up.

The lateral beam spread is mainly due to elastic Coulomb interactions with the target nuclei. Numerous small angle deflections in an ion beam lead to lateral spreading of the incident ions away from the central trajectory, resulting in larger divergence of the beam.

The angular distribution of the scattered particles is roughly Gaussian for small deflection angles, and the mean beam deflection is approximately proportional to the penetration depth. The Coulomb scattering of the projectiles is described very precisely in the Molière theory [33, 34]. A thorough analysis of a large set of proton beam spread data obtained over many years at the Harvard proton therapy center [35] was found to be in very good agreement with the Molière theory. From these studies, a parametrization for the angular distribution f(α) when the scattering angle α is small, was found:

$$f(\alpha) = \frac{1}{\sqrt{2\pi}\sigma_\alpha}e^{-\frac{\alpha^2}{2\sigma_\alpha}} \qquad (1.7)$$

where σ_α is the standard deviation of the distribution, given by:

$$\sigma_\alpha = \frac{14.1\ MeV}{\beta pc}Z_p\sqrt{\frac{d}{L_{rad}}}(1 + \frac{1}{9}log_{10}(\frac{d}{L_{rad}})) \qquad (1.8)$$

p is the momentum (in MeV) while L_{rad} is the radiation length in the absorber and d is the absorber thickness. Values of L_{rad} for common materials can be found in [36].

Targets containing heavy elements cause a larger angular spread than targets of light elements with the same thickness (in units of g/cm^2).

Figure 1.6 represents the beam spread for carbon ions and protons calculated for a typical treatment beam line. From the figure 1.6 that shows a
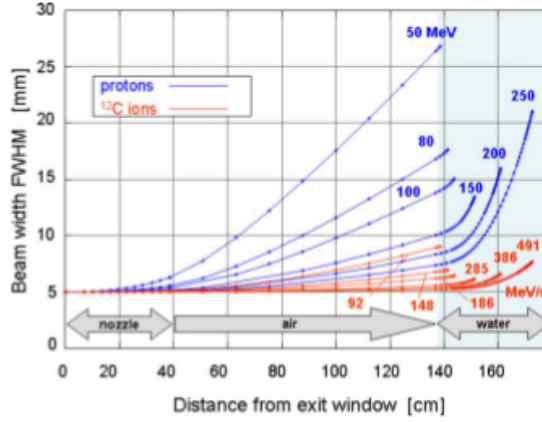
Figure 1.6: Calculated beam spread for ^{12}C ions and protons in a typical beam line for medical treatments [23].

comparison of beams with the same range in water (150 MeV protons and 285 MeV/n ^{12}C ions with R = 15.6 cm) it is possible to see that the angular spread (σ_α) for protons is more than three times larger than that for ^{12}C ions. This fact represents a further advantage of the clinical use of carbon ion beams and it contributes to an enhanced ballistic precision.

The small lateral deflection of heavy ions penetrating through an absorber is a particular advantage of heavy ions in comparison to protons and is of clinical relevance for treatments near Organs At Risk (OAR).

Radiation damage and linear energy transfer

The photon and heavy ion release of energy inside matter is strongly different.

Photons transfer their energy to the target cells either by Compton effect only or by Compton effect together with photoelectric effect, according to their initial energy. Because of the low cross sections of both effects, however, the number of ionization events per incident photon within the volume of a cell is small. Hence many photons are required in order to deliver a relevant dose. In both the cases, moreover, mostly due to multiple Compton scattering, the photons are scattered into randomly distributed directions. Therefore, the resulting ionization density can be assumed as uniform over the entire cell volume. In this way the ionization density results to be small, since it is not concentrated in a small part of the volume of the cell. Consequently the produced lesions are soft and hence easily reparable. As a consequence, photons are referred to as sparsely ionizing radiation.

Heavy ions, instead, create a energy distribution in space more localized

that leads to a larger biological effect. For an incident charged particle, the ionization occurs along its trajectory and most of the energy loss is transferred to the liberated electrons, which form a kind of "electron cloud" along the path of the primary ion: the ion track [37]. It is the action of these secondary electrons that determines the biological response, together with the primary ionization. The higher electron-density, and consequently the ionization-density, yields a larger biological effectiveness. For this reason, heavy ions are called densely ionizing radiation.

The principal target of the radiation attack is the DNA inside cellular nuclei. The Deoxyribonucleic acid (DNA) is a molecule that encodes the genetic instructions used in the development and functioning of all known living organisms; therefore its integrity is fundamental for cell (and whole organism) survival. DNA is strongly protected by an extremely elaborate repair system so that DNA violations like Single Strand Breaks (SSB) or Double Strand Breaks (DSB) can be rapidly restored. However, if DNA is exposed to very high local doses (local refers to the scale of a few nanometres) the DNA lesions become concentrated or clustered and repair system fails to correct the damages (see figure 1.7). The higher density of the secondary electrons produced by heavy ions (carbon ions among them), creates a large amount of clustered DNA damages resulting in a high biological effectiveness [38].
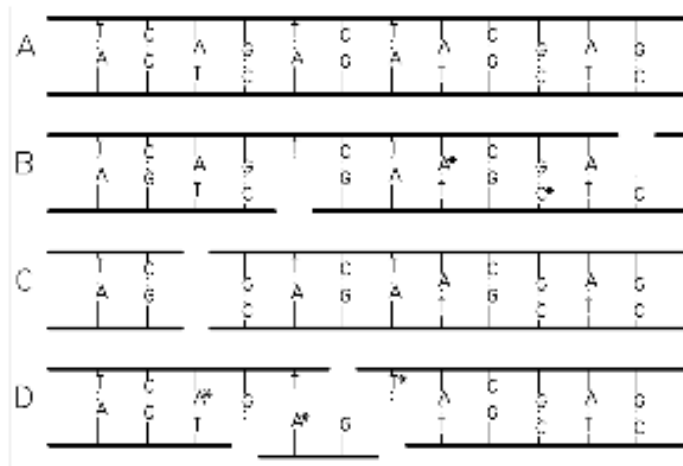

Figure 1.7: Schematic view of an undamaged part of DNA (A), two separated single strand breaks (B), a double strand break (C), and a clustered lesion (D). The (*) indicate a base damage [24].

The quantity that represents the energy deposition along particle tracks

Table 1.2: LET values for different ion species at different residual ranges. The energies of column 2 correspond to a range of 262 mm in water. The values 262 150 70 30 1 in line 2, above the LET (keV/μm) columns, refer to the distance between the ion position during its path into the water and the stopping point [38].

Charged particle $^A_N^Z$	Energy(AMeV) Range = 262 mm	LET (keV/μm)				
		262	150	70	30	1
^{1}H^{+1}	200.0	0.5	0.6	0.8	1.1	4.8
^{4}He^{+2}	202.0	1.8	2.2	3.1	4.4	20.0
^{7}Li^{+3}	234.3	3.7	4.6	6.2	8.9	40.0
^{11}B^{+5}	329.5	8.5	10.0	13.5	19.0	87.5
^{12}C^{+6}	390.7	11.0	13.5	17.5	24.5	112.0
^{14}N^{+7}	430.5	14.5	17.5	22.5	31.5	142.0
^{12}O^{+8}	468.0	18.0	21.5	28.0	39.0	175.0

in tissue is the Linear Energy Transfer (LET). It is defined as the ratio between the energy dE deposited by a charged particle in a track element and its length dx; it is measured in keV/μm.

If only single collisions, with energy deposition limited to a specific value Δ, are considered, the LET is defined as restricted LET and is described as:

$$L_\Delta = (\frac{dE}{dx})_\Delta \tag{1.9}$$

If no limitation in the amount of energy released in any single collision is considered, LET is called unrestricted LET and it is indicated with L_∞.

The higher is the LET, the higher will be the biological effectiveness. In fact, high LET radiations produce more microscopic damages and then more clustered lesions with respect to low LET particles. The distinction between low and high LET, for many cellular systems, is represented by the value of 20 keV/μm.

In table 1.2, a list of LET values for ions from hydrogen to oxygen (in the energy range corresponding to 200 MeV protons) is given.

From the table, it must be highlighted that carbon ions have a LET higher than 20 keV/μm in the last part of their travel (40 mm from the stopping point) while at the beginning, in the so called "entrance channel", their LET is smaller than 15 keV/μm. This means that in the region at the end of the path, in correspondence to the Bragg peak and to the tumor, the DNA damage is high and difficult to be repaired. Instead, the damage is reduced at the path beginning where healthy tissues are present.

Moreover, for ions heavier than carbon, the range of elevated LET starts too

early and extends to the normal tissues located before the tumor. It can be seen, therefore, that carbon ions can be considered the optimal choice for the therapy of deep-seated tumors as the increased biological effectiveness, owing to the variation of the LET along the track, could be restricted mainly to the target volume [39].

Relative biological effectiveness and oxygen enhancement ratio

The information contained in the linear energy transfer, however, is not sufficient alone, because it is also necessary to take into account the DNA repair capacity of the cells after irradiation. A new quantity has to be introduced: the Relative Biological Effectiveness (RBE), defined as the ratio of the sparsely ionizing radiation (mostly ^{60}Co rays) dose and the dose of particle radiation producing the same biological effect (isoeffect) [24]:

$$RBE_{iso} = \frac{D_{X-rays}}{D_{particle}} \qquad (1.10)$$

RBE depends, in a complex way, from several variables: absorbed dose, particle energy and atomic number, cell type and survival level...
Its definition, as said before, is based on the biological response for sparsely ionizing radiation, such as X-rays. This biological response is quantitatively described by S, the cell survival, a non-linear function of the absorbed dose D. For doses up to few Gy, S can be parametrized using a linear-quadratic (LQ) model [40]:

$$S(D) = S_0 e^{-(\alpha D + \beta D^2)} \qquad (1.11)$$

α and β are parameters, experimentally determined, characterizing the radiation response.
In particular, the ratio α/β introduces the "shoulder" behavior in the survival curve, a plot of survival cells in a semi-logarithmic scale, which is shown in figure 1.8. Moreover, this ratio is a measure of the cellular repair capacity.
 From the figure, it can be noticed that for increasing LET (curves 2, 3 and 4), the survival curves, represented in logarithmic scale, become linear as a function of the dose; hence the term β can be considered as negligible. For lower LET values (curve 1) instead, the coefficient β turns out to be not unessential since the survival curves are no more linear with respect to the dose.
Moreover, the figure shows that, for carbons, a particular level of survival is reached with a lower deposited dose with respect to photons. This demonstrates the different level of damage produced by sparsely and densely ionizing radiation.
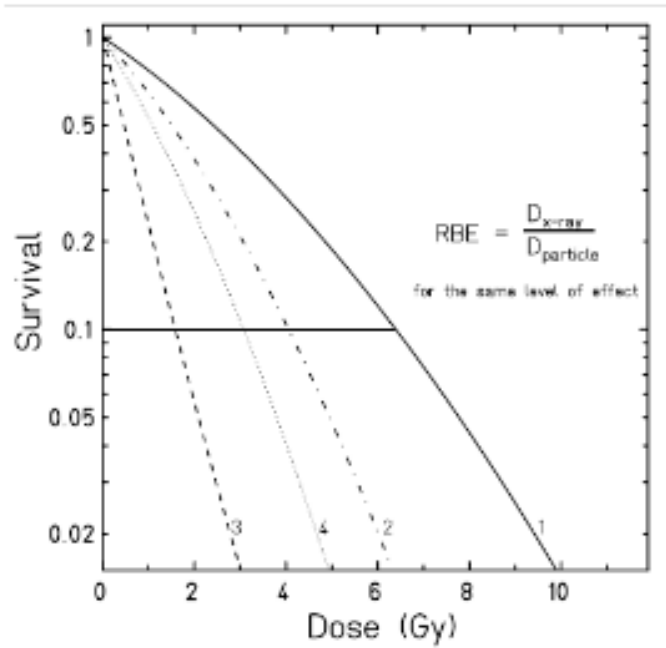
Figure 1.8: Survival curves (in logarithmic scale) for CHO-K1 cells irradiated with X-rays (1) and carbon ions of different energies: (2) 266.4 MeV/n LET = 13.7 keV/μm, (3) 11.0 MeV/n LET = 153.0 keV/μm, (4) 2.4 MeV/n LET = 482.7 μm [24].

Figure 1.8 also shows that, for different carbon ion energies, different dose-effect curves are obtained. This can be explained as follows: for high ion energies, corresponding to high ion velocities, the LET is low ($L = (\frac{dE}{dx}) \propto \frac{1}{v^2}$) hence a specific quantity of energy is lost in a longer part of the track with respect to what happens at the end of the path, when the energies and velocities are small and LET is high. At low LET, therefore, the ionization events occur far enough to make repair possible, yielding shouldered curves similar to sparsely ionizing radiation. When energy decreases, instead, the LET increases. This leads to a higher ionization density that means that the ionization events occur closely, diminishing the influence of repair and yielding a significantly increased RBE. At very high LET values, finally, at the end of the particle range (for carbon ions this is above 200 keV/μm) the local dose density becomes higher than necessary for a lethal damage and RBE decreases again [24]. In this last case there is an over production of local damages: it is the so called over-kill effect.

It is necessary to point out that the impact of RBE on tumor killing is

higher when the RBE maximum overlaps sufficiently with the Bragg maximum, thus getting together both effects of dose and high RBE but, at the same time, minimizing the biological effects before the peak. In fact, the compromise between sterilization of the tumor and damage to the surrounding healthy tissues is a crucial point in hadrontherapy.

For carbon, the high RBE region (with values ranging from 2 to 5) is limited to the end of the particle range; in the entrance channel, instead, the RBE is lower (about 1) and the produced damages are easily repaired. For ions heavier than carbon (Ne, Si, Ar) the RBE is high in the entrance channel (see figure 1.9). For this reason carbon ions have been chosen from the beginning of 1990's as optimal for treating deep-seated tumors, being considered as the most suitable for hadrontherapy also from the biological point of view.
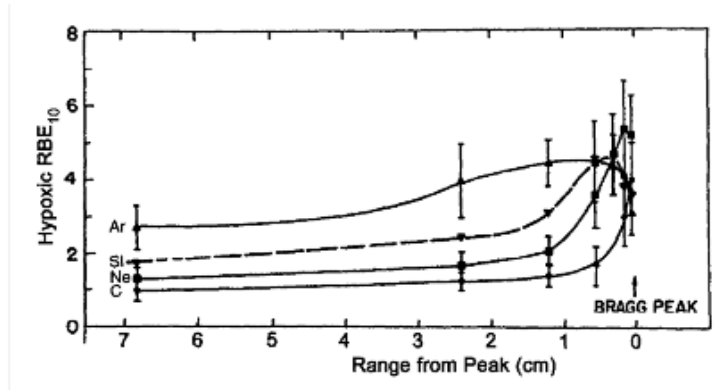
Figure 1.9: RBE for C, Ne, Si and Ar ions as function of the penetration depth inside a hypoxic tissue. For carbon ions RBE is relatively low at the entrance and becomes higher close to the peak [37].

An important challenge in hadrontherapy is the cure of hypoxic tumors i.e. tumor cells deprived of oxygen. As a tumor grows, it rapidly outgrows its blood supply, leaving portions of the tumor with regions where the oxygen concentration is significantly lower than in healthy tissues. Especially in the center of large tumors, hypoxic regions occur frequently. Even if a widely accepted mechanistic explanation for this effect is still missing, it is known that hypoxic conditions lead to a larger radioresistance. The effect that takes into account the level of oxygen in the tumor cells in the so called oxygen effect, quantified by the Oxygen Enhancement Ratio (OER):

$$OER = \frac{D_{hypoxic}}{D_{aerobic}} \tag{1.12}$$

where $D_{hypoxic}$ and $D_{aerobic}$ are the doses in reduced and normal oxygen conditions, respectively, producing the same biological effect [23]. The lower is the OER value, the higher is the effect of irradiation on hypoxic cells. OER is dose independent even though is a dose-modifying factor. Its value is typically 3 for conventional radiation while, for ion beams, is significantly reduced. For high-LET particles, it is close to 1, a value that means that the effect on normal and hypoxic cells is the same.

It has been found that the minimum OER is lower for heavier ions such as carbon or neon than for light ions (e.g. helium). Therefore, heavy particles such as carbon ions offer enormous potential for curing tumors with hypoxic regions.

1.1.3 Advantages and drawbacks in the use of heavy ions in radiation therapy

Highlights of carbon ion therapy advantages

As pointed out in the previous section, heavy ions and in particular the carbon ones present several advantages for radiotherapy due to their physical and biological properties. These advantages can be summarized as follows:

1. carbons deposit their maximum energy density at the end of their range, in the Bragg peak, where they can produce severe damage to the ill cells while sparing both the transversely adjacent and deeper located healthy tissues;

2. carbon beams have a favorable depth profile of the RBE. This is the most significant advantage with respect to protons; at high energies, in the entrance channel mostly repairable damages are produced, corresponding to low RBE values, while in the last 2-3 cm of the range, the RBE significantly increases to values between 2 and 5, depending on the type of tumor;

3. carbon ion beams are easily realized as narrow, focused, pencil-like beams. In this way the tumor can be accurately irradiated with optimal precision. In addition, carbon ions penetrate the patient with minor lateral scattering and longitudinal straggling; lateral and longitudinal scattering, in fact, is about 3 times smaller than for protons.

Drawbacks: the nuclear fragmentation

Nuclear beam fragmentation is the main disadvantage for the use of carbon ions in radiotherapy. This phenomenon is caused by the interactions with

the elements placed along the beam line as well as inside the tissue itself. While the first effect can be reduced through an appropriate beam delivery system, the second is an intrinsic contribution and therefore not eliminable. However, it is important to know in details the effects on the delivered dose. The most frequent nuclear reactions occurring in the energy range of hundreds MeV/n are the peripheral collisions, in which one or several nucleons can be lost by the beam particles. The process, illustrated in figure 1.10, can be described by the abrasion-ablation model [42]. Nucleons in the overlap-
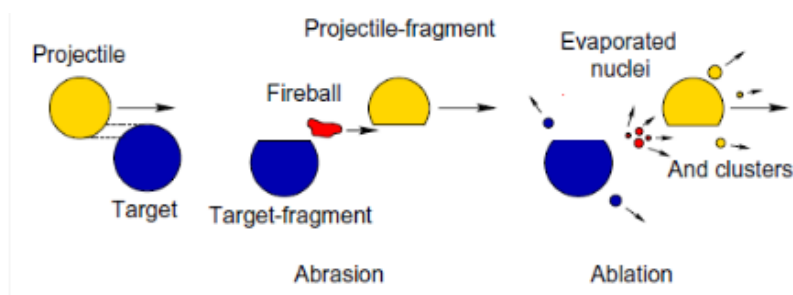
Figure 1.10: A simplified model of the nuclear fragmentation due to peripheral collisions of projectile and target nucleus [42].

ping zone, between the interacting projectile and target nuclei, are abraded, forming the hot reaction zone (fireball). The outer nucleons (spectators) are only slightly affected by the collision. In a second step (ablation), the remaining projectile and target fragments, as well as the fireball, de-excite by evaporating nucleons and light clusters. Projectile fragments are emitted mainly in the forward direction, due to the high projectile speed. Projectile-like fragments, traveling in the same direction and with almost the same velocity of the beam, contribute to the dose delivery until they stop or experience other nuclear interactions. Target-like fragments, instead are emitted isotropically and with smaller velocities.

The nuclear fragmentation results in a reduction of the primary beam flux and in a build-up of low-Z fragments. These fragments have a longer penetration depth if compared to primary ions, since the range (for particles at the same speed) scales with A/Z^2. For this reason the fragments are responsible for the undesired dose behind the Bragg peak: the tail.
Figure 1.11(a), illustrates the normalized depth-dose distributions, in case of SOBP, (Spread Out Bragg Peak, for the definition see section 1.1.2) for proton, carbon and neon ion beams having the same range. Tails are clearly visible for ions. Moreover, the tail height depends on the ion mass. From the figure, it can be seen that the increasing dose after the peak is approximately 15% of dose in the SOBP for ions like carbon and oxygen, while it can reach
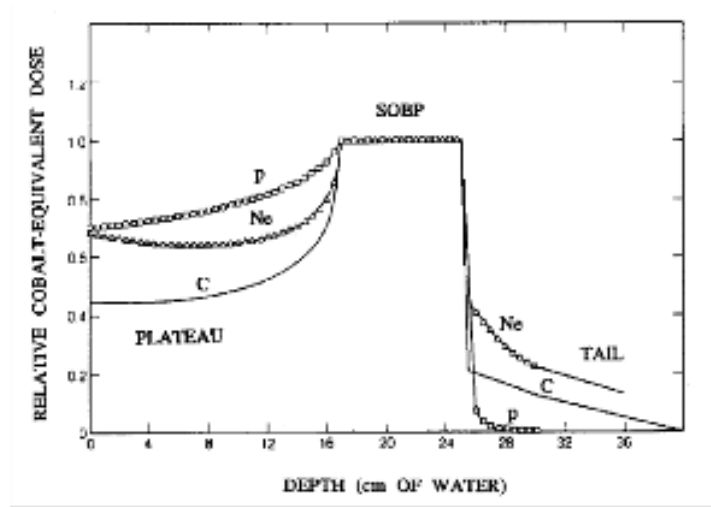
(a)
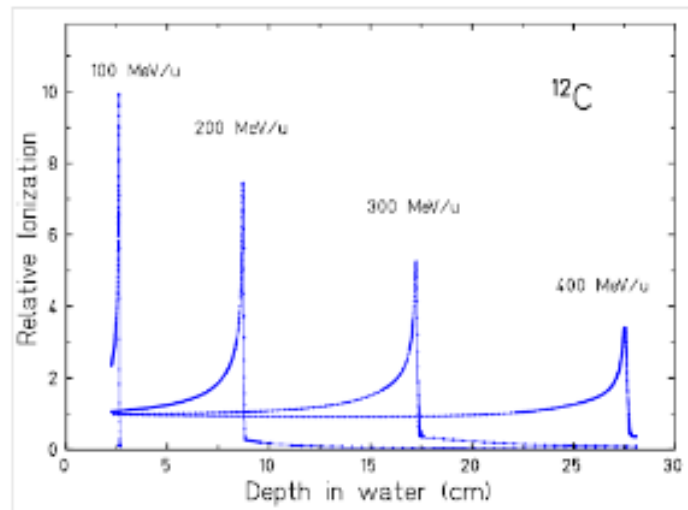
(b)

Figure 1.11: (a) Comparison of spread out Bragg peak (SOBP) for proton, carbon and neon beams with the same range in water. Tails due to fragmentation are evident for ion beams and more dramatic for neon ion beams [21]. (b) Measured Bragg curves of ^{12}C ions stopping in water [48].

30% in case of neon ions. This is one of the reasons why it is not justified to use ions heavier than oxygen for a really conformal therapy.

It is really important to take into account, in treatment planning, the effects of fragmentation also because of the different biological effects characterizing the secondary particles produced, which give rise to a mixed radiation field. Calculations of the fragment contribution in term of doses and ionization density, together with the carbon ion fragmentation study, represent one of the key-points in hadrontherapy.

Figure 1.11(b) shows the impact of nuclear fragmentation on carbon ion depth-dose profiles. The peak-to-entrance dose ratio becomes smaller with the increasing of the penetration depth, due to the exponential reduction of the primary ion flux. Particle fluence (i.e. the flux integral over time), in fact, decreases with the penetration distance according to the law [43]:

$$\phi(x) = \phi(0)e^{-\mu x} \qquad (1.13)$$

where $\phi(0)$ is the entrance fluence and μ is the linear attenuation coefficient, proportional to the total microscopic reaction cross-section σ for the ion-tissue interaction.
In figure 1.11(b), the build-up of lower-Z fragments is clearly visible in the dose tail behind the Bragg peak at larger depths.

To know the composition of the fragment field is necessary for dose optimization in heavy ion therapy, to take correctly into account the global biological effect in the tissue, due to secondary as well as primary particles. Moreover, both nuclear fragmentation cross sections and algorithms that deal with the transport of charged particle in matter, are essential for accurate treatment planning, mainly because, nowadays, about 50% only of the heavy ions addressed to the patient reach the tumor (if deep-seated) [44]. However, the transport models used in the deterministic codes (like TRiP [45, 46], developed at GSI or HIBRAC [47]) for treatment plans, have a predictive capability that, in case of mixed radiation fields and complex geometries, does not seem adequate for all practical purposes.
Reliable tools to overcome this lacks are the Monte Carlo transport codes like FLUKA [49] or GEANT4 [50, 51]. Nevertheless, recent studies [52–54], which compared the nuclear reaction models implemented in FLUKA and GEANT4 Monte Carlo codes with experimental data, pointed out only a modest agreement between them.
To improve the performances of the simulation codes, it is necessary to determine the MC parameters with fits to the experimental data. At present, however, the worldwide available data set is very limited. In particular experimental data concerning the composition of the fragments, i.e. the double differential cross sections in energy and angle, for carbon ions in the energy

range 60-400 MeV/n, are missing. Among the negative results of this situation due to the large uncertainties in the light fragment angular distributions, differences up to an order of magnitude in the various code predictions are present. Similar problems are found in codes used for space radiation transport in shielding materials [55].

In this context, the present work aims to fill the gap of information about the fragment build-up and their angular and energy distributions by presenting the preliminary results of a carbon fragmentation experiment in the energy range of interest for treatment planning (400 MeV/n).

1.1.4 The INFN Treatment Planning System (TPS) project

The INFN (Istituto Nazionale di Fisica Nucleare) Treatment Planning System project consists in a set of experiments, whose aim is to collect data in order to allow, for each hadrontherapy treatment, the proper conversion from the ion beam features (energy, position and intensity) to the specific dose required from the medical prescriptions. In order to fully exploit the potentialities of ion treatments, the information deriving from the experimental data will be used to arrange for an algorithm able to make up all the key parameters (physical as well as biological) necessary to optimize the dose distribution.

Each radiation therapy treatment planning is based mainly on two steps:

1. to define the target volume. The task of the treatment planner is to determine the appropriate particle positions, energies and fluences (i.e. the integral of flux over time, as mentioned in the previous section) in order to achieve the prescribed dose in a given target volume. A 3D model of the treatment geometry is constructed using the modern imaging techniques. This model is needed to find the most suitable beam entrance regions, with the requirement that the passage through structures under risk (organs, healthy tissue) should be avoided. For protons and heavier ions, generally, only few entrance regions are necessary thanks to their superior depth-dose characteristics.

2. To include the RBE evaluation for each irradiation point, iteratively. The biological effectiveness of primary ions as a function of depth in the irradiated tissues has to be evaluated carefully by taking also into account the effects due to all the secondary fragments produced in nuclear reactions within the irradiated volume. To evaluate the relative

biological effectiveness of a beam, in particular in the case of ions, is a hard task due to its several dependencies and to the complex radiation field generated.

The TReatment Planning for Particles (TRiP), developed at GSI [56,57], is a treatment planning system, whose aim is to find the best superposition of a large number of pencil beams (each one with its energy, particle number and position) in order to obtain the prescribed dose. This procedure is called inverse planning. The TRiP code includes a physical model that describes the nuclear fragmentation and the depth-dose profiles of ^{12}C ion pencil beams. Moreover, it also contains the Local Effect Model (LEM), able to calculate the biologically effective dose, the RBE and the cell survival (together with other biological endpoints, i.e. observed or measured outcomes in a clinical trial that indicate the effect of the treatment being tested) for any dose level and radiation field composition (provided the photon sensitivity for the tissue under consideration is known).

Starting from successful experiences of collaboration between INFN and radiotherapists and oncologists (CATANA [58] or CNAO [59]), at present, many INFN research groups with knowledge in different fields (from nuclear physics to Monte Carlo simulations passing through radiobiology and hardware/software development for dose monitoring purposes), are cooperating to develop an improved Treatment Planning System for ion therapy (with a special attention to carbon ions) with active scanning [60].

The active scanning method uses two magnets to move the beam in the two orthogonal directions. The tumor is virtually divided in slices in the longitudinal direction and each slice is thought as composed of small volumes of the same thickness, called voxels. Each slice is irradiated fixing the beam energy and irradiating each voxel changing the currents of the scanning magnets. Furthermore, for each voxel in a slice, it can be taken into account the dose given during the irradiation of the previous slices. Therefore with active scanning the irradiated target is shaped very closely to the tumor target, both in the transverse and in the longitudinal planes.

The drawback of such beam delivery system is a greater difficulty in operation due to the management of the scanning magnets and of the beam position and also an increased sensitivity of the system to current changes. Problems occur, particularly, in the cases in which tumor moves because of breathing and heart beating. For this reason, several studies are in progress worldwide, in order to develop methods that allow to use the active scanning with moving tumors.

To use this technique, an optimization procedure is needed to determine the optimal beam spot energies, positions and fluences starting from the pre-

scribed dose distribution. The goal is to have a TPS able to compute the dose delivered to the patient with the highest probability of eradicating all the tumor cells (sparing the healthy tissues) and, simultaneously, able to evaluate the treatment plan with a high level of interactivity and in real time.

The development of the optimization algorithm, described by an appropriate objective function, has to face two main aspects: the first is to improve the knowledge on the biological effects of radiation by effectively including the various physical and biological factors into the algorithm; the second is to evaluate and minimize the objective function, within the hardware constraints (computation time, memory management) by developing suitable mathematical methods.

The INFN TPS project has been proposed to give significant improvements with respect to the state of the art treatments, by finding solutions to several open issues; for example:

- the improvement of physical models for fragmentation, especially trying to cover the lack of experimental data for carbon ion fragmentation between 20 e 400 MeV/n;

- the development of Monte Carlo simulations to verify the implemented TPS;

- the improvement of on-line monitoring techniques for the dose delivery;

- the factorization of the RBE computation from the cell type;

- the factorization of the dependence of the TPS on the accelerator and beam control system.

This PhD thesis is based on the work performed on an experimental set-up at GSI: FIRST (Fragmentation of Ions Relevant for Space and Therapy), whose aim is to investigate the fragmentation cross sections at relativistic energies, to improve, among other aspects, the nuclear physics models within the Monte Carlo codes included in the TPS project.

1.2   Space Radiation protection

One of the most serious challenge in space explorations is the health protection from the risks due to space radiation. Since the radiation in space and on Earth are substantially different, a high uncertainty is present on the estimated radiation health risk (including cancer and non-cancer effects); this

makes protection extremely difficult. Moreover, the very high energy (E) and charge (Z) of Cosmic Rays (CR) and the severe constraints on the spaceflight mass make the shielding in space very hard. In addition, although Monte Carlo transport codes can, at present, describe quite well the CR-matter interaction, more accurate evaluations of doubly-differential cross sections in angle and energy are needed to improve the simulations [61].

1.2.1 Space radiation risks and effects

Space is a dangerous environment for humans and enabling life in space requires to deal with several health risks [62], summarized by NASA in the NASA bioastronautics roadmap [63] and updated in the Human Research Roadmap [64]. These risks are rated from 1 to 3, in order of danger. The first type corresponds to risk of serious health effects; in this case, if a mitigation can not be carried out, the spatial mission can not take place. The second one means serious health risk worsened by the fact that the medical countermeasures are not yet validated in space. Finally, third risk category corresponds to small risks due to suspected health consequences; this kind of risks has a limited impact on the mission design.
The health hazard can be summarized in three main categories [65]:

1. physiological problems caused by microgravity (risk 3),

2. psychological and medical problems due to isolation (risk 3),

3. acute and/or late hazard caused by radiation exposure (risk 1).

The last category is for sure the most risky. The complex nature of the space radiation can lead to both acute (i.e., short-term risk of radiation sickness) and late (e.g., cancer) effects. Acute radiation syndrome is associated to the intense Solar Particle Events (SPE) exposure and, at the same time, to the absence of adequate shielding for the crews. Late radiation morbidity, including cancer and other diseases of old age, instead, is associated to the chronic exposure to Galactic Cosmic Radiation (GCR). The space radiation is different both qualitatively and quantitatively from the Earth's radiation natural background: in deep-space High charge (Z) and Energy particles (HZE) provide the main contribution to the equivalent dose while γ rays and low-energy α particles are major contributors on Earth. For this reason the estimated uncertainty in radiation risk is very high, especially for carcinogenesis, Central Nervous System (CNS) damage, and late cardiovascular damage. Estimates of this uncertainties on space radiation cancer mortality hazard range from 400% to 1500% [66]. This uncertainty is certainly too high

([67, 68]) even if many ground-based experimental programs are currently ongoing to reduce it. In addition, countermeasures are not easily available. In fact, over the three main ways to reduce the radiation exposure, i.e. increasing the distance from the radiation source, reducing the exposure time, and shielding, only the third is feasible. In space, the first way is not an option since cosmic radiation is isotropic. Time of space explorations will be increased, rather than decreased in the future; therefore also the second way is not possible. Shielding remains the only solution available, which can contribute significantly to risk reduction, although it cannot be a full solution for the GCR problem [69]. In fact, very heavy shielding are not practical on spaceships. Other strategies to reduce radiation damage are available: administration of drugs or dietary supplements to reduce the radiation effects and crew selection based on genetic screening. However, due to the high uncertainty on risk estimates and to the lack of effective countermeasures, cosmic radiation remains one of the main health concerns for space exploration.

In particular, the poor knowledge of CR biological effects is one of the main sources of uncertainty. The principal gaps in knowledge can be summarized as follows [61]:

- relative biological effectiveness factors of energetic heavy ions for late effects, both cancer and non-cancer types;

- shape of the dose-response curve at low doses for charged particles;

- dose and dose-rate reduction effectiveness factors;

- errors in human data including statistical, dosimetry and transfer among populations in application to space radiation risks;

- interaction of radiation damage with other space environment stressors (particularly microgravity).

It is sure, however, that the main biological effects of radiation exposure are negative and dangerous: carcinogenesis, degenerative tissue effects, acute and hereditary effects. Among them, cancer is the dominant risk. Hereditary effects, instead, are assumed to be a factor of 10 or more lower than somatic effects in radiation protection, although there is missing evidence for heavy ions in this field. Acute effects are expected only for very intense SPE, hitting an unprotected crew.
At present, large ground-base radiobiology research experimental programs

are ongoing in different countries (USA at the NASA Space Radiation Laboratory in the Brookhaven National Laboratory, NY, Europe at GSI in Darmstadt, Germany and Japan at HIMAC in Chiba), to reduce the uncertainty on biological effects, especially of heavy ions [70–72].

Another important concern for the safety in spaceflight is due to the effects of CR on microelectronics. The charge generated by the ionization of energetic particles in spacecraft electronics can upset microcircuit functions. The damages produced if the charge yield is sufficiently high, can be of two types: destructive or non-destructive. The destructive effects can not be repaired. They are mainly single-event induced, i.e. single-event gate rupture, single-event burnout, single-event dielectric rupture ... The second ones, also called soft errors or SEU (Single Event Upset), are the most common. They consist in a change of state (bit flip) that affects bipolar and metal-oxide-semiconductor elements. Luckily, this kind of errors can be easily corrected by rewriting the affected element, but they can still represent a threat to spacecraft electronics [61].

Before electronic components can be sent into space, they have to be qualified on Earth. These tests are usually done using γ rays (for total dose effects) or low-energy beams of accelerator facilities (for SEU). Two parameters are used to test the vulnerability of a device to SEU: a threshold LET (minimum LET required to produce SEU) and the saturated cross section (maximum upset rate for the device, when no increase is observed by further increasing the LET). But, as for the biological effect, LET alone may not be the only parameter characterizing the effect. Below the LET threshold, nuclear reactions can still produce SEU, and high-energy ions are more effective than low-energy ions [73]. Moreover, recent studies ([74, 75]) using particles at energies around 1 GeV/n, pointed out that, in the range between LET threshold and saturation, cross sections are higher for low energy ions compared to relativistic high energy and charge particles at the same LET.

Tests done using high-energy accelerators are considered the best ones; in this case the particles can cross the whole device, allowing the device test at different tilt angles [76].

1.2.2 Radiation measurements in spaceflight

The detectors for the monitoring of radiation environment on spacecrafts (in particular the ISS, International Space Station) are divided in two categories: the first concerns the "operational radiation monitoring devices". These are area monitors and personal dosimeters like the ThermoLuminescence Dosimeters, TLD. They are used to measure organ or tissue doses to

be used for normalizing radiation transport calculations, individual dose assessment, field quantities and real-time or near real-time estimates of dose rates.

The second category, instead, includes specific detectors, selected for precise science topics and used for limited times. For example, on the ISS, these topics are the characterization of the radiation field (such as the determination of particle flux and energy spectra for each particle type, at different locations and times in the different modules and outside the space station) and the influence of shielding material composition and thickness on radiation protection [61].

1.2.3 Exposure limits and organ doses

In the last years, the estimates of cancer risk caused by radiation exposure did not change greatly: they are based on the Life Span Study (LSS) of the survivors following the atomic bombing of Hiroshima and Nagasaki. This estimates, corresponding to acute exposure, are corrected by the so called DDREF, Dose and Dose-Rate Effectiveness Factors, which consider the reduced radiation effectiveness at a low dose rate. The risk coefficient recommended by ICRP-103 [77] is 5×10^{-2} Sv^{-1} [3].

The average annual effective dose on Earth is about 3 mSv and can be reduced to less than 1 mSv when the man-made sources and the internal α-particle exposure to Radon (Rn) daughters are excluded. Moreover, the exposure to cosmic radiation on the Earth's surface is reduced to a nearly zero level because of the Earth's magnetic field and the atmospheric thickness of about 1 kg/cm^2. Instead, dose rates in space are definitively higher: the equivalent dose rate on Mars ranges between 100 and 200 mSv/yr [78], depending on the solar cycle and altitude; values around 350 mSv/yr can be reached on the Moon [79]. The astronauts, therefore, present a considerably higher radiation risk than the population on Earth, even if compared to occupationally exposed workers, whose effective dose limit recommended is 20 mSv over a period of 5 years. In table 1.3, the corresponding NASA astronaut career limits are reported and compared with those from other space agencies. As can be seen from the table, the European, Canadian and Russian space agencies do not adopt age- and gender- corrected coefficients, but apply a single career limit of 1 Sv.

These recommended effective career limits refer to effective doses, which must be estimated from personnel dosimetry combined with radiation trans-

---

[3]The sievert (Sv), is the measurement unit of the equivalent dose in the International System (IS). This quantity has the same dimension of the absorbed dose: $\frac{J}{kg}$.

Table 1.3: Age- and gender-dependent career effective dose limits (in Sv) as recommended by different space agencies [80, 81]. NASA limits are always based on 3% risk of exposure-induced death, and the values refer to a 1 yr mission.

Space agency	Gender	Age at first exposure, (yr)			
		30	35	45	55
NASA (USA)	Female	0.47	0.55	0.75	1.1
	Male	0.62	0.72	0.95	1.5
JAXA (Japan)	Female	0.6	0.8	0.9	1.1
	Male	0.6	0.9	1.0	1.2
ESA		1.0	1.0	1.0	1.0
FSA (Russia)		1.0	1.0	1.0	1.0
CSA (Canada)		1.0	1.0	1.0	1.0

port codes [77]. Only the skin dose is measured in all astronauts by TLD (ThermoLuminescence Dosimeters). The use of measurements performed on human-like phantoms can improve effective dose estimates but cannot represent the movements of individual astronauts within a complex spacecraft. Organ doses have been calculated by NASA using Computerized Anatomical Models (CAM) [82, 83]. The CAM man model represents a 50th percentile U.S. Air Force male. The computerized anatomical female model has been obtained by removing male organs and incorporating female organs and taking into account the smaller stature of the woman. An example of CAM phantom is MATROSHKA [84], on board ISS.

1.2.4 The shielding

The constraints related to spacecraft volumes and mass are the major priority to be considered when talking about shielding. Moreover, the extra fuel required to launch such shielding has to be taken into account when considering the mass dedicated to shielding itself.

An improvement in this field can derive from material selection and topology optimization. Considerations coming from atomic and nuclear physics can be used to guide the material selection together with detailed radiation transport code predictions. Engineering considerations, such as material strength, UV degradation, flammability, etc. must also be taken into account in the selection [61].

In the following, a description of the atomic and nuclear phenomena, which play a fundamental role in the choice of the shielding material, will be given. The goal of a shield is to stop the cosmic radiation inside the absorber ma-

terial. Therefore, it is mandatory to minimize the radiation path inside the absorber, the so called "range" R, that equivalently to equation 1.5, can be defined as:

$$R \equiv \int_{x_i}^{x_f} dx = \int_{E_i}^{0} \frac{dx}{dE} dE = \int_{E_i}^{0} (\frac{dE}{dx})^{-1} dE \qquad (1.14)$$

where x is the coordinate along the (straight) trajectory of the particle inside the absorber, hence x_i and x_f are the particle initial and final positions inside the absorber, corresponding to the entrance point in which the energy is E_i and the stopping point where the energy is 0, respectively.

From equation 1.14, it is possible to see that the minimization of the range corresponds to the maximization of $\frac{dE}{dx}$, the energy loss, which depends on the atomic composition and density of the material according to the Bethe-Bloch formula[4]:

$$\frac{dE}{dx} = k\frac{Z}{A} * \frac{1}{\beta^2} * f(\beta) * \rho \qquad (1.15)$$

ρ, Z and A are the density and the atomic and mass numbers of the absorber. (Equivalent numbers are used in case of poly-atomic composition of the shield). The parameter k contains only universal constants, together with the charge of the incident particle (in electron units). The function $f(\beta)$ is slightly dependent on the material and this dependence can be neglected for the purposes of this discussion.

It must be remarked that equation 1.15 provides the energy loss per unit path length of one particle. When a fluence of particles, I, passes through a thickness dx, the total amount of energy loss is given by the product $I * \frac{dE}{dx}$. Therefore the quantity $\frac{dE}{dx}$ can be considered as the energy loss per unit of fluence and of length.

Thus the choice of the best material for a shield results from the maximization of the ratio $\frac{Z}{A}$ and the density ρ. Nevertheless the interaction of the radiation with the matter includes also a number of nuclear reactions. Considering a fluence I of particles, passing trough an infinitesimal thickness dx of absorber, the number of reactions dI produced in the passage is given by:

$$dI = \sigma * I * dx * \frac{N_{Av}}{A} * \rho \qquad (1.16)$$

where σ is the total cross section of the interaction particle-nucleus of the absorber and N_{Av} is the Avogadro's number. It is possible to write, with a good approximation: $\sigma = \sigma_N * A^{2/3}$, in which σ_N is the total cross section

---

[4]A more detailed description of the Bethe-Bloch formula, which describes the energy loss of a heavy charged particle inside matter, is given in section 1.1.2 and in appendix 2.

particle-nucleon, independent on the material.

The number of reactions per unit of fluence and of path length is given by:

$$\frac{dI}{dx} * \frac{1}{I} = \sigma_N * A^{2/3} * \frac{N_{Av}}{A} * \rho = \sigma_N * N_{Av} * \rho * A^{-1/3} \qquad (1.17)$$

The total cross section includes the following nuclear reactions: elastic and inelastic scattering, pion production, absorption and fragmentation. All these reactions, of course, subtract the incident particle from the primary fluence and this seems to contribute to the shielding. Unfortunately, other particles appear in the final state: the same particle with different energy after the scattering, produced pions, decay products after the absorption and fragments. They can have high energy and produce a secondary fluence inside the absorber. Therefore their number should be minimized. Minimization of both range and secondary fluence requires to maximize the ratio r of the energy loss per unit of fluence and of length to the reaction number per unit of fluence and of length:

$$r = \frac{dE}{dx} * (\frac{dI}{dx} * \frac{1}{I})^{-1} = \frac{k}{\sigma_N * N_{Av}} * \frac{1}{\beta^2} * f(\beta) * \frac{Z}{A^{2/3}} \qquad (1.18)$$

The ratio r is an indication of the role played by both Z and A in the optimization of the shielding materials. Noteworthy it is independent on the absorber density, since this term is present in both the phenomena, energy loss and reactions, hence disappears.

Thus equation 1.18 can be used as a first guide to the shielding selection. Of course, the final choice must take into account also other parameters: the relative importance of primary and secondary fluence in damaging both human tissues and devices, the relative weight of the reaction cross sections, the weight, availability and costs of the materials etc...

1.2.5 Space radiation transport codes and Monte Carlo track simulations

In this field, Boltzmann type transport equations are used for the description of the passage of high energy particles through matter. These equations treat the atomic and nuclear interactions, which modify the particle energy and type in the collision.

NASA developed a Boltzmann equation based code: HZETRN [85] to describe the transport of High charge (Z) and Energy particles (HZE). The code includes the Quantum Fragmentation Multiple-Scattering model (QMS-FRG) [86], whose predictions on cross sections agree with spaceflight measurements of organ equivalent dose within ±20% [87, 88]. This code that

uses broad energy beam boundary conditions, together with the GREEN-TRN code, which uses narrow energy beam or monoenergetic boundary conditions [85], calculate the average flux of each particle at different depths in shielding. These codes have been well validated by space and accelerator measurements. Recently, code extensions have added methods for bidirectional neutron transport and pion transport [89, 90].

Moreover, in HZETRN code, complex spacecraft geometries can be handled using ray tracing techniques to represent thousands of spacecraft parts even if only in a bidirectional transport.

As an alternative, recently, Monte Carlo codes such as GEANT4, FLUKA or PHITS [91] have been used for space applications, to develop the trajectories of charged particles and the energy deposition in materials. The Monte Carlo codes, furthermore, are able, in principle, to produce very detailed detector designs and more complicated geometries can be considered in this approach compared to the HZETRN code because the angular scattering of particles is also taken into account. However, until now, only simplified geometries have been implemented into MC codes to represent the complex spacecraft geometries and the MC potentialities have not been fully exploited.

For what concerns the track simulation codes, they need, for transport simulation and tracking, the total, total elastic, total inelastic, ionization, and excitation cross sections. Examples of ion track codes are RITRACK or the GSI developed code TRAX. The first one generates radiation tracks up to very high energies (> 10 GeV/n) and includes relativistic corrections to ionization and excitation cross sections, including bremsstrahlung contributions [92, 93]. The second one [94] uses the empirical cross-section formulas developed by Rudd [95] and modified for the use at high ion energies (including empirical corrections in accordance with energy loss tables). Thanks to these corrections, the microscopic calculations of TRAX can be expanded to predict macroscopic quantities. The Bragg peak position for heavy ions, for example, can be determined and reproduced with an accuracy better than 0.7 mm; furthermore, the dose values estimated are in good agreement with macroscopic calculations.

However, many of the codes developed for this purpose, are limited to energies below 10 MeV/n. Moreover, few data at high energies are available to validate the accuracy of the effective charge assumptions used by the models at higher energies [95].

For these reasons, experiments aiming to provide measurements of the still missing cross sections are really helpful.

1.2.6   Transport code validation

The evaluation of uncertainty in transport codes, which are able to evaluate radiation exposure of sensitive tissues behind shielding on spacecrafts, can be obtained through three approaches:

1. comparison of ground-based measurements carried out with several defined beams on thin or thick targets of different materials;

2. comparison of transport codes to spaceflight measurements;

3. inter-comparison of radiation transport codes, using matched environments and configurations.

An example of good agreement among transport code predictions and experimental measurements is given by the GERMCODE. It is a Monte Carlo code developed to describe the NASA Space Radiation Laboratory (NSRL) beam line for radiobiology applications [96]. In particular the NSRL carried out extensive measurements of the Bragg ionization curve originating from several HZE nuclei on polyethylene or aluminum shielding. GERMCODE is a GCR (Galactic Cosmic Rays) event-based risk model that exploits the QMS-FRG (Quantum Multiple Scattering FRaGmentation) model of the nuclear interaction database and the atomic energy loss subroutines from HZETRN. A comparison between the GERMCODE and the NSRL measurements (for ^{28}Si, ^{37}Cl, ^{48}Ti and ^{56}Fe) is given in figure 1.12. A good agreement between the measurements and the model is appreciable at all the depths, including the region beyond the Bragg peak, in which only the secondary radiation contributes.

Furthermore, many inter-comparisons between the HZETRN and Monte Carlo codes like FLUKA have been performed, for specific configurations, which shield from GCR [55] and SPEs [97]. The results of the comparisons show a reasonable agreement among the transport codes in the cases taken in exam.

However, even if some encouraging results are available for what concerns the agreement between data and models and also among the different transport code results, many problems are still existing. In fact, there are some cases in which different codes give very contrasting predictions: differences can be greater than an order of magnitude, especially for the production of light ions. This is due to the lack of measurements, which can provide information about the physical quantities (like cross-sections) needed to perform a reliable transport simulation.
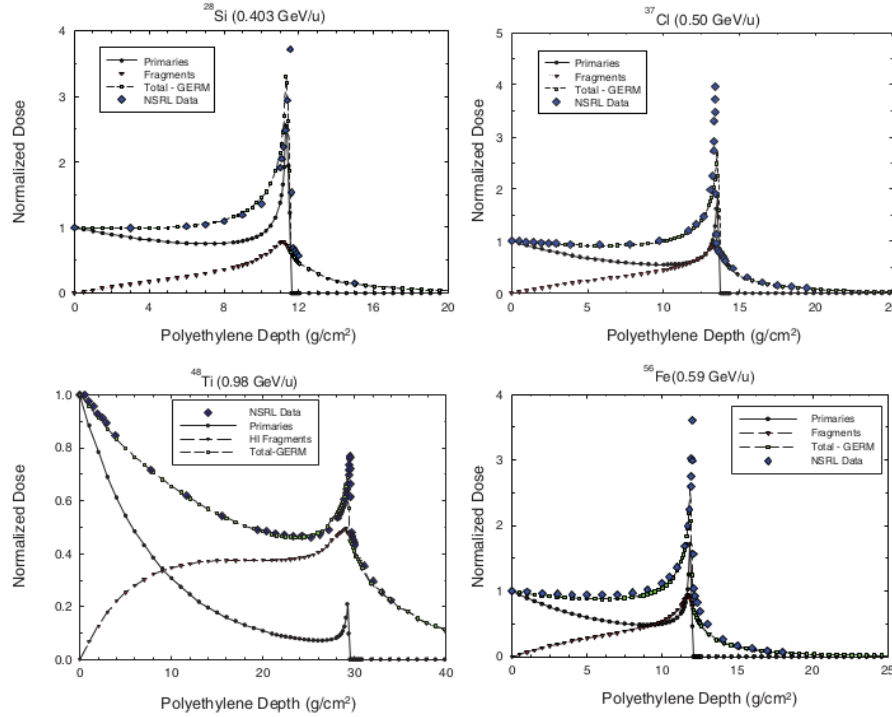
Figure 1.12: Comparisons of the GERMCODE with QMSFRG cross sections to NSRL measurements for the depth dose in polyethylene for nearly monoenergetic ^{56}Fe (0.59 GeV/n), ^{48}Ti (0.98 GeV/n), ^{37}Cl (0.5 GeV/n) and ^{28}Si (0.403 GeV/n) nuclei [96].

To summarize:
the existing radiation transport codes are in agreement within 20% with measurements of organ doses; however, such an agreement is not enough neither for medical treatment purposes (in which an accuracy $< 3\%$ is required [98]) nor for radiation protection in space. Therefore, a further increase of experimental data-sets is necessary to improve the transport codes.
Future work has the aim to enhance the knowledge of interaction cross sections and their usage in space radiation transport codes. Many cross-section data sets have been determined; however, there are still significant gaps in double-differential cross sections for light particle production, cross sections for new materials of interest and knowledge of exclusive cross sections that is needed to support stochastic based risk models that supplant the current deterministic dose based quantities.

Chapter 2

The FIRST experiment

The experiment FIRST (Fragmentation of Ions Relevant for Space and Therapy) is inserted in the context of the particle therapy and space radiation protection applications.

For this purpose the experiment is designed to measure the double differential cross sections (DDCS) of nuclear fragmentation processes in the energy range between 100 and 1000 MeV/n.

In particular, the Treatment Planning System (TPS, see section 1.1.4) application of the measurements drives the constraints on the precision to reach: a 3% of maximum uncertainty in each bin of the energy and angle (20 x 20) phase space is required [99].

FIRST was designed and realized by an international collaboration from France, Spain, Italy and Germany. The data taking was carried out on summer 2011 at the Heavy Ion Synchrotron SIS of GSI (Helmholtz Center for Heavy Ion Research) in Darmstadt and was focused on the measurement of fragmentation deriving from a ^{12}C beam at 400 MeV/n colliding on carbon and gold targets.

2.1   The experimental setup

The FIRST experimental setup consists of several sub-detectors divided into two different regions [99]: the Interaction Region (IR), whose detectors have been built specifically for this experiment and the Large Detector Region consisting in already existing devices. The two regions are separated by a magnet working as a spectrometer. In table 2.1 the list of detectors with their features is given.

Table 2.1: FIRST detector overview

Name	Type	Function	Angular coverage (deg)	Trigger capability
Interaction Region				
Start Counter	Scintillator	Start of Time of Flight		Yes
Beam Monitor	Multi-wire drift chamber	Control of beam direction and impact point on target		No
Vertex Detector	Si pixel detector	Fragment emission angle from target	$\lesssim 40$	No
KENTROS	Scintillator	Time of Flight and Energy loss for large angle emitted fragments	$\approx 5-90$	Yes
Large Detector Region				
ToF-Wall	Scintillator	Stop of Time of Flight and Energy loss for small angle fragments	$\lesssim 5$	Yes
Veto Counter	Scintillator	Trigger veto, Time of Flight and Energy loss	$\lesssim 1$	Yes

The dimensions of the detectors are significantly different in the two regions: the impinging beam and created fragments are detected in the IR within some centimeters from the target; after the magnet, in the Large Detector Region, the fragments are detected using devices with typical dimensions of meters. The IR is in air: this choice strongly helps the design and the construction of the detectors in this region while increasing the out of target interaction probability only by about 5 % [99]. A schematic view of the FIRST setup is given in figure 2.1. Following the beam path, it is possible to see:

- the Start Counter (SC), which provides the start to all time measurements,

- the Beam Monitor (BM), a drift chamber that gives the beam trajectory and the impact point onto the target,
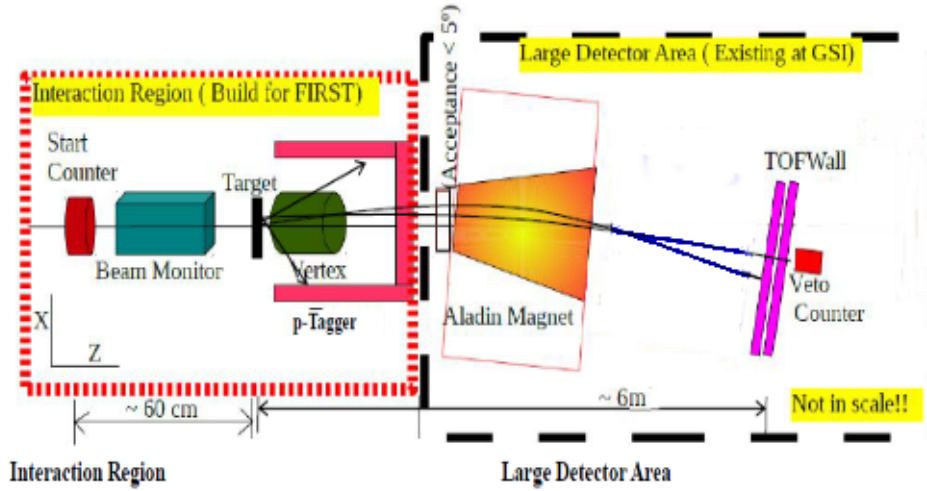
Figure 2.1: Schematic view of the FIRST setup.

- a robotized target system, which allows to insert and extract the target from the beam line,

- the Vertex Detector (VTX), a pixel silicon device that tracks the charged fragments emerging from the thin target and

- the Proton Tagger (KENTROS), a thick scintillator, which detects the light fragments at large angles.

The heavy fragments (Z>2) are expected to be produced mostly in the forward direction (see figure 2.2) with β close to the beam velocity and then are within the magnetic acceptance of the ALADiN dipole magnet [100]. The figure 2.2 shows the angular distribution predicted by FLUKA Monte Carlo ([49], [101]) for the fragments produced by a 400 MeV/n carbon beam on carbon: the number of all the particles produced in the target for a given run in a certain energy bin, N_{prod}, divided by the number of ions, N_{primC}, in the primary ^{12}C beam, is shown as a function of the fragment angle. As it can be seen, the heavy fragments are forward peaked.

After magnetic bending, fragments enter in the Large Detector Region where, after a flight of about 6 meters, are detected by the Time of Flight Wall (ToF-Wall). This is a large area system of scintillators that provides the measurement of the impinging point, the arrival time and the energy release of the particles. Finally, the Veto Counter, a scintillator sandwich positioned after the ToF-Wall on the trajectory of the ^{12}C beam fraction, which does
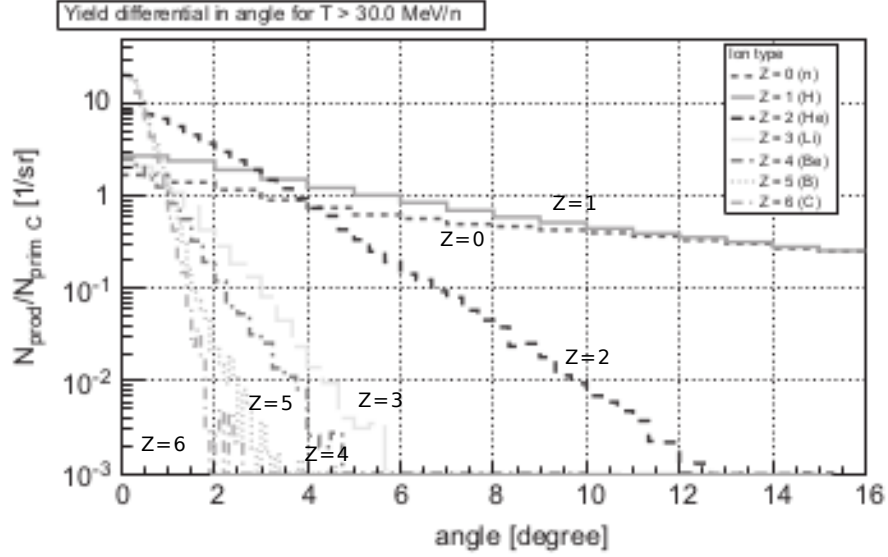
Figure 2.2: Angular distribution of the fragments produced by a 400 MeV/n carbon beam on 8 mm carbon target. N_{prod}/N_{primC} is the yield of fragments per primary carbon ion and steradian with a kinetic energy larger than 30 MeV/n (FLUKA Monte Carlo) [99].

not interact with the target, is used to analyze the survived beam.

The magnet ALADiN deviates the ion trajectories according to their impulse to charge (in electron units), p/Z, ratio. The curvature radius, deriving from the Lorenz force, is in fact:

$$R = \frac{Z}{p} * eB \tag{2.1}$$

where e is the electron charge and B is the modulus of the magnetic field. The knowledge of the fragment path, from the target to the ToF-Wall, through the magnetic field, allows to evaluate the curvature radius and therefore the p/Z ratio of the fragments. Therefore, high care must be taken to match the information of the Interaction Region with that collected in the Large Detector Region.

The main features of the ^{12}C beam provided by the SIS (Heavy Ion Synchrotron) accelerator are:

- a rate of incoming particles in the range of the kHz and

- a Gaussian shape of the beam spot in the transverse plane of $\sigma \simeq 2.1$ mm.

The time structure of the spills has a flat shape of $\simeq 10$ s out of 20 s duration in total.

The whole FIRST experimental setup is able to fulfill several requirements:

- suitable particle identification capability providing a $\Delta M/M \leq 10\%$ (M is the fragment mass),

- tracking capability to measure angles (the angular resolution on tracks is $\leq$0.2 degrees) and kinetic energies per nucleon (the resolution on the kinetic energy per nucleon varies from 30 to 100 MeV/n, depending on the energy interval and on the ion) of the produced charged fragments, at the exit of the target,

- large angular acceptance of the IR detectors for the detection of low energy proton and helium ions: the calorimeter KENTROS allows the detections of light fragments in the angular range 5–90 degrees.

In the following sections a detailed description of all the FIRST detectors will be provided.

2.1.1 The Interaction Region

The detectors belonging to IR were tested at LNS (Laboratori Nazionali del Sud) of the INFN (Istituto Nazionale di Fisica Nucleare) under the 80 MeV/n ^{12}C beam of the Superconducting Cyclotron and also at INFN LNF (Laboratori Nazionali di Frascati) under the electron beam at 510 MeV of the Beam Test Facility.

In figure 2.3 the technical drawing of the IR is reported.

The Start Counter (SC)

The Start Counter is a thin scintillator designed for triggering and timing purposes. It is located on the beam path, 20 cm before the target. It is designed in order to have a pre-target particle interaction probability of less than 1% with respect to the on-target one, reducing to a negligible amount the Start Counter contribution to the systematic error on the cross section measurements [102]. A time resolution better than 250 ps (σ) is necessary to reach the precision on fragment time of flight measurement required by FIRST ($\sim$100 ps) and hence achieve a good capability in the separation among the masses of the different isotopes (A=1,2,...,12). Such a resolution is also sufficient to allow the measurement of the time of flight of the fragments
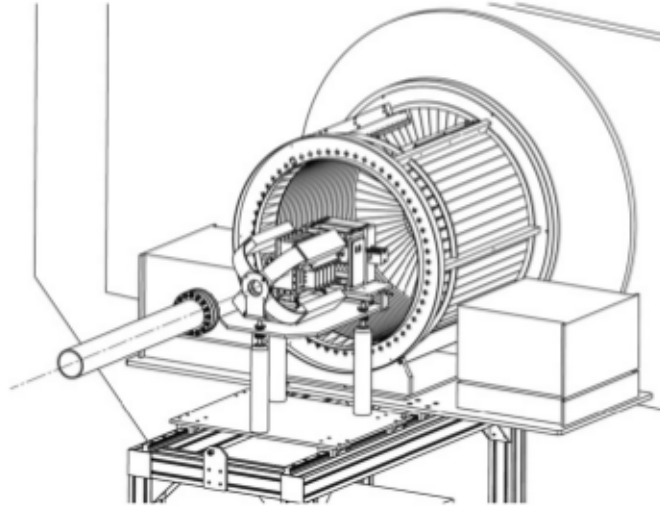
Figure 2.3: Technical drawing of the Interaction Region, embedding the Start Counter, the Beam Monitor, the Vertex Detector and the Proton Tagger [99].

in KENTROS, where the track lengths are in the range 20–80 cm. The SC is made of a circular thin foil of plastic scintillator (EJ-228) with a diameter of 52 mm and 150 μm of thickness (see figure 2.4). Light is collected by means of 160 step-index plastic optical fibers (IEC 60793-2-40) each of 1 mm in diameter; they are radially glued and grouped in four bundles and finally connected to four fast Hamamatsu UBA H10721-201 photomultipliers (PMTs). The performances of these PMTs are 40% of quantum efficiency and 250 $ps/\sqrt{N_{ph.el}}$ in time resolution. The signals coming from the four photomultipliers are amplified by a factor 20 by means of custom electronics boards embedded in the detector. The fiber layout has been chosen in order to maximize the light collection from the scintillator.

During the tests performed at LNS under ^{12}C and proton beams of energy 80 MeV/n, an efficiency of (99.7 ± 0.15)% has been obtained for the SC. During these tests a majority of 3 PMT signals out of 4 was required. A time resolution of 130 ± 1 (stat) ps was obtained under the ^{12}C beam; using the proton beam, instead, a 310 ± 1 (stat) ps time resolution was obtained.

The Beam Monitor (BM)

The Beam Monitor is a drift chamber designed for the reconstruction of charged particle trajectories. This detector gives the impact point of the beam on the target. Moreover, this detector can provide important information on possible pre-target fragmentation of the projectile [102]. In fact, if a
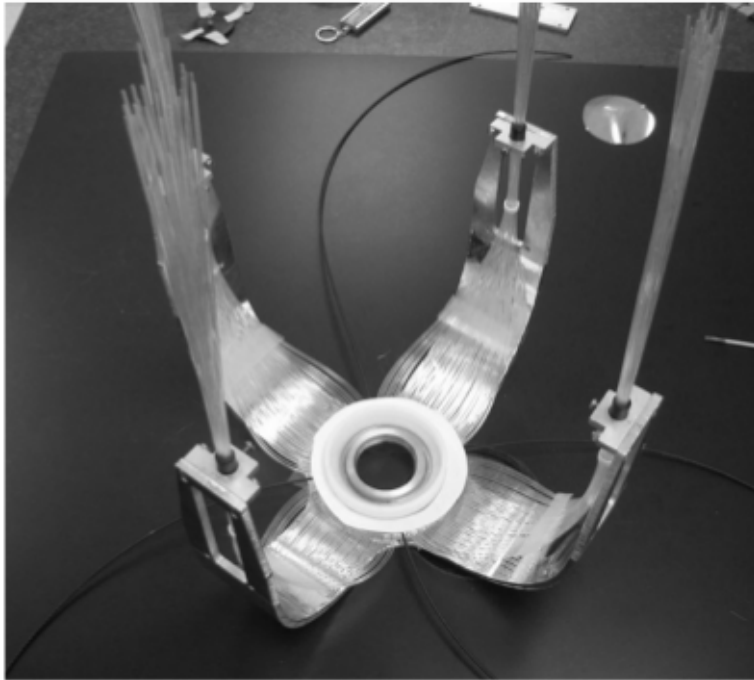
Figure 2.4: The thin SC scintillator foil readout by scintillating fibers [102].

fragmentation event occurs before the target, the BM detects more than one track.

The BM provides two orthogonal profiles of the beam by mean of six planes of three cells (see figure 2.5), for a total of 36 sense wires horizontally and vertically alternated for each view. In order to resolve the left/right ambiguity, the consecutive layers of each beam view are staggered by half a cell. Each cell has a rectangular shape with dimensions of 10 x 16 mm^2 with the long side orthogonal to the beam, in order to minimize the possibility of beam-wire interaction (see figure 2.6). The chamber has an active volume of 2.4 x 2.4 x 2.4 cm^3. Under the ^{12}C beam, it is operated with a Argon/CO$_2$, 80/20 gas mixture at a working point of 1.8 kV, which turned out to be the best working conditions after the tests performed at LNS with ^{12}C and proton beams and at LNF using an electron beam. During these tests an efficiency of 99% and a spatial resolution of 80 μm were measured.

Custom front-end electronic boards are connected to the detector and provide wire signal amplification by a factor 10.

The BM main task is to track the arriving carbon beam with a precision of about 100 μm on the impact point on the target. This is required because the VTX detector (see next subsection), due to its high readout time, can
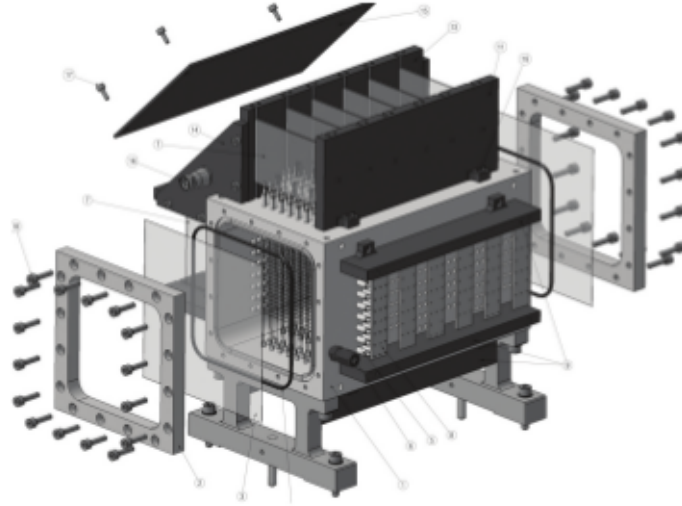
Figure 2.5: BM drift chamber technical drawing [102].
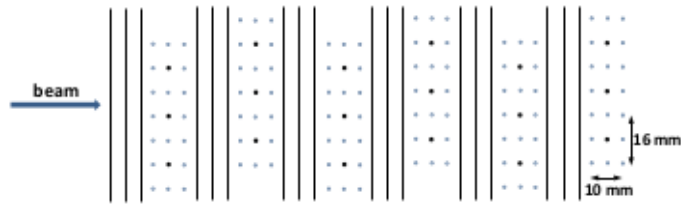
Figure 2.6: BM cell layout [102]. See text for more details.

register, in a single event, two (or more) carbon tracks: the phenomenon is called pile-up[1] and has a 10% probability at 1 kHz interaction rate. Therefore, the BM precision is necessary to discriminate between the two tracks in VTX. In fact, the beam track detected by the BM in these events must point to the correct carbon track in Vertex.

Moreover, a high space resolution, when a single hit is present, is needed, in the chamber, to provide a good angular resolution on the scattering angle between the carbon projectile and the fragments produced.

---

[1]The pile-up events happen when VTX, after a first event, does produce a signal for the successive event and the signals are such that the detector readout is unable to discriminate and separate them and therefore clusters due to the two events result as fired.

The Vertex Detector (VTX)

The Vertex detector has to fulfill several requirements [103]. At first a wide angular acceptance (considering also the non-negligible beam spot transverse size of $\simeq 5$ mm) is required to track also large angle projectiles (outside the ALADiN acceptance window); an angular resolution on tracks of about 0.3 degrees is then needed due to TPS (see section 1.1.4) requirements. Moreover, a purity at the percent level in the separation between two tracks is necessary to minimize systematic errors. In addition, a whole sensor thickness of few percent of the target thickness (0.8 cm) is needed to reduce the nuclear interactions of carbon ions inside the sensors. Finally, a wide dynamic range is preferable in order to be able to detect signals from about two MIPs (Minimum Ionizing Particle) by fast protons up to the two or three order of magnitude larger signal from slow carbon ions.

In order to satisfy all the requirements, a new pixel sensor has been developed by the Strasbourg group of the FIRST experiment [104] to equip Vertex: Mimosa26 (Minimum Ionizing Metal Oxide Semiconductor Active pixel sensor, M26). This sensor has a sensitive area of 10.6 x 21.2 mm^2 covered by 576 rows and 1152 columns of pixels with 18.4 μm pitch. In rolling shutter mode, its readout time is 115.2 μs per frame. The sensor, providing only digital information on the fired pixel, is equipped with zero suppression logic to reduce the DAQ bandwidth. Moreover, in order to properly associate the different tracks and clusters to their vertex also in pile-up events, information from BM will be associated to the one of Vertex to identify the on-target interaction (and then the fragmentation vertex).

VTX is made of four stations. On each of them, two M26 sensors are glued on the two sides of a 1 mm thick PCB (Printed Circuit Board) in correspondence to a square hole with sensing area of 2 x 2 cm^2 (see figure 2.7). Using four 1 mm thick PCBs, the distance between two consecutive stations is 2 mm and the total longitudinal VTX dimension is 12 mm with an angular coverage of ± 20 degrees. Moreover the use of a 50 μm thinned sensor (overall sensor thickness of 200 μm) allows to reduce the secondary fragmentation in the vertex detector to a tolerable level.

The pixel cluster size in the M26 sensors has been tested at LNS using carbon beams of different energies; it was found that it is possible to achieve a double track separation of 99% for the expected fragments. This conclusion has been drawn also from the simulation results, which show that clusters from a track pair will be closer than 100 μm (maximum cluster diameter corresponding to 6-7 pixels) only in 0.3% of cases.
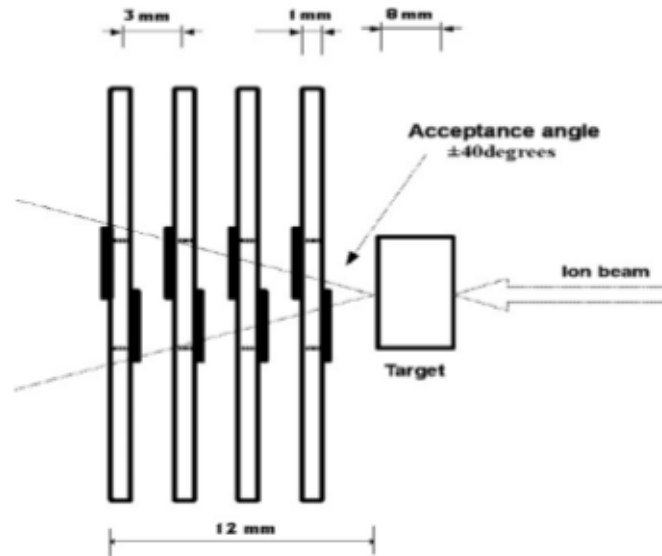
Figure 2.7: Relative positions and dimensions of beam, target and four VTX sensor housing boards (stations) [99].

The Proton Tagger (KENTROS)

KENTROS (Kinetic ENergy and Time Resolution Optimized in Scintillator) is placed between VTX and ALADiN. It has the aim to measure kinetic energy and time of flight of particles emitted with polar angles higher than 5 degrees. In particular, its response is optimized for detecting low energy protons. In fact, protons with kinetic energy up to 100 MeV are the most interesting from the TPS point of view (they release their whole energy inside the patient body). For this reason, it is necessary to achieve a relative error on the kinetic energy of such a kind of protons less than 15%. Therefore, the detector has been designed in order to provide a time resolution of 250 ps. This small time resolution influences the kinetic energy error because the kinetic energy itself can be estimated by measuring the energy deposition in the detector and the ToF.

The detector has an active part made of organic scintillator modules and scintillating fibers [105]. The modules are built using EJ-200 fast scintillators with decay time of 2.1 ns, 10^4 photons/MeV light yield, 425 nm wavelength of maximum emission, 1.58 refractive index and 4 meter attenuation length. The scintillating fibers are 1 mm diameter BCF-10 fibers with decay time of 2.7 ns, $8*10^3$ photons/MeV light yield, 432 nm wavelength of maximum emission, 1.6 core refractive index and 2.2 meter attenuation length.

The signal is read using Silicon PhotoMultipliers (SiPM) with active area

of 4x4 mm^2, which have excellent timing resolution (about 100 ps). The scintillation light is driven from the modules to the SiPM through plexiglass light guides. The SiPM output is processed by a custom electronics whose aim is to properly send the signals to TDCs and ADCs and to provide a discriminated OR-ed pulse for triggering purpose. For this reason the electronics amplifies, reshapes, splits and discriminates the waveforms. Custom electronics have also been developed to handle the SiPM power supply and the discrimination thresholds of all the channels.

The KENTROS shape is cylindrical. Moreover, the detector is structured in three main parts depending on the angular coverage (see figure 2.8): a Small Endcap, covering angles between 5 and 15 degrees, a Big Endcap, for particles with polar angles between 15 and 36 degrees and a Barrel, that covers angles between 36 and 90 degrees. In details:
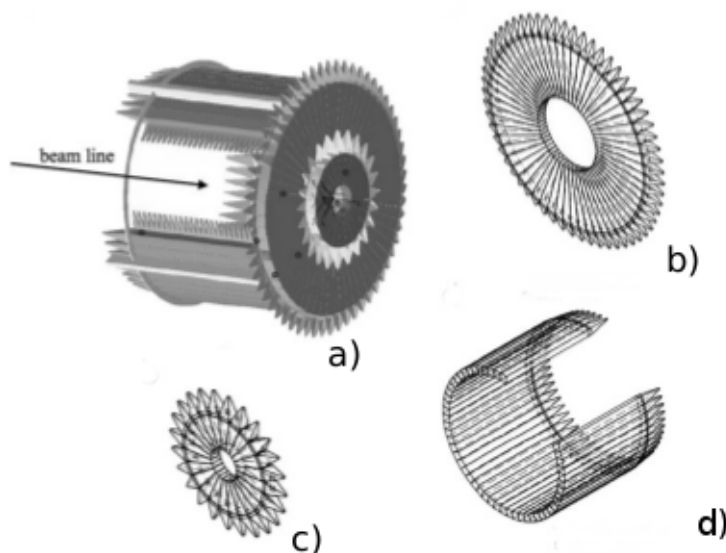
Figure 2.8: Technical drawings of KENTROS: a) general assembly, b) big endcap, c) small endcap and d) barrel [99].

a) the small endcap (figure 2.8c) has the shape of a disk with a hole with 10 and 30 cm of internal and external diameters, respectively. It is composed by 24 trapezoidal scintillator modules having a 3.87 cm greater base, a 1.28 cm lesser base, a 10 cm height and thickness of 3.5 cm, along the beam direction;

b) the big endcap (figure 2.8b) has the same shape of the small endcap with different dimensions: the internal and external diameters are 28

and 74 cm, respectively. It is composed by 60 trapezoidal scintillator modules whose dimensions are 3.8 cm for the greater base, 1.39 cm for the lesser base and 23 cm for the height. The thickness is equal to the one of the small endcap;

c) the barrel (figure 2.8d) has an active part composed by two layers. The external one has an external diameter of 74 cm. It is made of 50 scintillator modules oriented in the beam direction. Each module has a trapezoidal section of thickness 3.8 cm, lesser base 3.4 cm, greater base 3.8 cm. The scintillator length is 50 cm. The azimuthal angle covered by each module is 6 degrees.

The internal layer is made of two planes of 1 mm diameter scintillating fibers, bent to form circles. These fibers are grouped in 20 modules containing 20 x 2 fibers each. The azimuthal angle resolution is 2 degrees.

During the tests performed on the small and big endcap prototypes (at the Beam Test Facility of the Frascati National Laboratory of INFN, with 510 MeV electron beam) the measured time resolution turned out to be in agreement with the expected one for low energy protons ($\simeq$ 250 ps).

The relative resolution of the proton energy in the range of the FIRST experiment extends from a few percents for protons having 100 MeV kinetic energy to slightly more than 10% at 400 MeV.

2.1.2 The Large Detector Region

The charged particles traveling in the forward direction (i.e. with polar angle less than 5 degrees), are within the ALADiN magnet acceptance window. Therefore, they enter into the magnetic region where they are bent accordingly to their mass and momentum. After the bending they arrive in the Large Detector Region where they are detected by the ToF-Wall or the Veto Counter.

The ToF-Wall detector (TW)

The ToF-Wall is basically the spectrometer of FIRST, especially for those particles forwardly emitted, within the magnet acceptance. It measures the arrival time, energy release and impinging position of the fragments produced with polar angles smaller than ~5 degrees, allowing the reconstruction of their impulse and charge. It is placed at a distance of about 6 meters from the target, inside a chamber filled with nitrogen with an entrance window made of mylar. The TW consists of two layers, Front and Rear, made of

12 modules, each of 8 BC-408 plastic scintillator slats (110 x 2.5 x 1 cm^3), covered by aluminum foils (see figure 2.9). The 3 central slats of the Front layer have a hole of 4.8 x 5.0 cm^2 in their centers to preserve them from the plastic scintillator degradation due to the very intense transmitted beam. The upper and lower halves of these central slats are optically connected by a hollow light guide in aluminized mylar [106]. The two layers are staggered from each other of 1.25 cm (half a scintillator slat) to maximize the probability that incoming fragments hit at least one slat. Moreover, a brass foil 0.5 mm thick is inserted between the two layers in order to shield the second one from the δ electrons produced in the first plane. Each slat is connected

Figure 2.9: The ToF-Wall inside its slot.

to a photomultiplier tube (PMT) on each side. The signals from the PMTs are then split and read out by fastbus Analog to Digital Converters (ADC, model Lecroy 1885F) and Time to Digital Converters (TDC, model Lecroy 1875) for charge and time measurements, respectively. A sketch of two modules with the associated electronic chain is represented in figure 2.10.

Each fragment impinging on one scintillator slat produces 2 measurable signals on top and bottom PMTs. From the figure it can be seen that the analog signal from each PMT is split on two chains: one part is delayed and fed into the ADC, while the other is sent to a Constant Fraction Discriminator[2] (CFD) and the CFD output signal is further delayed and fed to the TDC. In this way four electronic signals (top and bottom ADCs and top and

---

[2]A Constant Fraction Discriminator (CFD) is an electronic signal processing device, designed to mimic the mathematical operation of finding a maximum of a pulse by finding
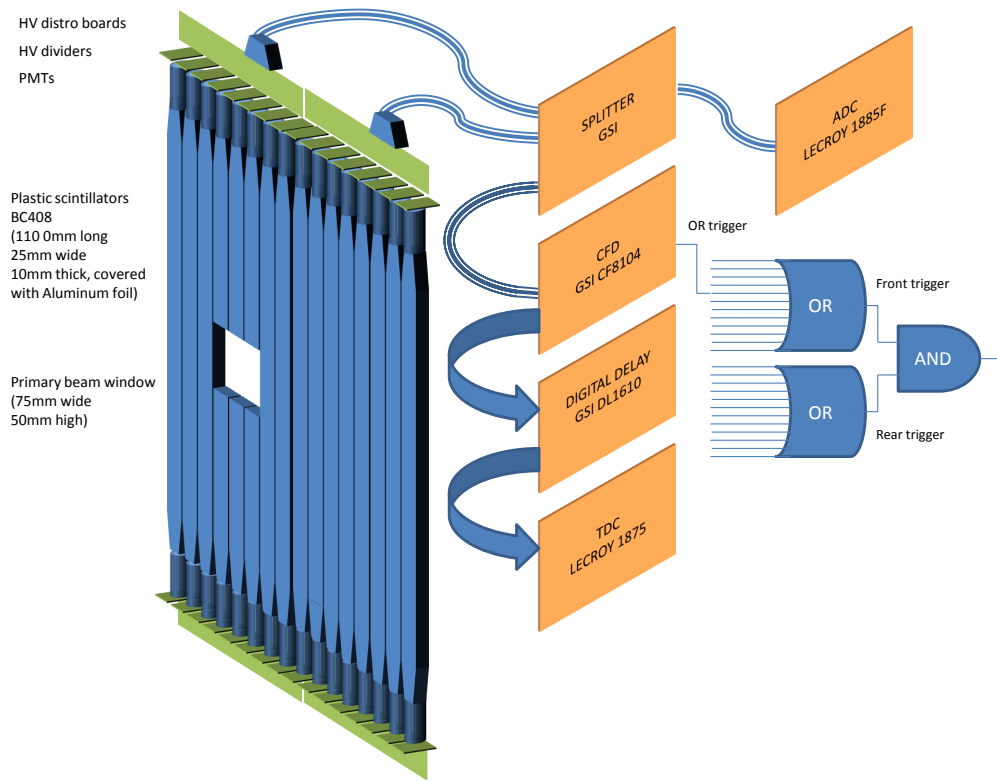
Figure 2.10: Sketch of two scintillator modules together with the associated electronic chain.

bottom TDCs) are generated per each crossed slat.

The delays inserted on the TDC and ADC signals, are needed to synchronize them with the gate and stop signals generated by the global trigger of the experiment. The signals from the CFD are also combined to provide a local trigger to the experiment.

Further details about the TW calibration will be provided in the following chapter.

---

the zero of its slope. Typical input signals for CFDs are pulses from plastic scintillation counters. The scintillator pulses have identical rise times that are much longer than the desired temporal resolution. This forbids simple threshold triggering, which causes a dependence of the trigger time on the signal's peak height, an effect called time walk. Identical rise times and peak shapes permit triggering not on a fixed threshold but on a constant fraction of the total peak height, yielding trigger times independent from peak heights.

The Veto Counter (VC)

The Veto Counter is placed beyond the TW in a position in which it intercepts the non interacting carbon beam. This because it has the aim to monitor the amount of fragments that are produced in the same angular range of the non-interacting beam. Moreover, the VC signal is also used to label non-interesting events where the carbon projectile did not interact and arrives unperturbed on this counter.
This detector is made of two scintillator slabs (BC-404) with the shape of parallelepiped with bases 6 x 6 cm^2 and 4 x 4 cm^2, respectively. They are located one beyond the other, with the bases in contact. Their thicknesses, along the beam direction, are 3 and 6 cm, respectively. The bigger slab is read by one Hamamatsu PMT on each lateral surface. The smaller one, instead, is read by one PMT on the rear surface.

2.2 Data AcQuisition system (DAQ) and triggers

The readout is handled by the Multi Branch System (MBS), a general DAQ framework developed at GSI [107]. In the MBS several intelligent bus controllers (CES RIO) perform the readout of the digitization modules of the individual crates, when triggered by the dedicated trigger modules. All the trigger modules, one in each readout crate, are connected via a trigger bus to distribute the trigger and dead-time signals and to ensure event synchronization. Data collected by single controllers are broadcast via Ethernet to an event-builder where they are merged and saved in the standard GSI format. A set of client-server applications allows to control the data acquisition, to remotely configure the detector settings and to perform on-line monitoring of the data quality.
The expected dead time, due to trigger signal formation and readout, is of the order of few ms. An efficient trigger system is then essential to select the fragmentation events and to keep the counting rate at a level where the inefficiencies due to the dead-time are minimized.
The final trigger decision requires the coincidence of the Start Counter trigger with the trigger of any of the detectors: KENTROS, ToF-Wall or the Veto Counter. In order to suppress events in which the carbon projectile does not interact with the target, coincidences between the Start Counter and the Veto Counter can be rejected.
The trigger logic is implemented in a FPGA programmable VME module (VULOM4). This module accepts individual trigger signals and implements

all the logic matrices and the downscale factors needed to control the trigger conditions, the scalers to count input and output triggers, the internal generators of regular calibration triggers and the locking mechanism to block the propagation of triggers during the dead time.

Finally, in order to avoid the need of delay lines to synchronize the KEN-TROS analog signals to the ADCs with the delayed master trigger decision, a two-level trigger system is implemented for the detectors in the interaction region. The analog signals are processed in the ADCs as soon as the local trigger from the start counter is generated; if no master trigger is received within a fixed time, a fast clear signal is provided to the electronics and the event is not recorded by the DAQ system.

Chapter 3

The ToF-Wall

A description of the ToF-Wall detector (TW) has been given in section 2.1.2. In this chapter, the procedures used to evaluate the detector efficiency, slat by slat, the calibrations performed and some preliminary results obtained after the calibrations will be presented in details.

3.1 Efficiency

A preliminary important operation that has to be performed on a detector, is to evaluate its efficiency.

In the ToF-Wall, the light, emitted when a particle hits the detector slats, reaches the PMTs but the electric signal produced can be too low, resulting under the threshold set on the corresponding Constant Fraction Discriminator (CFD). In this case the signal measurement does not take place and the impinging particle is not detected. Therefore, the efficiency is not one and must be evaluated. The inefficiencies can be due to several reasons: low ionizing particles, low PMT gain, high light attenuation and reflection losses along the scintillators.

The efficiency of the detector has been evaluated for each slat of the two planes. A conditional frequency approach has been used. For each slat, s, the response of each TDC, top and bottom, is taken into account for every particle detection.

Considering, for example, the bottom TDC: if both the TDCs reveal the signal, the case is "bottom TDC efficient", on the contrary, if the top TDC fires while the bottom TDC does not, the case is "bottom TDC inefficient". In an analogous way, when taking into account the top TDC, the case of "top TDC efficient" happens when both the TDCs react. Instead, the "top TDC inefficient" case is when the bottom TDC reveals the signal while the

top TDC does not.

The following quantities have been considered for the efficiency estimation:

- $n_{tb}(s)$ = number of events when both TDCs fired (good entries),

- $n_t(s)$ = number of events when only the top TDC fired (bad bottom entries),

- $n_b(s)$ = number of events when only the bottom TDC fired (bad top entries).

The efficiency, evaluated for the bottom TDC, called $\epsilon_b(s)$, is calculated as the number of events with both TDCs fired, $n_{tb}(s)$, divided by the sum of $n_{tb}(s)$ with the number of events with only the top TDC fired, $n_t(s)$:

$$\epsilon_b(s) = \frac{n_{tb}(s)}{n_{tb}(s) + n_t(s)} \tag{3.1}$$

Analogously, for the top TDC, the efficiency $\epsilon_t(s)$ is calculated as:

$$\epsilon_t(s) = \frac{n_{tb}(s)}{n_{tb}(s) + n_b(s)} \tag{3.2}$$

The total efficiency $\epsilon(s)$, of the whole slat s, is calculated by multiplying the two independent efficiencies:

$$\epsilon(s) = \epsilon_b(s) * \epsilon_t(s) \tag{3.3}$$

The figure 3.1 represents the total efficiency for the Front Wall (a) and for the Rear Wall (b) slats.

To calculate the efficiency, the events of the whole data set, in which the carbon beam was swept onto all the slats, without target, was used (sweep-runs). In this way the full ToF-Wall area was hit by a statistically significant amount of particles.

From the figure, it can be seen that the majority of the slats has an efficiency around 95%. This is a very good result, considering that this detector is more than 10 year old and was operated in various experiments during this period. Moreover, a number of slats has an efficiency between 70% and 95%. Only for a small fraction of slats the efficiency is close to 0. This can be due to the breakage of one or both the PMTs or to bad channel connections.

Anyway, the efficient slats are quite uniformly distributed, therefore the ToF-Wall can detect a large area with good efficiency, as requested for the differential cross section measurements.
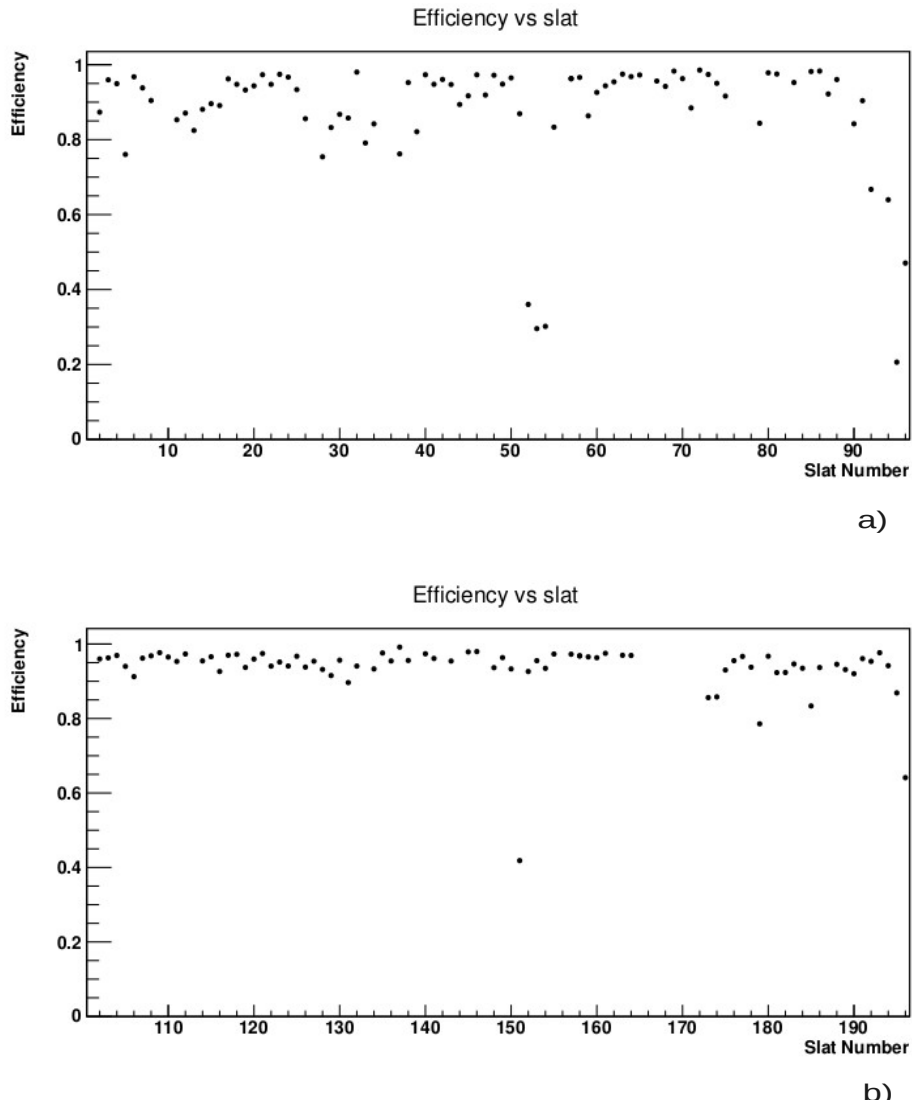
Figure 3.1: Total efficiency of the slats versus the slat number. Slats from 0 to 96 belong to the Front plane (a); slats from 100 to 196 belong to the Rear plane (b).

3.2 ToF-Wall calibration

A fundamental step to calibrate this detector is to correct for time-dependencies and channel-by-channel differences and to equalize the delays of all the components of the detector. The TW calibration has been performed using two different approaches, depending on the number of TDC and ADC measure-

ments available for each event in each slat.

If all the four TDC and ADC channels returned a measured value, the standard approach is used: the 4-channel calibration. Instead, if one channel is missing, an alternative method is employed: the 3-channel calibration.

As mentioned before, the ToF-Wall detector is fundamental for the FIRST experiment because it measures, for the impinging particles, three quantities that are fundamental for the ion recognition:

- the arrival position, providing its horizontal and vertical coordinates, (X, Z) and Y,

- the arrival time, called Time of Flight, ToF,

- the energy released in the slat, E_{lost}.

A local reference system is used, based on the TW position. It is a right-handed Cartesian reference frame, which has the z-axis along the beam direction, perpendicular to the ToF-Wall and the x- and y- axes pointing in the horizontal and vertical directions, transverse to the beam.

The coordinates in the horizontal plane are related to the slat number, which gives information on the X position of the particle, the fired wall gives the Z coordinate. The Y coordinate can be calculated in two ways: starting from the difference of the top and bottom TDC readings, or trough the ADC measurements. The first way is used for the 4-channel calibration, the second, for the 3-channel calibration. (It must be taken into account that the Y coordinate is always the same, apart different uncertainties, even if calculated in two different ways.) The sum of top and bottom TDC readings is used to derive the time of flight of the particles, defined as the time spent by a particle to travel from the target to the TW. Finally, the ADC measurements, providing information on the collected charge, allow to calculate the energy lost by the particle in the slat, E_{lost}.

Two data sets have been used for the calibrations: the "sweepruns" and the "wedgeruns".

In the sweepruns the beam (without target) has been deflected in the horizontal plane, over all the slats, by varying the magnetic field. In this way no variation of energy (except a negligible energy loss on the detector walls) occurs. Knowing the energy of the particle beam and then its velocity, it is possible to reconstruct, through geometrical calculations, the flight path. Therefore, the sweepruns are used for the calibration of the following quantities: ToF, E_{lost} and Y.

The wedgeruns, instead, have been used to correct the time walk effect, an energy dependence of the time measurement. These runs have been carried

out as the sweep ones, but with a 5 cm thick aluminum wedge set horizontally just ahead the Front Wall. The wedge is employed to produce a number of fragments with the same time of flight, independently from their energy. Figure 3.2 shows the Front Wall of the TW with the wedge set in front of it.

Figure 3.2: The TW Front Wall with the wedge ahead it.

For what concerns the ToF and the Y calibrations, two constant delays, Δ_t and Δ_b must be determined, slat by slat. In practice, to evaluate them, two equations are used, one starting from the difference of TDC readings, $TDC_t - TDC_b$, and the second from their sum, $TDC_t + TDC_b$. In this way a system with two equations and two unknowns is written and the two delay constants can be calculated.

The released energy, instead, is a non linear function of the ADC measurements, which depends on the impact point along the slat and on the particle energy. In order to determine precisely the energy, the zero signal level, so called pedestal or dark-noise level, has to be found and subtracted first. Then the overall gain is the only parameter to be determined.

For all these quantities, distributions have been considered. A Gaussian fit of the peak has been performed and the central value of the fit has been

taken as the best estimation (i.e. most probable value).

3.2.1 4-channel calibration

When all the TDC and the ADC signals are available, the following approach has been used for the calibrations.

Y coordinate calibration

The evaluation of the vertical coordinate, Y, is done using the readings of the TDCs, top and bottom.
The TDC readings are related to the particle Time of Flight (ToF), defined as the time spent by the particle to travel from the target to the TW. However, during calibrations, the sweepruns, in which the target is not present, have been exploited. Therefore the fragmentation does not take place and only the ^{12}C beam is present. For this reason, during calibrations, the time spent by the ^{12}C projectiles from the SC to the TW is considered as ToF. Moreover the TDC readings include the times spent by the scintillation pulse to reach each PMT from the impinging point, called τ_t and τ_b, the delay time to convert the scintillation light into electronic pulses and the time spent by the signal inside the electronic chain up to the TDC, Δ_b and Δ_t.
The relation is linear and given by:

$$\begin{cases} TDC_t = ToF + \tau_t + \Delta_t \\ TDC_b = ToF + \tau_b + \Delta_b \end{cases} \tag{3.4}$$

Figure 3.3 shows the description of the particle travel from SC to TW and then the light propagation inside the slat.
The values of τ_t and τ_b depend on the vertical coordinate of the impact point, Y, and on the light speed inside the slat, called v_{ligth}:

$$\begin{cases} \tau_t = \frac{\frac{L}{2} - Y}{v_{ligth}} \\ \tau_b = \frac{\frac{L}{2} + Y}{v_{ligth}} \end{cases} \tag{3.5}$$

where L is the slat length: $L = 110$ cm.
By replacing τ, given by equations in the system 3.5, in the TDC relations of system 3.4 and by subtracting the two TDC definitions one from the other, it is obtained:

$$TDC_t - TDC_b = (ToF + \Delta_t + \frac{\frac{L}{2} - Y}{v_{ligth}}) - (ToF + \Delta_b + \frac{\frac{L}{2} + Y}{v_{ligth}}) = (\Delta_t - \Delta_b) - (\frac{2Y}{v_{ligth}}) \tag{3.6}$$
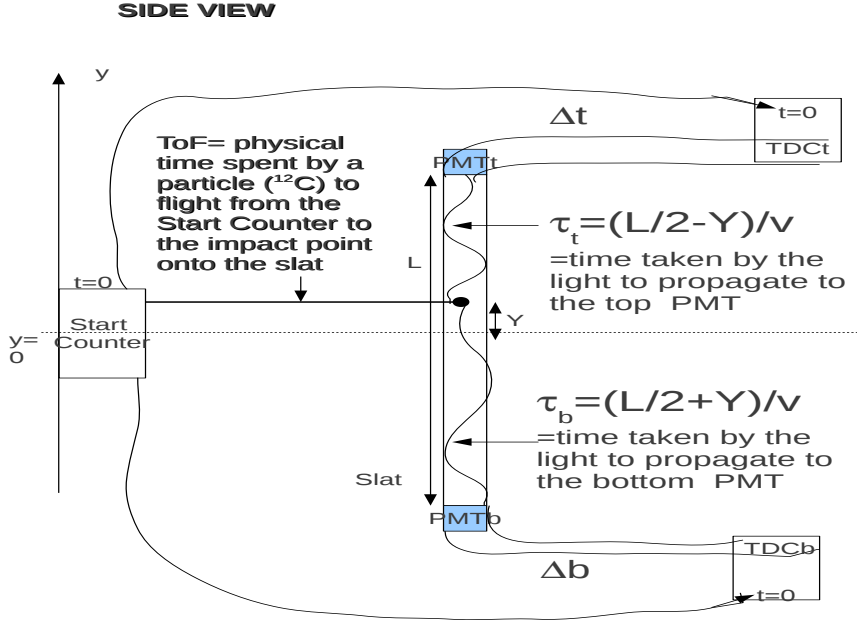
Figure 3.3: The diagram shows the particle hit position and the signal propagation sketch.

The horizontal plane on which the beam sweep onto the slat is taken as reference plane for the Y coordinate; thus Y in sweepruns is assumed as 0. Therefore equation 3.6 becomes:

$$TDC_t - TDC_b = (\Delta_t - \Delta_b) \tag{3.7}$$

The constant offset $(\Delta_t - \Delta_b)$ can be determined, on the basis of TDC reading difference.

For each slat, the TDC difference distribution is plotted. A Gaussian fit has been performed to the distribution: the mean value from the fit gives the $(TDC_t - TDC_b)$ expected value; the σ represents the measurement error. An example of the TDC difference distribution, for the slat 47, is shown in figure 3.4.

Once the TDC difference and then the difference in delay constants are determined, they can be inserted in the Y coordinate definition:

$$Y = \frac{1}{2} v_{light} [(\Delta_t - \Delta_b) - (TDC_t - TDC_b)] \tag{3.8}$$
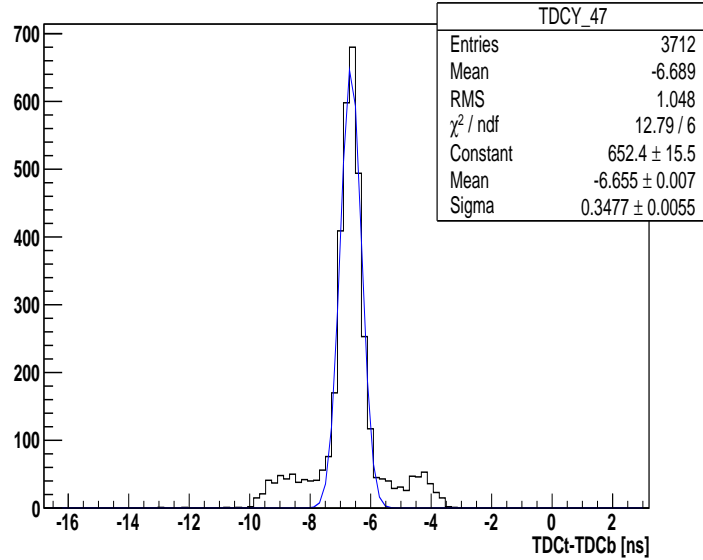
Figure 3.4: Distribution of uncalibrated $TDC_t - TDC_b$ measurements on slat 47 produced during sweepruns.

Since the two terms $(\Delta_t - \Delta_b)$ and $(TDC_t - TDC_b)$ are equal, the Y coordinate is set to 0, as expected during sweepruns.

In figure 3.5 the Y coordinate distribution, after the calibration, is shown for slat 47.

Again, a Gaussian fit is performed on the distribution. As can be seen from the fit parameters (readable in the top-right rectangle in figure 3.5), the mean value, deriving from the fit is about 0 ($\bar{Y}$=-0.3375 cm) while the σ is about 3 cm. Therefore, for slat 47, the calibration error, given by the σ of the fit, is ± 2.91 cm.

In both the figures, 3.4 and 3.5, a Gaussian fit has been performed on the central part of the distributions (TDC difference – figure 3.4 and Y coordinate – figure 3.5). As a matter of fact the beam distribution, on each slat, looks like a narrow peak surrounded by a lower, almost flat plateau. This plateau is due to the scattering of ^{12}C projectiles on the materials upstream the target (kapton membrane at the beam pipe end, SC and BM chamber), which broad the beam spot radius up to $\sim$25 cm on the TW. Hence the corresponding statistics can be discarded from the calibrations.

On the other hand, in presence of the target, the effects of this broadening are corrected by the reconstruction (not applied in the sweepruns) of the interaction vertex inside the target, which is assumed as the starting point of the fragment tracks.
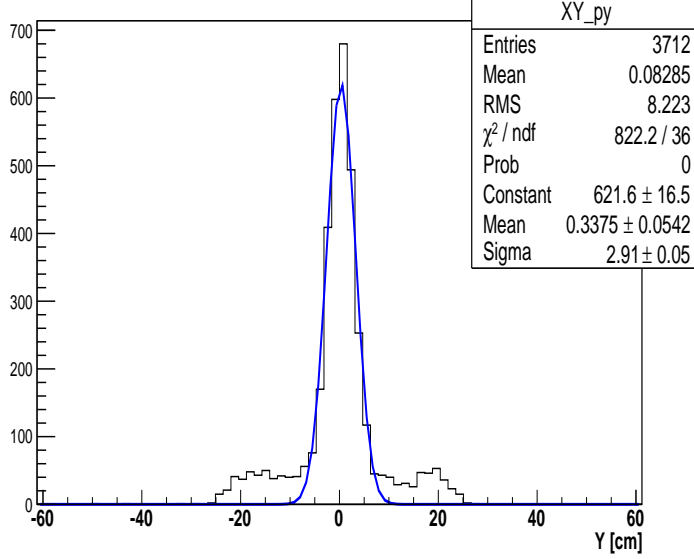
Figure 3.5: Distribution of the Y coordinate, for slat 47, after calibration.

As can be seen by equations 3.5 and 3.8, the light speed inside the slat is necessary for calibration purposes. The value of this quantity is, in principle, different for each slat. However, at first, the determination of v_{light} has been carried out, in practice, only for some slats, in the Front Wall.

A source of ^{90}Sr was used for this purpose. This source was placed in two points on the slat under measurement, in two different stages. In the first, the point was close to the bottom PMT and in the second it was close to the top one, at a relative distance of 99 cm.

During stage I, the source is put at a distance d from the bottom PMT; instead, in stage II, the source is put at the same distance d from the top PMT. d is equal to 5.5 cm.

In stage I, the vertical coordinate is $Y = -\frac{L}{2} + d$, assuming the origin in the middle of the slat, while for stage II, it is $Y = \frac{L}{2} - d$. Recalling equation 3.6 and substituting the Y values, it is obtained:

$$
\begin{cases}
\Delta TDC^{(I)} = TDC_t^{(I)} - TDC_b^{(I)} = (\Delta_t - \Delta_b) - \left(\frac{2(-\frac{L}{2}+d)}{v_{ligth}}\right) \\
\Delta TDC^{(II)} = TDC_t^{(II)} - TDC_b^{(II)} = (\Delta_t - \Delta_b) - \left(\frac{2(\frac{L}{2}-d)}{v_{ligth}}\right)
\end{cases}
\tag{3.9}
$$

By subtracting the first equation from the second one, the following relation is found:

$$
\Delta TDC^{(II)} - \Delta TDC^{(I)} = \frac{2L - 4d}{v_{ligth}}
\tag{3.10}
$$

from which the value for the light speed is calculated:

$$v_{ligth} = \frac{2L - 4d}{\Delta TDC^{(II)} - \Delta TDC^{(I)}} \qquad (3.11)$$

All the parameters on the right side of equation 3.11 are known and the light speed can be evaluated.
Figure 3.6 shows this quantity for the 14 slats in the Front Wall used in the measurement.
The average speed found, as can be seen in figure 3.6, was (15.61±0.81) cm.
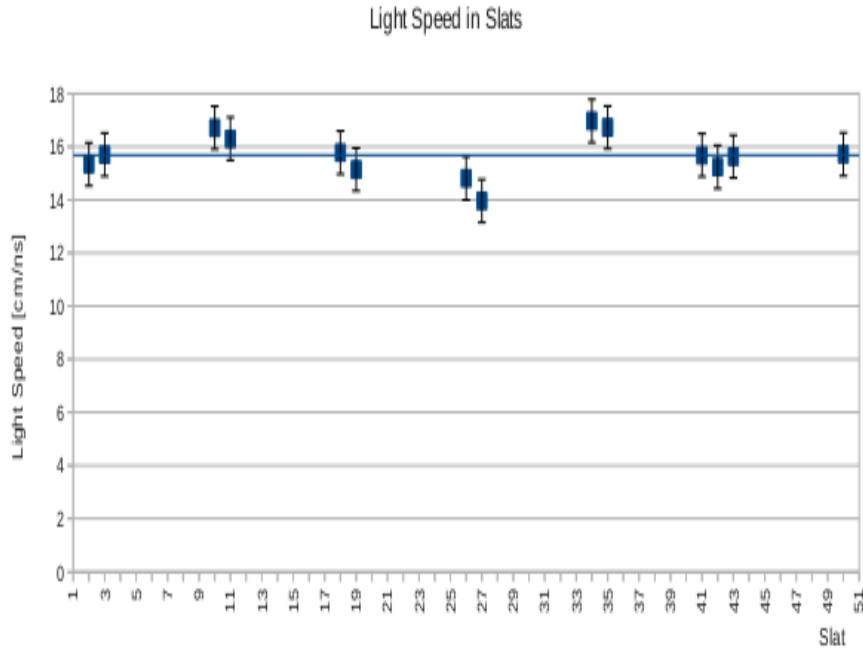
Figure 3.6: Speed of light values inside the 14 slats considered in the measurement vs the slat number.

The Y coordinate evaluation obtained using the TDCs has been denoted as Y_{TDC}.

Another evaluation of the light speed inside the slats

The reconstruction code (described in detail in section 5.1) can provide information on the vertical coordinates of the impact points of the fragments on the ToF-Wall, using the data provided by the VTX detector: Y_{VTX}. This is useful because, by exploiting this information, it is possible to implement

a new evaluation of the light speed inside each slat.

Since the vertical coordinate should be independent from the method used to determine it, it is possible to write:

$$Y_{VTX} = Y_{TDC} = \frac{v_{light}}{2} * [(TDC_b - TDC_t) + (\Delta_t - \Delta_b)] =$$
$$= \frac{p_1 * v_{0;light}}{2} * [(TDC_b - TDC_t) + (\Delta_t - \Delta_b)] = p_1 * Y_{TDC;0} \quad (3.12)$$

defining $Y_{TDC;0}$ the vertical coordinate retrieved using TDCs and the value of the light speed $v_{0;light}$ measured as described in the paragraph "Y coordinate calibration". Equation 3.12 represents a linear relationship between Y_{VTX} and $Y_{TDC;0}$, therefore by plotting the two quantities one versus the other, the slope, p_1, can be determined. This parameter represents the ratio between the real speed value inside a slat with respect to the mean $v_{0;light} = 15.61$ cm/ns.

Figure 3.7 shows the plot of $Y_{TDC;0} vs Y_{VTX}$ for slat 46. In red, is superimposed the fit performed to retrieve the parameter p_1.

A plot like the one in figure 3.7 has been drawn for each slat. From it, the
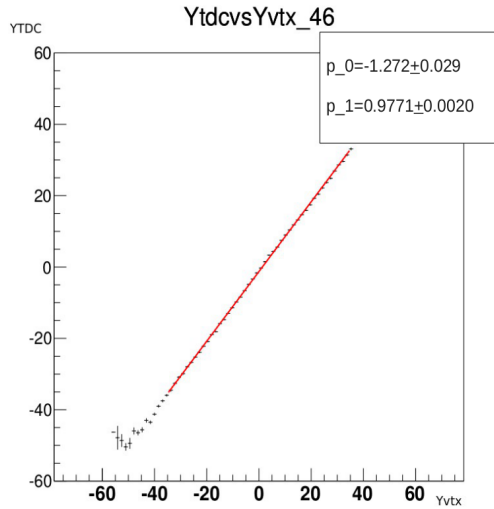
Figure 3.7: A plot showing the $Y_{TDC;0} vs Y_{VTX}$ curve, for slat 46. The linear fit is superimposed in red.

parameter p_1 and then the value of the light speed have been calculated for all the slats. In figure 3.8, the new values of the light speed, found trough this method as $v_{light} = p_1 * v_{0;light}$, are shown as a function of the slat number.
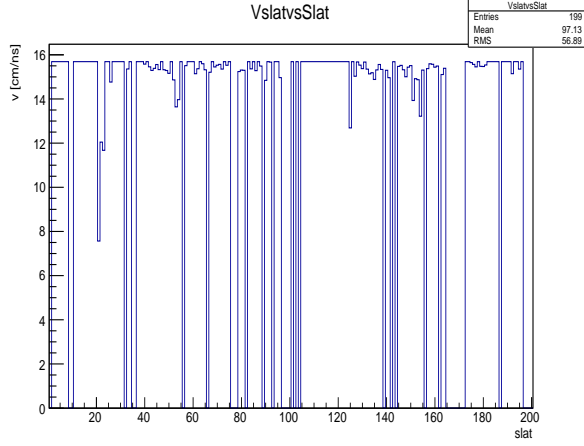
Figure 3.8: New values of the light speed as a function of the slat number.

Time of flight calibration

The Time of Flight (ToF) is the time spent by a particle to travel from the target to one TW slat. In order to calibrate the ToF measurements, the sweepruns have been used: in these runs the target is absent hence the fragmentation does not occur; therefore, during calibrations, the time spent by the ^{12}C projectiles from the SC to the TW is the ToF. Instead, when the fragmentation occurs, to calculate the ToF of fragments, a costant time offset, related to the fligth time of ^{12}C projectiles from the SC to the target must be subtracted, since the fragments are originated in the target and not in the SC.

The projectile trajectory depends on the ALADiN magnetic field, which deviates the ^{12}C ions according to their energy. In figure 3.9, the scheme of two trajectories from the SC to the TW for two different ^{12}C ions, is illustrated.

Considering the same quantities defined for the vertical coordinate calibration, the system 3.4 can be written again and holds also for the ToF calibration:

$$\begin{cases} TDC_t = ToF + \tau_t + \Delta_t \\ TDC_b = ToF + \tau_b + \Delta_b \end{cases} \tag{3.13}$$

By summing the two equations of the system and isolating the ToF term, the following equation is obtained:

$$ToF = \frac{1}{2}[(TDC_t + TDC_b) - (\tau_t + \tau_b) - (\Delta_t + \Delta_b)] \tag{3.14}$$

The term $(\tau_t + \tau_b)$ is a constant that represents the total time spent by the scintillation pulse to travel along the whole slat length.
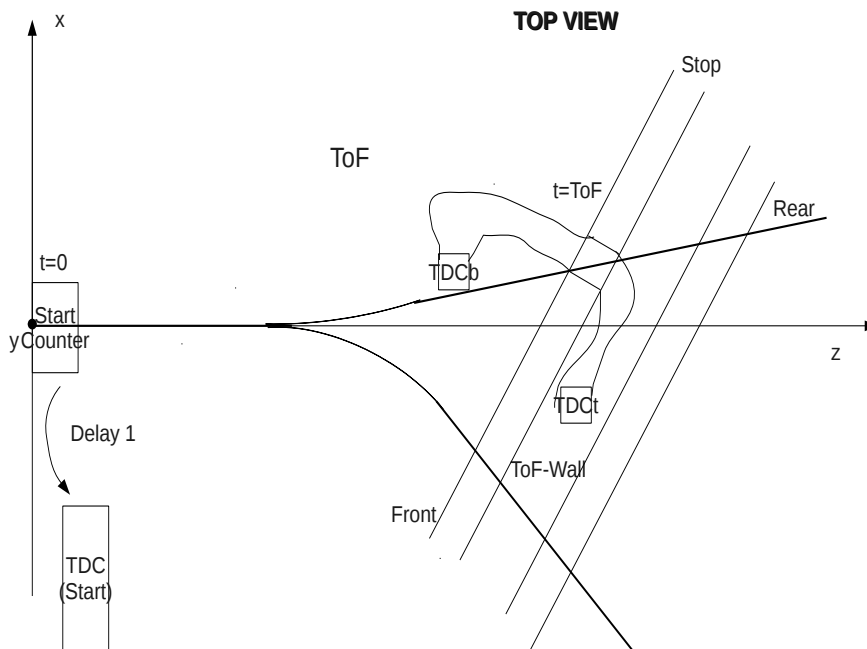
Figure 3.9: The diagram shows two different ^{12}C projectile trajectories, from the Start Counter to the ToF-Wall, during sweepruns.

Equation 3.14 shows that the ToF is equal to the mean time measured by both PMTs of the hit slat plus a constant offset:

$$\tau_0 = \frac{1}{2}[-(\tau_t + \tau_b) - (\Delta_t + \Delta_b)] \qquad (3.15)$$

This parameter can be evaluated when the particle trajectory and speed, and therefore ToF, are known. The data set provided by the sweepruns has been used for the ToF calibration; in those events the particle energy and therefore its velocity is known. In fact, in these runs, the target is absent and then the ^{12}C beam is not scattered, nor fragmented and maintains almost its initial energy ($E_k = 4.8$ GeV). The velocity of the ions is deduced from their kinetic energy as:

$$v = \beta c = c * \frac{\sqrt{(E_k + M)^2 - M^2}}{E_k + M} \qquad (3.16)$$

being M the ^{12}C ion mass.
To determine the trajectory followed to reach each slat, a geometrical reconstruction, exploiting an iterative calculation, has been developed. An

assumption of uniform, vertical magnetic field has been used. This hypothesis is a good approximation for the central trajectories and for the high energy projectiles. Therefore it can be applied to the ^{12}C ions not scattered by any target. Figure 3.10, represents the geometrical reconstruction of a ^{12}C trajectory in sweepruns.

If the target is not present, the ion direction of entrance into the magnetic
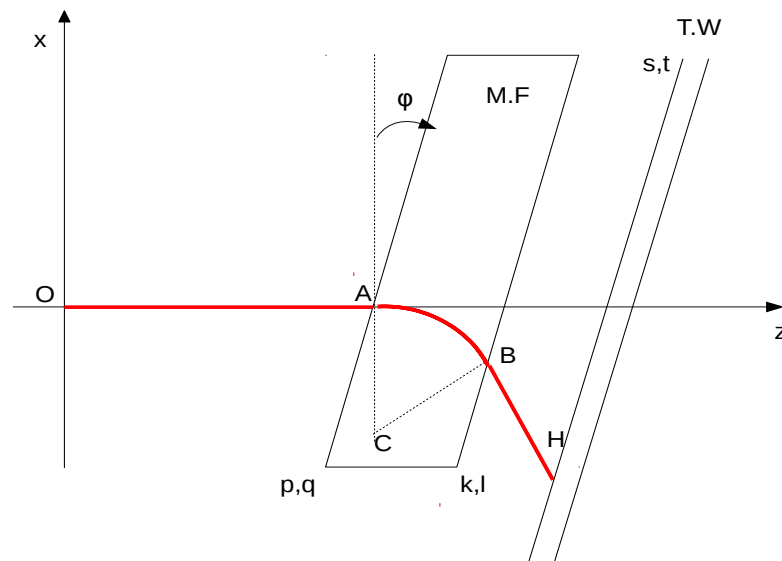
Figure 3.10: Sketch (not in scale) of a ^{12}C ion trajectory, in the sweepruns. In the picture, T.W.: ToF Wall; M.F.: Magnetic Field region.

field region is the z-axis (beam line). In the magnet, the trajectory is bent by the Lorenz force onto an arc of circumference from the entering point A to the exiting point B. The arc radius depends on the known magnetic field intensity. The path from B to the impact point onto the slat, H, is a segment. For every point B, there is one and only one arc AB, one center C and one impact point H. Point A is always the same and is known. In the geometrical reconstruction the slat of impact is known and then H is known too, within the uncertainty of the slat width. Therefore from geometrical properties, R and the point B can be reconstructed and the total Length of Flight, the so called LoF, i.e. the path OABH can be calculated for each slat.

Finally, the ToF can be easily calculated as:

$$ToF = \frac{LoF}{v} \qquad (3.17)$$

Inserting the values of ToF found in this way into the τ_0 equation (3.15), the calibration offset is determined and the quantity is calibrated.

The Time of Flight values, obtained through the geometrical reconstruction are reported, for each slat in figure 3.11.
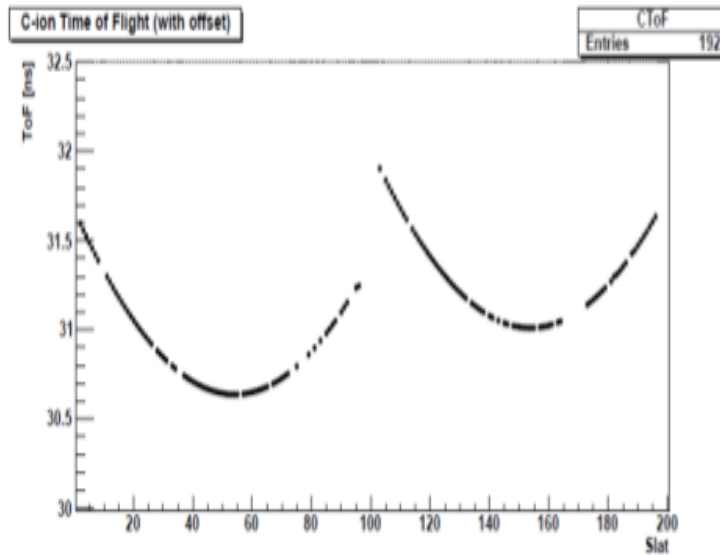
Figure 3.11: ToF (in ns) of the ^{12}C ions of the sweepruns vs slat number. Slats from 1 to 96 belong to the Front plane, from 100 to 196 to the Rear plane.

The distance between the Front and Rear planes is about 8 cm: therefore the trajectories related to the slats 100-196 are longer than the corresponding ones in the Front plane (1-96) and the ToF is longer. The associated time difference is clearly seen in the figure 3.11. The shape of both curves shows a minimum corresponding to the central slats of both planes (52-53 and 152-153).

The uncertainty of the Time of Flight distributions has been found to be ~400 ns, for all the slats.

The energy loss calibration

The energy released in a slat by a particle, E_{lost}, is a function of the particle energy E, charge Z, mass m and impinging angle ξ: E_{lost}(E, Z, m, ξ).

During the calibration runs the target is absent and only Carbon ions are present on TW. These ions release inside the slats, in average, the same energy; therefore, in the calibration process, it is possible to consider the scintillation light E_0, produced inside the slat, as directly proportional to the energy lost by the particles.

On the other hand, during the runs with target, the fragmentation process occurs. The produced fragments release a significantly different energy inside the slats, depending on their initial energy. In this case, the scintillation light, E_0, can not be considered proportional to the energy lost, E_{lost}, in the slat because of the non-linear effects in the plastic scintillators that become relevant when the energy losses are very different (as in the case of fragments). These effects can be corrected using the Birks' model [108].

According to Birks' law:

$$\frac{dE_0}{dx} = L_0 \frac{dE_{lost}/dx}{1 + k_b * dE_{lost}/dx} \tag{3.18}$$

where

- dE_0/dx is derived from ADC measurements

- dE_{lost}/dx is a theoretical value derived by the Bethe-Bloch formula

This law will be considered to correct the non-linear effects in the plastic scintillators during the charge identification process.

During calibrations, instead, the approximation according to which the scintillation light E_0, released inside the slat, is assumed as directly proportional to the energy lost by the particles, is applied.

In the slat, E_0 is split into two photon pulses of half energy $E_0/2$ propagating towards the 2 photomultipliers, PMT_t and PMT_b.

When the light, coming from the impinging particle point of impact on the slat, reaches the two PMTs at both ends of the scintillator bars, it arrives attenuated proportionally to the (different) travels along the slat. The two PMTs convert the received energies called E_{PMTt} and E_{PMTb} into electronic signals ADC_t and ADC_b. This is done through an electronic chain: the signals are amplified, transmitted to the ADCs and here converted into two digital values.

Recalling that Y is the vertical position of the impact point on the slat, L is

the slat length and defining α as the attenuation coefficient of the photons inside the scintillator, it is possible to write E_{PMTt} and E_{PMTb} as:

$$\begin{cases} E_{PMTt} \propto \frac{E_0}{2} * e^{-\alpha(\frac{L}{2}-Y)} \\ E_{PMTb} \propto \frac{E_0}{2} * e^{-\alpha(\frac{L}{2}+Y)} \end{cases} \qquad (3.19)$$

Figure 3.12 represents a sketch of the light propagation inside the slat.
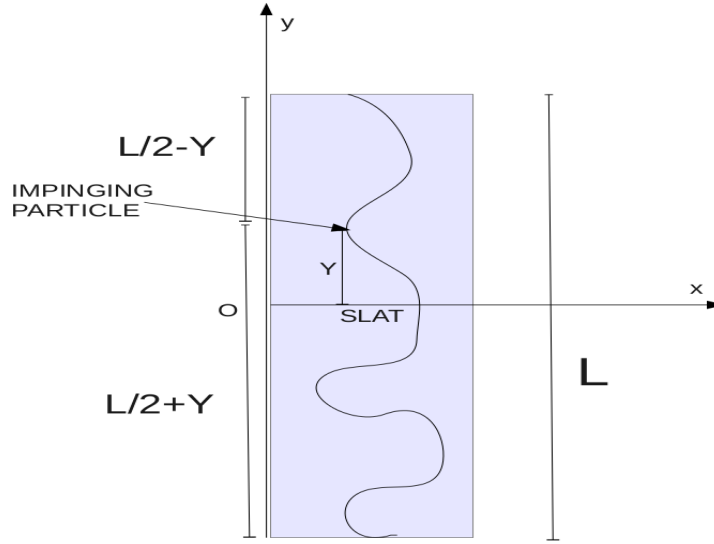
Figure 3.12: Sketch (not in scale) of the geometry in the photon attenuation process inside a slat.

The electronic signals into which E_{PMTt} and E_{PMTb} are converted, are ADC raw values. Each ADC measurement is proportional to the received signal through a gain factor; moreover they are shifted by an offset, called pedestal: it is the zero signal or dark noise level.
The two pedestal values: ADC_t^{Ped} and ADC_b^{Ped} must be subtracted to the ADC raw values in order to measure the energy release.
In figure 3.13 the pedestal peak, on the left hand side, and the Carbon peak, on the right hand side, for the top PMT of a single slat, are visible.

After the subtraction, the corrected ADC values, called ADC_t' and ADC_b' are obtained:

$$\begin{cases} ADC_t' \equiv ADC_t - ADC_t^{Ped} \\ ADC_b' \equiv ADC_b - ADC_b^{Ped} \end{cases} \qquad (3.20)$$
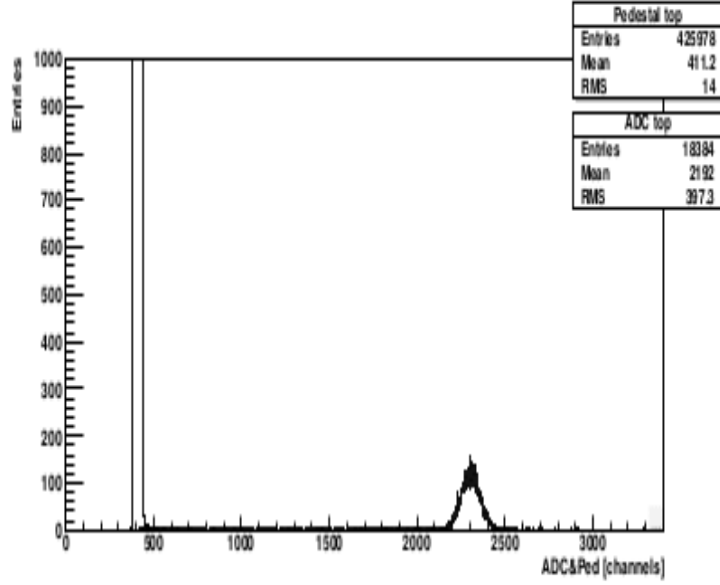
Figure 3.13: Plot showing the pedestal peak on the left hand side and the Carbon peak on the right hand side for the top PMT of a single slat.

These values are related to the particle energies through proportionality factors ϵ_t and ϵ_b:

$$\begin{cases} ADC'_t = \epsilon_t E_0 * e^{-\alpha(\frac{L}{2}-Y)} \\ ADC'_b = \epsilon_b E_0 * e^{-\alpha(\frac{L}{2}+Y)} \end{cases} \qquad (3.21)$$

ϵ_t and ϵ_b are gain/attenuation factors depending on PMTs and electronic chains.

The square root of the product of the two values, ADC'_t and ADC'_b, gives the deposited energy:

$$E_0 = K * \sqrt{ADC'_t * ADC'_b} \qquad (3.22)$$

$K = \frac{1}{\sqrt{\epsilon_t * \epsilon_b * e^{-(\alpha L)}}}$ is the calibration constant that has to be determined for each slat.

During the sweepruns, as already said, the target absence allows to know the type and the energy of the particles hitting the TW: ^{12}C ions at $E_k = 4.8 \ GeV$. Therefore it is possible, by using the Bethe-Bloch formula (described in equation 1.2) and taking into account the slat thickness, to find the average energy lost by the ions into the slat: $E_0^C \approx 116$ MeV. Starting from E_0^C it is possible to evaluate K, by inverting equation 3.22:

$$K = \frac{E_0^C}{\sqrt{ADC_t' * ADC_b'}} \tag{3.23}$$

For what concerns the pedestals, their evaluation was performed considering those events in which both the TDCs in a slat did not respond. These events are the ones in which there are no particles passing through the slat; in this case the ADC values represent the noise produced by the electronics i.e. the pedestal values.

The distribution of the pedestal values for each PMT (top and bottom) of each slat has been found. A Gaussian fit has been applied to each distribution peak. Since the peaks were not symmetric, the fit was adapted only to the left side (unphysical region) of the distribution. The fit mean value is taken as the pedestal. An example of pedestal distribution, with the Gaussian fit superimposed, is shown in the figure 3.14.
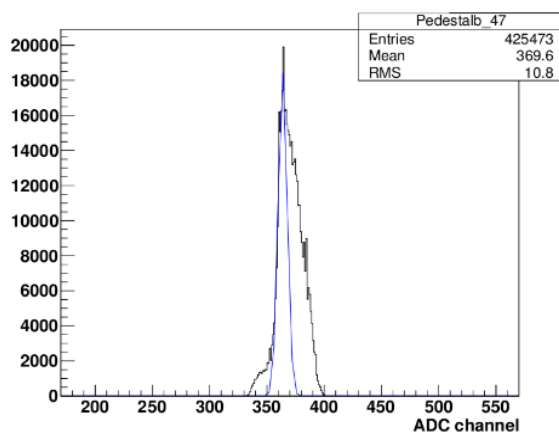
Figure 3.14: Distribution of the ADC values in the slat 47 (bottom PMT channel), in those events in which no TDC signal was observed. The solid line is the Gaussian curve fitted to the left channels, from 350 to 380.

3.2.2   3-channel calibration

This second type of calibration is performed when one of the TDC or ADC channels is not giving the measurement. Even if one channel is missing, it is anyway possible to perform a calibration of the quantities of interest thanks to the redundancy of information given by the dependence among TDC and ADC measurements. In particular, the vertical coordinate Y can be obtained not only through the TDC reading difference, as mentioned above, but also

using information coming from ADCs. Obviously, independently on how the quantity is evaluated, its measurement must be the same, excluding the uncertainties; calling Y_{ADC}, the vertical coordinate calculated through ADC channels, it must be:

$$Y_{TDC} = Y_{ADC} \qquad (3.24)$$

Starting from this condition it is possible to calibrate all the physical quantities, ToF, E_{lost} and Y, using only the 3 channels available: 1 ADC and 2 TDCs or the contrary.

To have the possibility of a second calibration is really useful, in fact, in this way it possible to perform the calibration also in those cases in which not all the 4 channels are responding; this can be due to:

- hits with under-threshold signal on 1 TDC
  (mainly protons – 20% statistics),

- slats with 1 failing channel.

Moreover, this provides a way to carry out a calibration cross-check. The calibration parameters ($\Delta_{t,b}$ and $\epsilon_{t,b}$) can be retrieved from both the methods and compared.

When one channel is missing, it can be an ADC or a TDC. Depending on the missing channel, the calibration procedure changes.

Case 1: a TDC missing

This is the case in which only one of the two TDCs is available while both the ADC readings are present and their signals are above the pedestals. In this situation the calibration of the energy loss is performed as described in the 4-channel calibration (see section 3.2.1) because the 2 ADCs are available; this is the only condition needed to evaluate the gain factor K:

$$K = \frac{E_0^C}{\sqrt{ADC_t' * ADC_b'}}$$

(being E_0^C the energy lost by the carbon ions into the slat, during the sweep-runs).

Instead, the procedure to calibrate the Time of Flight and the vertical coordinate is different due to the lack of the TDC channel.

The Y coordinate is calibrated and calculated starting from the logarithm

of the ratio of the 2 ADC readings (after pedestal subtraction), through the relationship:

$$Y_{ADC} = \frac{1}{2\alpha} \left(\log \frac{ADC'_t}{ADC'_b} + \log \frac{\epsilon_b}{\epsilon_t} \right) \qquad (3.25)$$

The calibration of the vertical coordinate requires the evaluation of two parameters: the attenuation coefficient inside the slat, α and the ratio of the PMT gain factors, $\frac{\epsilon_b}{\epsilon_t}$. The ratio $\frac{ADC'_t}{ADC'_b}$ is known because both the ADC readings are available.

The ToF, on the other hand, is calibrated and obtained using the vertical coordinate and the reading of the available TDC.
It can be written:

$$ToF = TDC_{t,b} - \frac{(L/2 - Y_{ADC})}{v_{ligth}} - \Delta_{t,b} \qquad (3.26)$$

When the vertical coordinate Y_{ADC} is calculated, $\Delta_{t,b}$ i.e. the time delay constant related to the TDC (top or bottom) at our disposal, is the only parameter missing in the ToF equation. The slat length L and the light speed inside the slat v_{ligth} are known together with the reading of 1 TDC ($TDC_{t,b}$). As in the case of the 4-channel calibration, during sweepruns, the ^{12}C ion speed is known; moreover, the flight path of the particle can be reconstructed using a geometrical iterative procedure. Therefore the ToF can be calculated (see equation 3.17).

The first step to perform this calibration is the evaluation of the unknown parameters for Y_{ADC}: α and $\frac{\epsilon_b}{\epsilon_t}$. These parameters can be found, for each slat, when all the TDC and ADC channels are available, because the vertical coordinate evaluation through TDCs is needed. Then the parameters can be used when 1 TDC channel is missing.
To find α and $\frac{\epsilon_b}{\epsilon_t}$, it is necessary to invert the equation 3.25 and to solve for $log\frac{ADC'_t}{ADC'_b}$:

$$\log \frac{ADC'_t}{ADC'_b} = 2\alpha Y_{ADC} - \log \frac{\epsilon_b}{\epsilon_t} \qquad (3.27)$$

Recalling equation 3.24:

$$Y_{TDC} = Y_{ADC}$$

it is also possible to write:

$$\log \frac{ADC'_t}{ADC'_b} = 2\alpha Y_{TDC} - \log \frac{\epsilon_b}{\epsilon_t} \qquad (3.28)$$

From this last equation turns out that the terms $\log \frac{ADC'_t}{ADC'_b}$ and Y_{TDC} are linked by a linear relationship in which 2α represents the slope and $\log \frac{\epsilon_b}{\epsilon_t}$ is the known term. Therefore, plots of $\log \frac{ADC'_t}{ADC'_b}$ vs Y_{TDC} were created, slat by slat, and fitted with a linear function. From the fit parameters, slope and known term, α and $\frac{\epsilon_b}{\epsilon_t}$ are determined.

An example of the plot representing $\log \frac{ADC'_t}{ADC'_b}$ vs Y_{TDC} with the linear fit superimposed is shown in figure 3.15.

In figure 3.16, the calculated parameters α (a) and $\frac{\epsilon_b}{\epsilon_t}$ (b) are shown for
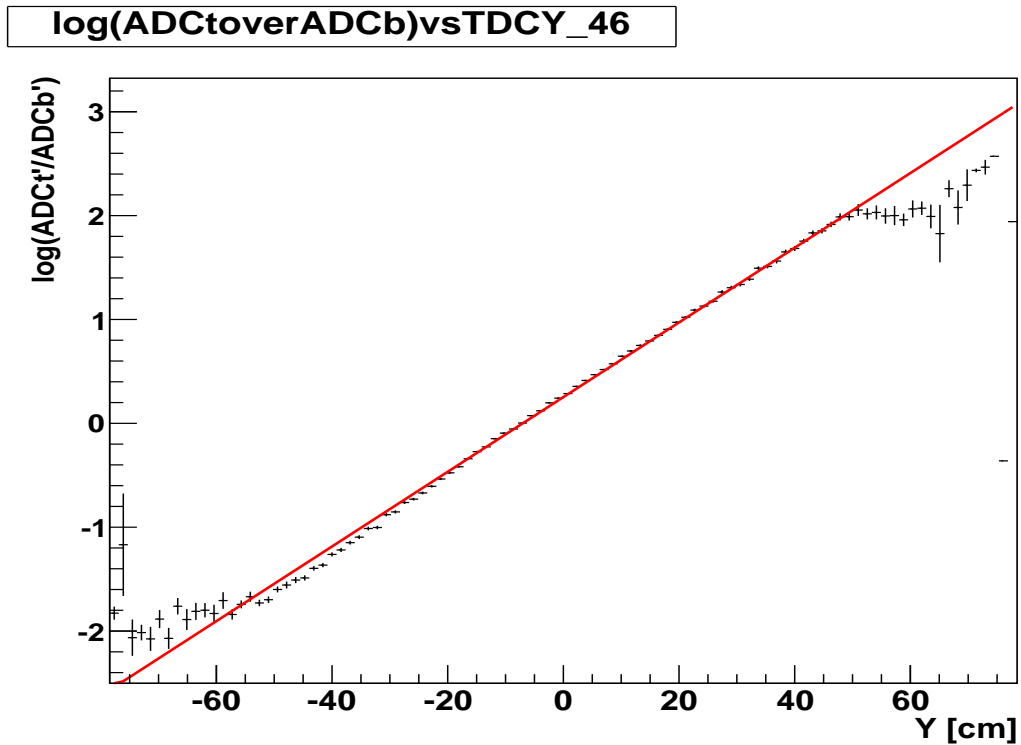
Figure 3.15: $\log \frac{ADC'_t}{ADC'_b}$ vs Y_{TDC} plot for slat 46. The linear fit is shown in red.

all the slats. Once the parameter values are established for all the slats, the quantity Y_{ADC} is calibrated and can be calculated using the equation 3.25. An evaluation of the resolution of this quantity has been carried out using the uncertainty propagation. The resolution found depends on the value of the vertical coordinate itself, as expected. Moreover it varies, slat by slat. Except few slats, it turns out to be lower than the one related to Y coordinate based on TDCs.
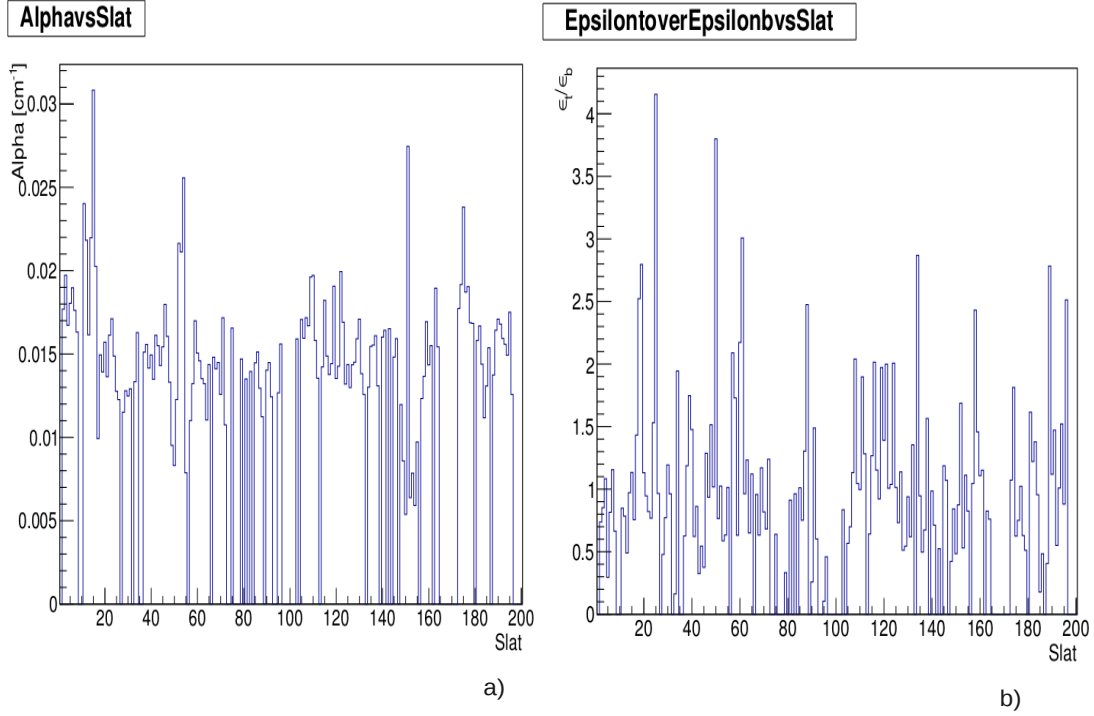
Figure 3.16: Parameters α (a) and $\frac{\epsilon_b}{\epsilon_t}$ (b) represented in function of the slat number.

When the vertical coordinate is known, the ToF calibration can be performed. Inverting the equation 3.26, the calibration parameter $\Delta_{t,b}$ can be calculated:

$$\Delta_{t,b} = TDC_{t,b} - \frac{(L/2 - Y_{ADC})}{v_{ligth}} - ToF \tag{3.29}$$

All the terms in the right part of the equation are known; therefore $\Delta_{t,b}$ can be evaluated.

These parameters have been found, for each slat, building their distributions using all the events in the sweepruns. Each distribution has been fitted by a Gaussian and the fit mean values have been assumed as the parameter values for the top and bottom delay constants in each slat. The uncertainties of the parameter evaluations are given by the fit standard deviations.

Figures 3.17 and 3.18 show the top Δ_t and bottom Δ_b parameter distributions for one slat, as an example. The Gaussian fit is superimposed in blue.
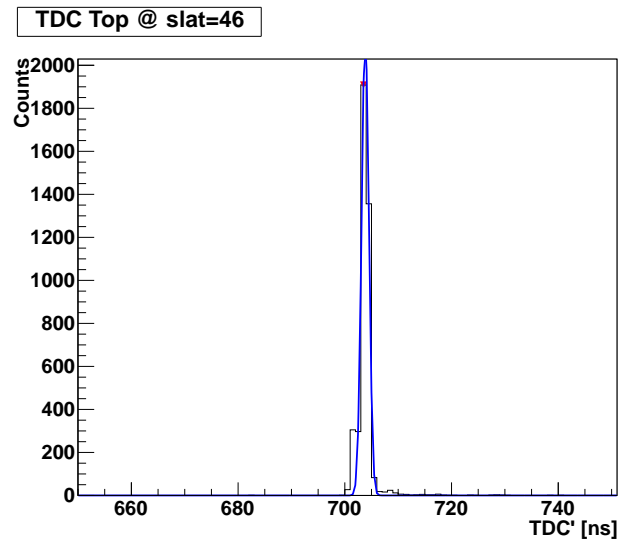
Figure 3.17: Δ_t parameter distribution for slat 46. The blue curve shows the Gaussian fit.
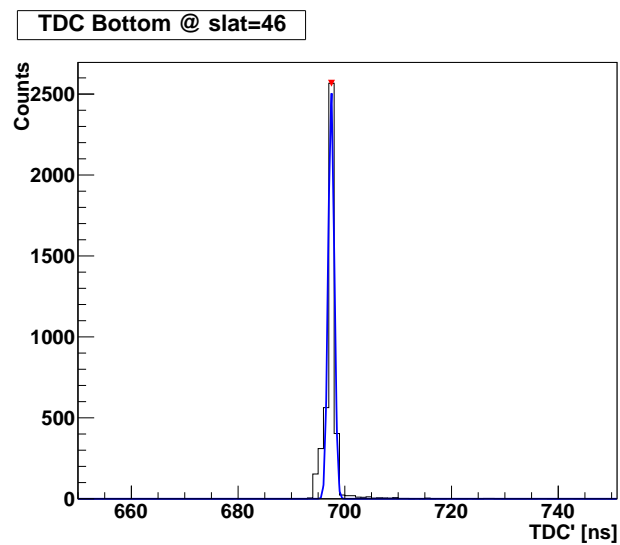
Figure 3.18: Δ_b parameter distribution for slat 46. The blue curve shows the Gaussian fit.

Case 2: an ADC missing

In this case, the two TDC channel measurements are available. Instead, one ADC reading is missing while the other has the signal above the pedestal. Since both the TDCs are available, in this case the ToF and the vertical co-

ordinate can be calibrated as in the 4-channel calibration (see section 3.2.1).

The energy loss, on the contrary, must be calibrated following another procedure. This quantity is calculated and calibrated starting from the Y coordinate and the reading of the available ADC (top or bottom, $ADC'_{t,b}$). The equation that describes the energy released in the slat by a particle, E_0 is the following:

$$E_0 = \frac{ADC'_{t,b}}{\epsilon_{t,b}} * e^{\alpha*(L/2 \mp Y_{TDC})} \qquad (3.30)$$

The reading of one ADC after pedestal subtraction ($ADC'_{t,b}$) is available, together with the vertical coordinate, the slat length and the attenuation coefficient (α). Moreover, using the sweepruns, the energy loss by carbon ions in the slat is known: E_0^C=116 MeV. Therefore, it is easy to find the only unknown parameter, $\epsilon_{t,b}$, the gain factor of the PMT corresponding to the available ADC:

$$\epsilon_{t,b} = \frac{ADC'_{t,b}}{E_0^C} * e^{\alpha*(L/2 \mp Y_{TDC})} \qquad (3.31)$$

ϵ_t and ϵ_b have been found, slat by slat, building their distribution using all the sweeprun events. All the distributions have been fitted using a Gaussian. The fit mean values have been assumed as the parameter values for the top and bottom PMT gains for each slat; the fit standard deviations, moreover, are an evaluation of the uncertainty on the parameters.

3.3 The fragment charge identification

When considering the runs with the ^{12}C beam impinging onto the target, effects due to both fragmentation and scattering of the projectile are present. In this case we can expect six different kinds of ions impinging on ToF-Wall: H, He, Li, Be, B and forward scattered or not interacting C, whose atomic numbers are Z=1,2,3,4,5,6 respectively.
Fragments with different charge Z produce different energy loss in the slat. The ToF-Wall performances are good enough to allow the discrimination of six well separated spots in the ToF-E_{lost} plane (where ToF is the Time of Flight and E_{lost} the energy released in the slat). The spots clearly corresponds to H, He, Li, Be, B fragments and to the scattered or not interacted C.
In figure 3.19 an example of the Time of Flight versus energy loss plot, showing the six spots, is available for a central slat (47).
The six spots, quite separated along the energy loss axis, have similar (but not equal) spread along the ToF axis. In fact, the particle forwardly emitted
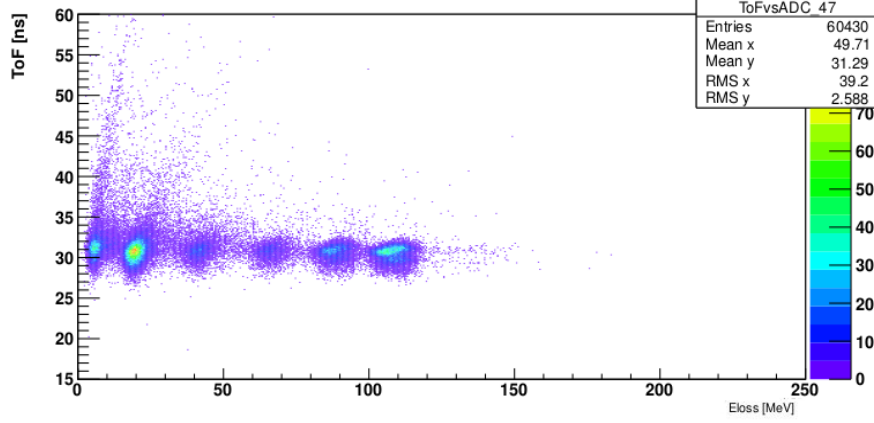
Figure 3.19: $ToFvsE_{lost}$ plot for a central slat. The 6 spots, corresponding to different ions, are clearly distinguishable.

in the fragmentation are very energetic with linear momentum close to the projectile one. Therefore, their velocities do not differ much from each other, as well as the length of their trajectories, because the geometrical acceptance of ToF-Wall is small ($\approx$1 msrad) over a long (about 6.5 m) target-detector distance. In conclusion the ToF values of all different fragments mainly spread in similar time intervals.

On the contrary, the energy loss depends on the entrance velocity and strongly on the charge of the ion ($\propto Z^2$). In this way different ions are separated along the energy loss axis and the separation is as clearer as Z is higher.

In principle, to perform the charge identification, each spot should be fitted using the Bethe-Bloch formula (equation 1.2) with Z corresponding to the spot charge. However, when comparing measured data and expected values (from the Bethe-Bloch formula) in $ToFvsE_{lost}$ plots emerges that data distribution and theoretical curves disagree (see figure 3.20). This is due to the non-linear effects in the plastic scintillators; therefore, as anticipated in section 3.2.1, the Birks' model must be used to correct for these effects.

As can be seen from the Birks' law (equation 3.18), it is possible to deduce the released energy, E_{lost} from E_0:

$$\frac{dE_{lost}}{dx} = \frac{dE_0/dx}{L_0 - k_b * dL/dx} \tag{3.32}$$

L_0 and k_b parameters, the luminescence at low specific ionization densities and the Birks constant respectively, can be retrieved from fitting the energy peaks related to particle with different charge Z, mass m and known energy to the values given by the Bethe-Bloch formula. Once the parameters are
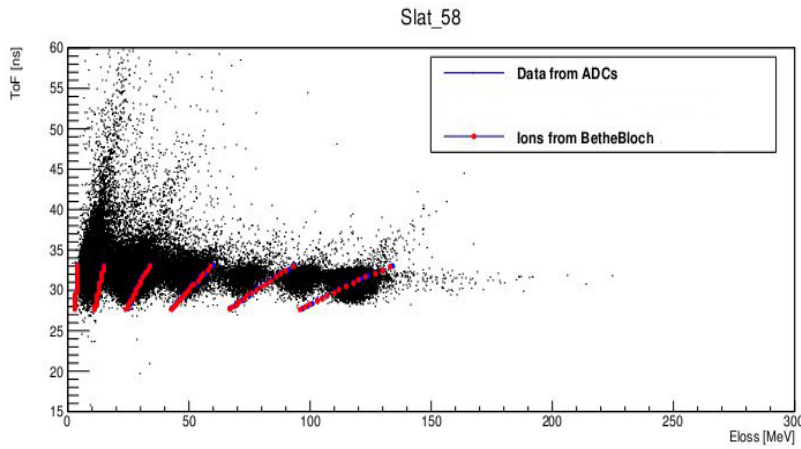
Figure 3.20: ToF vs E_{lost} plot showing the 6 spots for one slat (58), together with the Bethe-Bloch curves superimposed.

known, a rescaling of the energy axis can be applied to overlap distributions with theoretical curves.

Figure 3.21 shows the comparison between the data and the theoretical Bethe-Bloch curves after the correction using the Birks' model. From figure
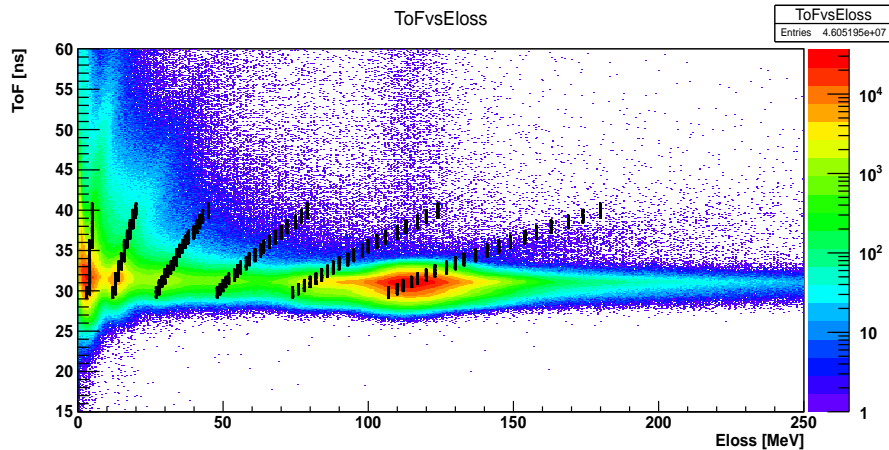
Figure 3.21: ToF vs E_{lost} plot showing the 6 spots (for all the slats) with the Bethe-Bloch curves superimposed (the black columns are due to different isotopes), after the non-linear effect correction.

3.21 it can be seen that, after the correction from the non-linearity effects, the data agree in a good way with the Bethe-Bloch curves.

Another plot showing the measured distributions of the fragments resulting

from ^{12}C ions on carbon target interactions, in the plane $(E_{lost} - ToF)$, with Bethe-Bloch curves superimposed in black, is shown in figure 3.22.
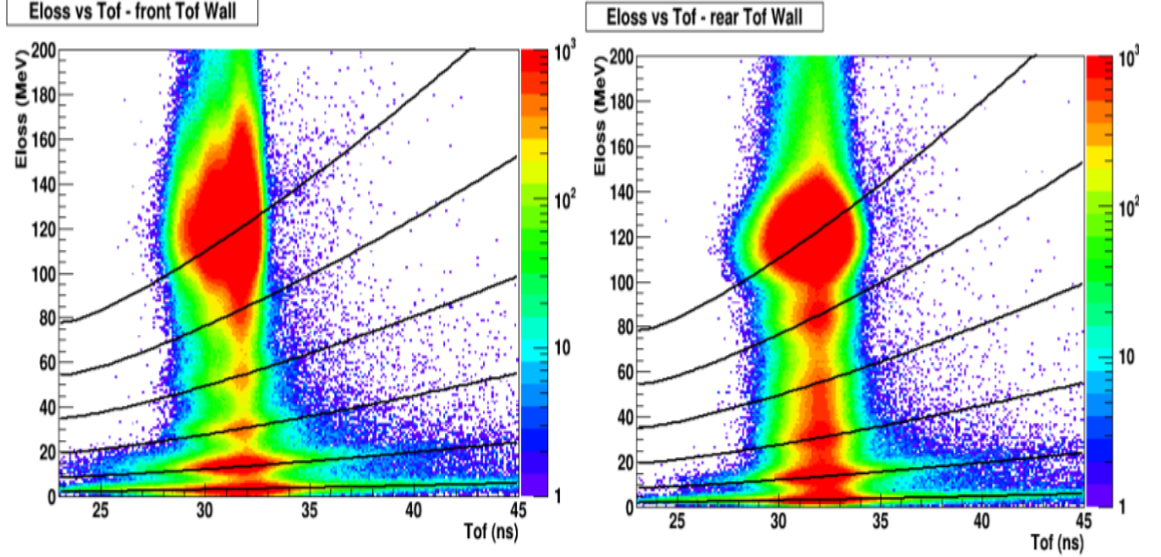
Figure 3.22: E_{lost} vs ToF plot for the Front Wall (left) and for the Rear Wall (right) slats. The Bethe-Bloch curves are superimposed in black.

For the charge assignment to each fragment, characterized by the energy released in the ToF-Wall and by the measured Time of Flight, the minimum distance between the point representing it in the $(E_{lost} - ToF)$ plane and the 6 Bethe-Bloch curves is calculated. Six distributions of the distances of each fragment coordinates $(E_{lost} - ToF)$ from the closest Bethe-Bloch curve are obtained. In figure 3.23 examples of the distance distributions from the six Bethe-Bloch curves for all the fragments (i.e. particles different from carbons, $Z \neq 6$) are available, with the condition of VTX-BM matching, i.e. excluding pile-up events. As can be seen in figure 3.23, the peak corresponding to the distance distribution from each given Bethe-Bloch curve, related to a particular kind of fragment (H, He, Li, Be, B), is centered to 0.
Then a Gaussian fit is applied to the plots, from which it is possible to retrieve the mean value μ_{dist} and the sigma σ_{dist} for each distance distribution. For each TW hit, the identification algorithm computes the normalized distance:

$$\frac{distance - \mu_{dist}}{\sigma_{dist}} \tag{3.33}$$

from the 6 different curves.
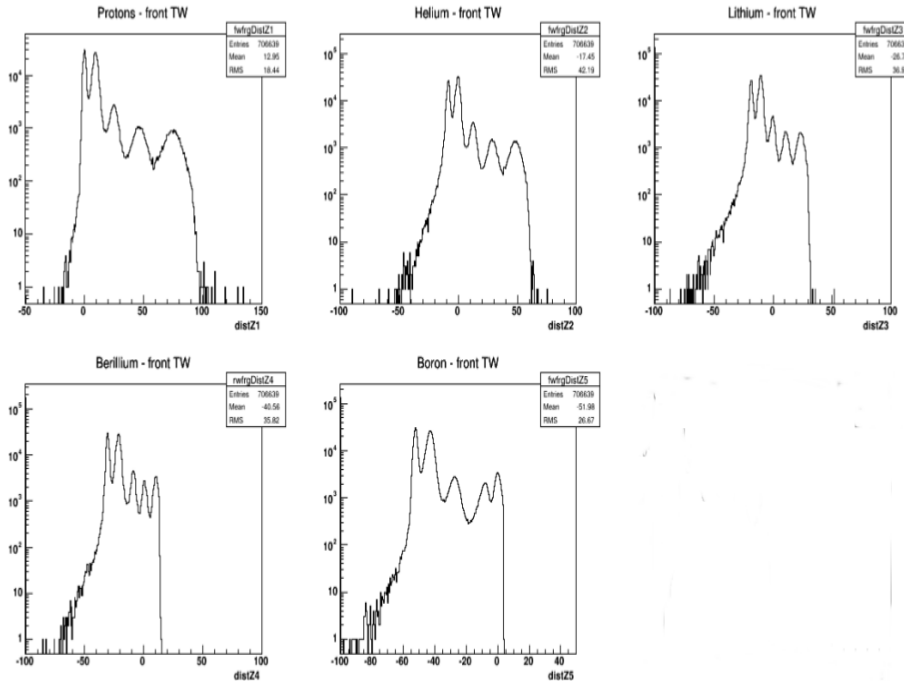
Figure 3.23: Distance distributions for fragmentation events (Z=1-5) in the Front Wall.

The Z assigned to a particle is the one corresponding to the Bethe-Bloch curve that minimizes the quantity in equation 3.33.

The minimization algorithm used is the so called "bisection method" [109]. This algorithm has the important advantage to always converge in the ToF interval where the method is applied.

Figure 3.24 shows the results of the charge identification method adopted. After the minimization process, all the fragments identified with a particular Z are plotted in the ($E_{lost} - ToF$) plane, separately from the other charge fragments. It can be noticed that the charge selection method works in a satisfactory way; the different fragment spots are recognized and well distinguished from each other.

3.4 Preliminary results on the scattered ^{12}C analysis

In order to test the goodness of the calibrations performed on ToF-Wall, a preliminary analysis of Single Coulomb Scattering (SCS) events has been carried out.
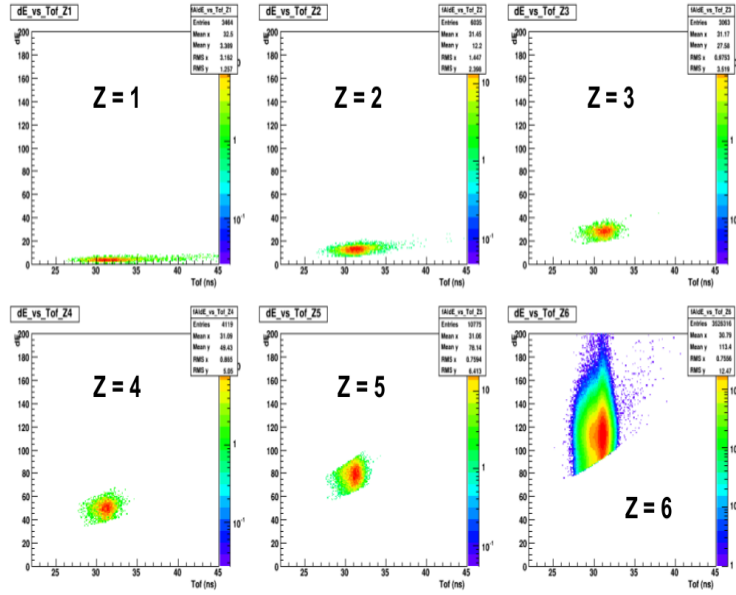
Figure 3.24: $E_{lost} vs ToF$ distributions for the different Z spots, selected with the charge identification process.

Using the charge identification process described in the previous section, only the ^{12}C ions detected by the Front Wall of the TW were selected. This kind of ions, due to their small lateral spread, can hit only the central TW slats, from 38 to 68. This slat range on TW, after the ALADiN deflection, corresponds to a polar angle (θ) of about 4 deg (≈ 0.07 rad), over a path length of approximately 6.5 m, at the exit of the target (before the magnetic deflection).

In order to perform the analysis, an approximation on the track direction has been used: the projectile deflection has been assumed to be constant inside the magnetic field region. This implies that the same impact distribution on TW would be obtained switching off the magnetic field and shifting the ToF-Wall in such a way that its center falls under the prosecution of the beam direction (z-axis), resulting perpendicular to it. In practice, since the trajectories of the ions considered in the analysis are actually close to each other, the particle flight paths were assumed as straight lines, considering negligible the change of polar angle due to the magnetic deflection. The error on the polar angle θ, due to this approximation, is lower than about 10%. It depends on the energy of the ^{12}C beam. In principle, projectiles that have lost more energy are bent more by the magnetic field and reach the rightmost slats, giving rise to a tail in the impact point distribution of carbons on TW.

In order to ensure that the approximation on the angle holds, the slat range considered in this study was limited to the left side of the C impact point distribution on the TW i.e. to slats from 1 to 51, corresponding to polar angles in the interval $0.2 - 4.5$ deg ($\approx 0.0035 - 0.0785$ rad).

For what concerns the particle energy, in this small θ range, it is quite close to the primary beam one, because the analyzed carbon ions are elastically scattered in a very forward direction. The error in assuming the scattered particle kinetic energy equal to the one of the beam ions ($E_k = 4.8$ GeV) is less than 0.2%.

For each ion, the angle θ was calculated through the formula:

$$tan\theta = \frac{\rho}{LoF} \tag{3.34}$$

where $\rho = \sqrt{X^2 + Y^2}$, being X the coordinate of the hit slat center, Y the impact point vertical coordinate and the LoF (Length of Flight) the particle path length calculated through a geometrical reconstruction.

The impact point distribution of ^{12}C ions has been evaluated over the solid angle as a function of the polar angle θ. The scattering process has a cylindrical symmetry over the azimuthal angle ϕ, then the differential cross section for SCS $\frac{d\sigma}{d\Omega}$ is ϕ independent: $\frac{d\sigma}{d\Omega}(\theta)$. Thus the impact point distribution has been evaluated over the solid angle $\Delta\Omega$ included between two cones of aperture $\theta - \frac{\Delta\theta}{2}$ and $\theta + \frac{\Delta\theta}{2}$, being $\Delta\theta \simeq atan(\frac{\Delta\rho}{LoF})$ and $\Delta\rho = 2.5$ cm. In this configuration (see figure 3.25), the solid angle is given by:

$$\Delta\Omega \propto \Delta(cos\theta) \tag{3.35}$$

The number of particles (ΔN) falling into the solid angle taken into account is related to the SCS differential cross section $\frac{d\sigma}{d\Omega}(\theta)$, to the number of used projectiles N_0 (i.e. the primary beam number of particles, integrated over the run time), to the slat efficiency ϵ, to the solid angle itself and to the target (8 mm carbon) features i.e. density, thickness and mass number (ρ, s and A):

$$\Delta N = N_0 * \rho * s * \frac{N_A}{A} * \frac{d\sigma}{d\Omega}(\theta) * \Delta\Omega * \epsilon \simeq N_0 * \rho * s * \frac{N_A}{A} * \frac{d\sigma}{d\Omega}(\theta) * \Delta(cos\theta) * \epsilon \tag{3.36}$$

(N_A is the Avogadro's number).

The major contribution in the distribution is expected to be the SCS cross section, proportional to $\frac{1}{sin^4(\frac{\theta}{2})}$, according to the Rutherford formula [110].

Figure 3.26 shows the behavior of the quantity $\frac{\Delta N}{\epsilon\Delta cos(\theta)}$ as a function of the polar angle (expressed in radians). The function $\frac{K}{sin^4(\frac{\theta}{2})}$ is superimposed
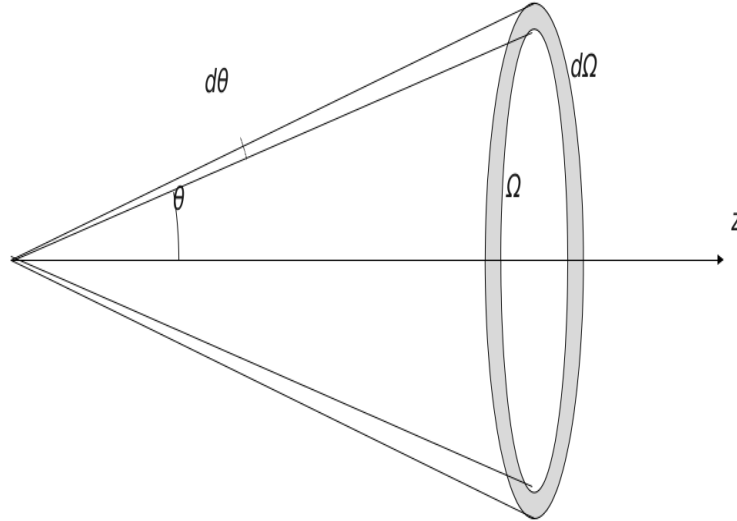
Figure 3.25: Solid angle configuration sketch.

in red. K represents the factor, which normalizes the experimental value $\frac{\Delta N}{\epsilon \Delta cos(\theta)}$ to the theoretical function in the smallest angle considered θ=0.0076 rad (corresponding to ≈0.436 deg).

The experimental points are in good agreement with the curve $\frac{K}{sin^4(\frac{\theta}{2})}$, within the errors. Therefore, it is confirmed that the coulomb scattering is the highly dominant interaction of ^{12}C projectiles on a ^{12}C target.

The data follow the expected behavior. This can be considered a satisfactory validation of the TDC and ADC calibrations.
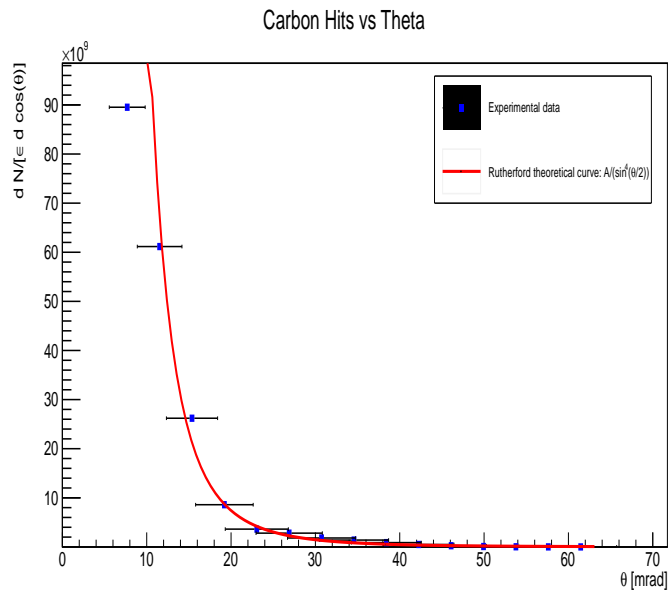
Figure 3.26: Plot of $\frac{\Delta N}{\epsilon \Delta cos(\theta)}$ (blue dots), together with the function $\frac{K}{sin^4(\frac{\theta}{2})}$ superimposed in red. Error bars take into account the statistical errors on the event numbers and the approximation effects.

Chapter 4

Monte Carlo simulation

4.1 The Monte Carlo simulation in FIRST

The Monte Carlo (MC) simulation developed for the FIRST experiment is built for several purposes, from the design and optimization of the experimental setup to the support for the reconstruction software development. In fact the simulation code is able to provide the simulated detector response data of an event. Moreover, it is fundamental in evaluating acceptances, reconstruction efficiencies and other kind of systematics.

The implementation of the simulation can be divided into different sectors: they concern the description of the experimental setup (beam path, detector layouts, parameters describing magnetic field) and of each sub-detector (geometry, materials, modeling of response and digitization); the particle transport and retrieval (scoring) of basic physical quantities of the tracks (i.e., primary particles and created secondary particles which are propagated through the detector geometry) and hits (i.e., energy depositions of tracks in sensitive detector elements); the storing of simulated tracks, hits and detector signal data for further processing and analysis.

For what concern the experimental setup, all the detectors and the ALADiN magnet have been implemented in the simulation with a considerable detail, considering their positions, the whole geometry and all the materials (including, for example, the vacuum windows or the air and gas mixtures crossed along the fragment paths). This is necessary to properly evaluate the interactions in all the active detectors and the production of secondary particles in out-of-target fragmentation processes.

The absolute positions of the detectors in the experimental area are fixed on the basis of the results of optical survey measurements performed at the end of the data taking, complemented with alignment studies from the collected

data.

The FLUKA (FLUktuierende KAskade i.e. Fluctuating Cascade) code is able to simulate in a fairly tolerable way the interactions (with the exception of the fragmentation cross sections) of the ions with the detectors in the experimental setup. However, some effects like the different sensitivity in the VTX pixels, the discrimination thresholds in each CFD (Constant Fraction Discriminator), the lack of uniformity/inefficiencies in the TW slats or the differences in the PMT gains in the TW slats and in the barrel of KENTROS can not be simulated by FLUKA. Therefore, they are determined from measurements and parametrized for the simulation. This results in a reduced computational effort and a decreased overall complexity of the simulation, while preserving its predictive power at a reasonable level.

The detailed MC simulation of the geometry and of the detector response, furthermore, is needed to evaluate efficiencies and resolutions[1] for the cross section measurement. For this purpose, the reconstruction code has been run also on MC events: each reconstructed track[2] is associated with the actual MC generated track; the reconstructed variables (kinetic energy, mass, charge, emission angle, momentum) are then compared with the corresponding actual values at the generator level. A MC sample of 24 million events of ^{12}C ion interactions with a carbon target has been used for this purpose.

4.1.1 The FLUKA code

The FIRST simulation exploits the multi-purpose FLUKA Monte Carlo code to simulate the particle transport and interactions with matter. In fact, FLUKA has been considered acceptable in the energy range of FIRST, to design the experiment, both for the description of electromagnetic processes and to provide a modeling of nuclear interactions (10% of uncertainty) [53, 111]. Nevertheless, large corrections are expected from the analysis of the data collected within the experiment FIRST, for what concerns the absolute values of Double Differential Cross Sections in angle and kinetic energy.

FLUKA [49] is a tool developed by CERN and INFN. It covers an extended range of applications spanning from proton and electron accelerator shielding to target design, calorimetry, dosimetry, detector design, radiotherapy.

This code is based, as far as possible, on original but well tested microscopic models. Due to this "microscopic" approach, each simulation step is self-consistent and has solid physical bases. Final predictions are obtained with a minimal set of free parameters, fixed for all energies and target/projectile

---

[1]In section 5.1.2 an explanation about the evaluation of these efficiencies and resolutions will be provided.

[2]The reconstruction algorithm will be described, in details, in the next section.

combinations.

The FLUKA code is able to simulate the transport of more than 60 types of particles, in addition to heavy ions.

The energy range covered for hadron-hadron and hadron-nucleus interactions is up to 10000 TeV, while the energy range for the electromagnetic and μ interactions varies from 1 keV up to 10000 TeV. The cross section data sets developed in FLUKA for neutron transport and interactions below 20 MeV down to thermal energies are based on standard evaluated databases (ENDF/B-VI or ENDF/B-VII [112] , JENDL [113], JEFF [114]).

For the FIRST experiment MC simulation, it has been chosen the recommended configuration for hadrontherapy ("HadronTherapy") for what concerns the interaction models for electromagnetic and nuclear processes relevant for the transport of both primary and secondary particles. It includes accurate simulations of non-elastic hadronic interactions at low energy and the evaporation and radioactive decays of heavy fragments. Moreover, neutrons are tracked down to thermal energies while electromagnetic physics is described within the EMF (ElectroMagnetic Fluka) package, which takes into account energy loss, straggling and multiple Coulomb scattering of charged particles.

During heavy ion collisions, nuclear processes vary depending on the energy. In the energy range of interest for therapeutic purposes, the mechanisms of interaction extend from pure fragmentation at high energy to more complex processes like Coulomb Scattering, fusion or deep inelastic processes at lower energies. This kind of processes are described, in the FLUKA code "HadronTherapy", taking advantage of interfaces with the rQMD (relativistic Quantum Molecular Dynamics) [115, 116] or with the new BME (Boltzmann Master Equation) [117] event generator, according to the energies considered. The relativistic Quantum Molecular Dynamics model, in particular, is used for ion projectile energies from 5 GeV/n down to 100 MeV/n; for lower energies, instead, the model based on the Boltzmann Master Equation theory is used to describe hadronic interactions.

The rQMD model

The Quantum Molecular Dynamics (QMD) approaches are a viable solution for nucleus-nucleus reactions because they represent a suitable way to describe the initial hot stage of heavy ion reactions.

However, sometimes the initialization of the projectile/target nuclear states can be difficult, especially considering the extension to relativistic regimes.

The rQMD-2.4 is a relativistic model, which has been applied successfully to relativistic particle production over a wide energy range, from about 100

MeV/n up to 5 GeV/n. This model combines the classical propagation of the hadrons (molecular dynamics) with some quantum effects such as stochastic scattering, particle decay, and Pauli blocking in collisions.

The main difference from the the non-relativistic QMD event generator is that a nucleus-nucleus collision model in the ultra-relativistic energy domain must be Lorentz invariant. Non-relativistic model results become, with growing energies, more and more observer frame dependent. Therefore, in rQMD models, the classical Hamiltonian is substituted by Lorentz invariant equation of motions.

Particularly, the rQMD nucleus-nucleus model in the energy range of interest for hadrontherapy, is an extension of the non-relativistic quantum molecular dynamics approach successfully used to study heavy ion collisions at low and medium beam energies $E_k = 50$ - 2000 MeV/n [118]. This code explicitly follows the trajectories of all hadrons (including the produced particles) and provides the full information about the dynamical evolution of all the particles in the phase space.

The BME model

An event generator based on the Boltzmann Master Equation (BME) approach is implemented for simulating heavy ion inelastic interactions in the energy range below the rQMD lower limit (100 MeV/n). This is needed to properly simulate the stopping processes involving heavy ion beams which are employed in radiation therapy.

The BME is a nucleon transport model based on nucleon-nucleon collision processes in the nuclear potential.

There are several mechanisms that can occur in heavy ion-target interactions, in the energy range of interest: break-up of the projectile and the target, inelastic scattering or thermalization process i.e. the formation of non-equilibrated nuclei reaching a state of thermal equilibrium through a sequence of two-body interactions leading to the emission of fast particles. The BME model, in particular, describes the de-excitation process of the non-equilibrated nuclei, which may be created through the previously explained mechanism (thermalization).

The description is given through the statistical evolution of the system studied, which changes from an initial state, far from the equilibrium, to the equilibrium state. This evolution follows a sequence of two-body interactions, with the emission of unbound particles [119]. The equilibrated system is produced (i.e. the process of de-excitation ends) when the probability of fast particle emission becomes negligible. The thermal equilibrium states, fi-

nally, further de-excite by evaporation of particles and γ-ray emissions until a cold residual nucleus is formed.

Moreover, other physical phenomena are described using other kind of models, for example: the de-excitation of the excited fragments is processed with the FLUKA evaporation/fission/fragmentation module; instead hadron-nucleus interactions are described by the PEANUT (PreEquilibrium Approach to NUclear Thermalization) model [49] which includes an intranuclear cascade stage followed by a pre-equilibrium stage and then equilibrium particle emission. Finally, total nuclear reaction cross-sections are calculated using an empirically modified version of the Tripathi parametrization for nucleus-nucleus interactions [115, 120].

4.2 Comparison between data and MC

The calculation of the cross sections, which is the final aim of the FIRST experiment, can not be performed without the contribution of the MC simulation. In fact, some of the quantities needed for the cross-section evaluation can be estimated only through Monte Carlo (see section 6). It is thus necessary to understand if the simulation estimates are reliable for the experimental purposes. Therefore, it is important to evaluate the agreement among the simulation results and the quantities of interest calculated starting from data.

Figure 4.1 shows an example of data-MC comparison for the distributions of two of the TW quantities of interest: Time of Flight and vertical coordinate. Both the quantities are of fundamental importance in the cross section calculations. The Time of Flight is involved in the evaluation of the fragment mass (see equation 5.5) thus its resolution influences the evaluation of the mass resolution and hence the possibility to distinguish the isotope distributions. The vertical coordinate, instead is one of the physical quantities used, in the global reconstruction (see section 5.1), to give a score to the track matching and then to establish the best combination among VTX tracks and TW hits. It is thus crucial in the tracking efficiency estimation.

It is therefore really important for the MC code to reproduce in a appropriate way the behavior of the distributions of these two quantities. The agreement among the MC simulation of Y and ToF distributions and the distributions deriving from data is an indication of the MC ability in reproducing the experimental setup.

Distributions in figure 4.1 are obtained using the so called "fragmentation events", i.e. events for which at least one vertex has been reconstructed in

the VTX detector and more than one track is associated to it. As can be
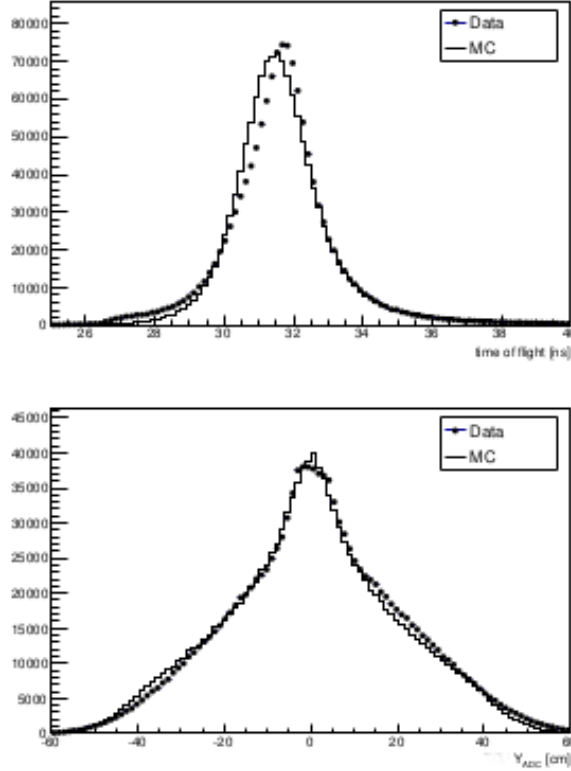
Figure 4.1: Comparison of data and MC distributions for TW reconstructed variables: Time of Flight (upper part) and vertical coordinate (lower part). The data and MC spectra have been normalized in order to have the same integral.

seen in the figure, the MC code is able to well recreate the behavior of the two distributions, Y and ToF, both in the peak and in the tails. Therefore the MC reproduces well the behavior of the TW detector.

Figure 4.2 illustrates the MC-data comparison for another TW relevant quantity: the energy loss. Also in this case the distributions have been obtained using fragmentation events. In these distributions, a good agreement can be noticed for what concerns the 6 peak width. This means that the MC code manages to reproduce, in a way that can be consider satisfactory, the energy loss resolution for all the 6 ions. Instead, the consistency in the peak height, in particular for the highest charges, is not as good as desired. However, this disagreement was expected, because the peak height represents the number of fragments for each type (H, He, Li, Be, B) and the evaluation
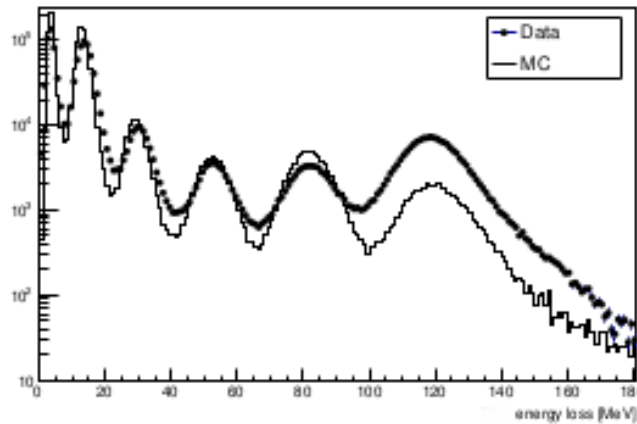
Figure 4.2: Comparison of data and MC distribution of the TW reconstructed energy loss. The data and MC spectra have been normalized in order to have the same integral.

of the number and kind of fragments produced, together with their angular and energy distributions, is the goal of FIRST. The experiment, in fact, has been planned in order to obtain the fragmentation cross section for ^{12}C ions at 400 MeV/n, among other motivations, because this information lacks in simulation codes such as FLUKA. Therefore, the predictions of the simulation code, for what concerns the number of fragments produced, will not be in agreement with the experimental distributions until the proper cross sections will be inserted in the FLUKA simulation, as parameters for the physics of nuclear fragmentation. Finally, it has to be noticed that the figure shows distributions in which the requirement of fragmentation events, only, has been adopted. This means that, for data, the peak around 120 MeV can not correspond to ^{12}C ions. However, this excess of carbons in the energy loss distribution, for data, can be explained as the result of several phenomena:

1. events in which the matching of tracks from the VTX detector and the TW hits is failing;

2. ^{11}C fragments;

3. pile-up carbon tracks (about 1%) that can be wrongly associated to a fragmentation vertex.

Another aspect in which the MC simulation must reproduce the data behavior is in the evaluation of systematic effects. An example of systematic phenomenon is the pile-up in the VTX detector (described in section

2.1.1). Figure 4.3 illustrates the comparison of the distributions of the number of vertices reconstructed with the VTX detector in data and Monte Carlo. When more than 1 vertex is present in the distribution, it means that one or more pile-up occurrences took place. The distribution of the number of
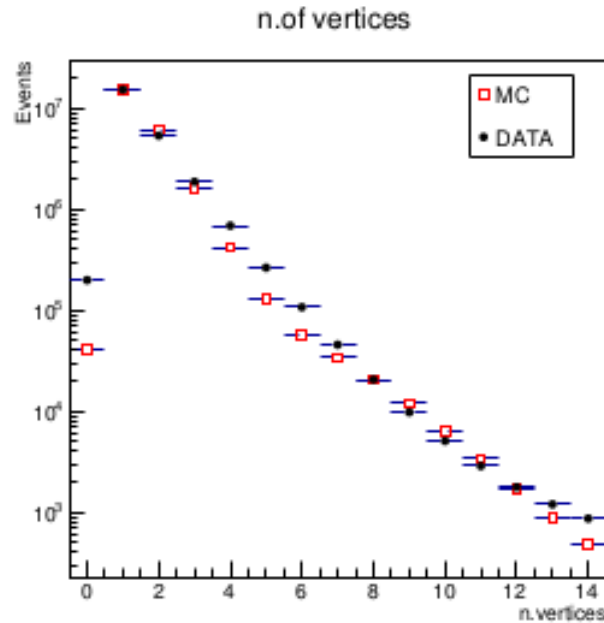
Figure 4.3: Number of reconstructed vertices for DATA and MC. The MC distribution is normalized to the same number of entries of the data.

reconstructed vertices in the VTX detector, obtained starting from the experimental data (black dots in figure 4.3), has been fitted with a Poissonian curve (with mean $\lambda = 0.758$). To well replicate the pile-up phenomenon in the MC code, for each event, a number of additional tracks deriving from events stored in a list is added to the ones of the event under study, according to the Poissonian distribution obtained through data. From figure 4.3, it can be noticed a good matching between the simulated distribution (red squares) and the experimental one. This means that the pile-up phenomenon has been well implemented in the MC code, which is able, therefore, to reproduce this kind of experimental systematics in a satisfactory way.

Chapter 5

The High Level Global Reconstruction

5.1   The Global Reconstruction code in FIRST

The high level global reconstruction algorithm has the aim to determine the momentum and mass of all the charged particles produced in the ^{12}C-^{12}C reactions, that means to completely describe the kinematics of the reaction. On the basis of the fragment production angle, the reconstruction strategy in FIRST follows a different procedure due to the different particle path:

a) if the polar angle θ is less than 5 deg, the fragment enters the AL-ADiN magnet region, where the momentum is computed measuring the bending in the XZ plane, and then is detected by the TW;

b) for large production angles (θ larger than 5 deg), the fragments cannot enter the magnet region and hence are detected by the KENTROS calorimeter.

This algorithm has been implemented using the C++ language and it has been tested on several Linux and MAC-OS platforms.
It is built on a event-tracking basis, performed by matching together the information extracted from each sub-detector. At this level, the local reference frame of each detector is converted to a global one, for a coherent description of the positions.
The reconstruction output files are ROOT ntuples [121] to be treated with suitable programs (macros), written for extracting the cross-section distributions in angle and energy.
The reconstruction code follows three fundamental steps.

1. At first, each event is selected applying many filters:

   a) one event is considered in the algorithm if at least one hit on the ToF-Wall[1] and one track in the Vertex detector are available;

   b) only TW hits in which the charge has been assigned to the fragment can be considered in the code;

   c) only VTX tracks that are in the ALADIN magnet window entrance acceptance are taken into account.

2. For each filtered event, a list of Global Track Candidates (GTC) is obtained, by combining all the VTX tracks with the TW hits: each VTX track is paired with one (or more) TW hit. In this way a TW charge is assigned to each GTC.

3. The track candidates are ranked in a list accordingly to quality criteria of the match VTX-TW. When more than one TW hit is associated to the same VTX track, duplicates appear in the rank list and must be removed. This is done by clustering the hits in the Front and Rear Walls of TW, i.e. associating the two hits of a single fragment detected by the two TW walls, considering them as one single hit. A scoring function is then applied to the purged list, in order to select the best candidates.

The VTX-TW matching quality criteria are based on weight factors coming from measured quantities: the fragment charge and vertical coordinate. Both these quantities, in fact, can be determined by the detectors TW (as described in sections 3.2 and 3.3) and VTX.
The VTX evaluation of the charge is based on the dimensions of the pixel cluster that each fragment produces in the detector planes. In figure 5.1 the results of the charge identification method of VTX are shown. In the "CountsvsA" sub-plots of figure 5.1, it can be seen that the six charges, from Hydrogen to Carbon, are well distinguished according to their mass number A. For charges Z=1 and Z=2 also the different isotopes can be identified: for Z=1, protons, deuterons and tritons can be recognized; instead for charge Z=2, the ^{3}He and ^{4}He isotopes are discerned.
The vertical coordinate can be determined by VTX thanks to the reconstruction procedure itself: the trajectory of each fragment, which gives one of the VTX pre-selected track, is determined using the reconstruction algorithm and the impact point onto the TW detector is found. The vertical coordinate of the impact point is defined as Y_{VTX}.

---

[1] A hit on TW corresponds to a particle revealed by the detector slats.
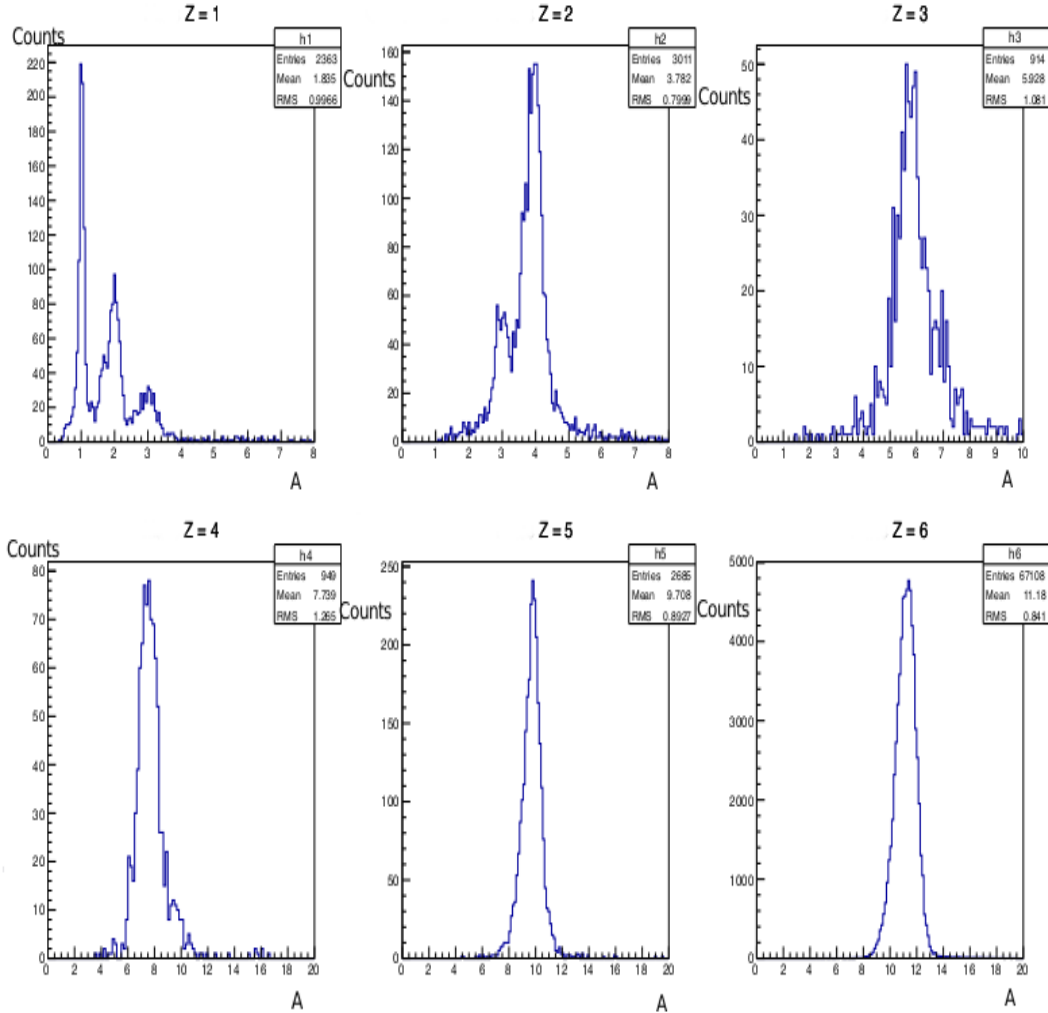
Figure 5.1: The results of the charge identification process performed by VTX are illustrated in this figure. Charges from Z=1 to Z=6 are identified. For charges Z=1 and Z=2 also the different isotopes can be distinguished.

The comparison of the information coming from the two detectors provides a way to evaluate the best matching of the tracks, when more than one track is available from VTX. Starting from the difference between the particle charge as reconstructed from the VTX and from the TW detectors (Δ_{chg}) and the difference between the Y position (Δ_Y) as extrapolated from the VTX and as measured with the TW, the adopted Scoring Function (SF) is defined as:

$$SF = \sqrt{\Delta_{chg}^2 * w_{chg}^2 + \Delta_Y^2 * w_Y^2} \qquad (5.1)$$

w_{chg} and w_Y are weight factors, whose values have been optimized on the MC simulations, by minimizing the fraction of wrongly reconstructed tracks. Running the reconstruction code on MC data, the number of erroneously reconstructed tracks can be evaluated. To minimize the percentage of wrongly reconstructed tracks, the weight factors belonging to the scoring function are varied one with respect to the other, in order to optimize the performance of the reconstruction algorithm. The corresponding best values of the weight factors (w_{chg} and w_Y) are then used also for the reconstruction on experimental data. Figure 5.2 shows the percentage of incorrectly reconstructed tracks for protons as a function of the weight factor related to the charge. Since the value 8 is the lowest one that minimizes the percentage of tracks badly reconstructed, it is chosen as the proper value for w_{chg}.
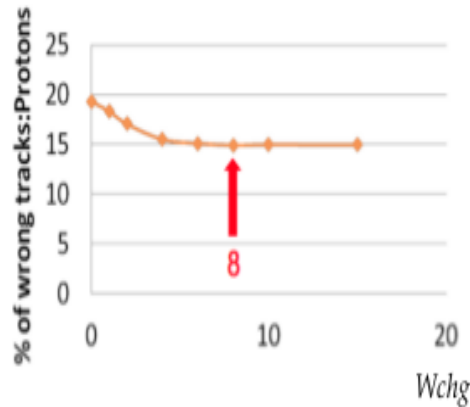
Figure 5.2: An example of optimization of the TW/VTX matching criteria in the reconstruction of protons.

The reconstruction algorithm is developed to compute, for each created GTC, the physical quantities of interest: charge, speed, momentum and mass of the fragments.
The particle charge is directly derived from the energy loss measurements in the ToF-Wall (see section 3.3). The TW is also able to provide the particle Time of Flight that, together with the fragment path reconstructed by the tracking algorithm, gives the fragment speed. The momentum (p) is computed using the charge and measuring the curvature in the magnet region; finally, knowing the particle impulse and speed, also the mass is reconstructed.

To determine at best the curvature inside the magnetic region, it is necessary a precise knowledge of the (non uniform) magnetic field inside and outside the magnet. The knowledge of both the ALADiN geometry and the field map, consisting in a set of values (B_x, B_y, B_z) measured with "Hall probes" in different points of the magnet, for various currents, have been inherited from previous experiments performed at GSI within the ALADiN collaboration [122].

In the following a more detailed description on how the reconstruction algorithm works is given.

Each sub-detector belonging to the FIRST setup registers the particle's passage by recording a hit. All the registered hits are combined to form tracklets and, in the following, global tracks of the event.
At first, the Interaction Region (IR) tracks are obtained using the information coming from the Vertex and the Beam Monitor detectors. The four planes of VTX are used to reconstruct the tracks of the fragments emerging from the target. The passage of a charged particle activates clusters of pixels in the 4 planes of VTX. The tracking algorithm of VTX aims to find straight paths compatible with the centers of one cluster per plane on the basis of a χ^2-minimization procedure. The tracking reconstruction efficiency, evaluated on Monte Carlo simulated events, is 98.7±0.1%, with a measured proportion of fake tracks of 1.99±0.01% [104].
The tracks defined in the VTX planes allow, together with the track information about the impact point of the primary ion on the target coming from the Beam Monitor, to reconstruct the interaction vertex in the target, when a fragmentation process happened. The reconstructed interaction point (vertex) can then serve as additional hit-point for subsequent track reconstruction. In the case in which more than one vertex is found in the VTX detector, the one closest to the BM extrapolated on-target position is taken as the true vertex for the event under study. The other ones are discarded as PU (Pile-Up) vertexes. The angular precision on the reconstructed tracklets, guaranteed by the high resolution of both VTX and BM, is about 0.06 deg (see figure 5.6).
After VTX, the ions can follow two different paths: if their polar angle is larger than 5 deg, they are detected by the KENTROS calorimeter. This detector can provide the impact point of the particles on it. This information allows to perform signal attenuation and timing corrections for KENTROS hits before reconstructing the particle energy and its charge.
When the ion polar angle is smaller than 5 deg, instead, they can enter into the magnetic-field region and are finally detected by the ToF-Wall. In

this case the fragments are reconstructed using an iterative procedure that matches the VTX tracks and the TW hits detected in each event.

The magnetic field of the ALADiN spectrometer is described, in its central part, by a Woods-Saxon formula [123] given by:

$$B(z) = \frac{B_0}{1 + e^{\frac{z-D}{a}}} \tag{5.2}$$

where z is the beam direction, B_0 is the maximum magnetic field in the region (0.8 T), D is the field length (70 cm) and a (about 10 cm) quantifies the slope of the fall-off of the field, the so-called surface thickness.

Since the magnetic field varies along z, when the particles travel inside it, its effect on the trajectories is a deflection in the horizontal plane (x,z), depending on the ion type and energy.

The magnetic rigidity R, needed for tracking in the magnetic field, depends on the particle mass m, charge q and speed v and on the trajectory curvature radius in the magnet ρ, trough the equation:

$$R = B\rho = \frac{p}{q} = \frac{mv}{q} \tag{5.3}$$

where not all the necessary information (m, p) is immediately available. For this reason, for the tracking inside the magnetic field, it is needed a reconstruction code. This exploits the magnetic field maps, available for different magnet currents, to determine the particle path inside ALADiN, taking into account also the magnetic hysteresis.

For each GTC, built pairing a IR tracklet with a hit in the ToF-Wall, the algorithm performs an iterative forward-tracking through the magnetic field, which bends the particle in the horizontal plane. Starting from the positions and angles measured in the IR, with a first-guess value for the momentum, the measured coordinates are forward-tracked inside the ALADiN magnetic field and are projected on the ToF-Wall. The horizontal coordinate of the track projected on TW (X_{VTX}), obtained as a provisional result of the reconstruction, is compared with the one measured by the TW. If the two coordinates differ more than 1.25 cm (corresponding to a semi-slat of the TW), it means that the hypothesized momentum is not correct. Therefore it is changed and the forward-tracking procedure is repeated. This process continues until the reconstructed position of the hit agrees with the measured one (within 1.25 cm). After the convergence, the algorithm returns, for each GTC, the reconstructed momentum p. At this level, the matching criteria, previously described, are used to rank the Global Track Candidate list and to select the best candidate for each event.

In figure 5.3 an example of a fully reconstructed fragmentation event, in which four fragments are produced at small angle, is shown.
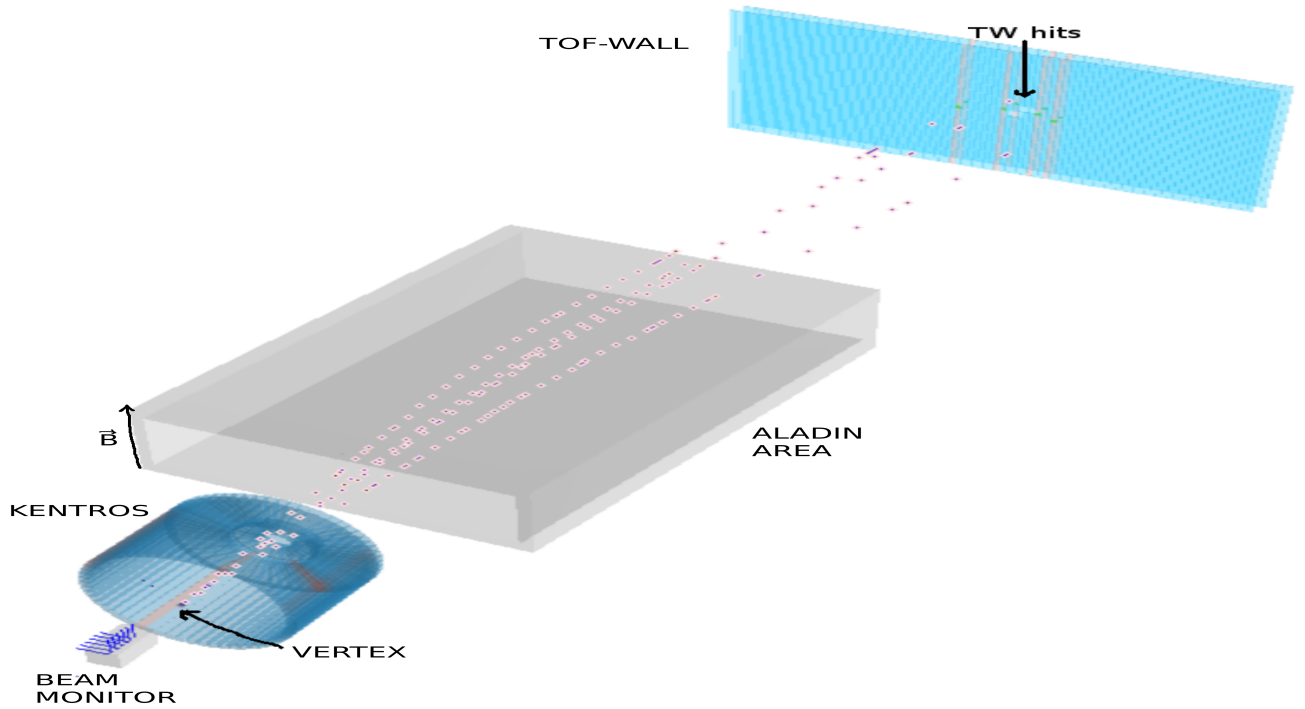
Figure 5.3: 3D view of a fully reconstructed fragmentation event, with 4 fragments produced in the small angle region. The fired BM wires/cells are highlighted in blue, in the bottom left corner of the picture. The KENTROS blue barrel and endcap modules, surrounding the target/VTX region (not visibile in this global view scale) are shown as well. The fragment tracks are represented as "dots" in space, connecting the target origin position and the relative 4 fragment tracks in the VTX, with the 4 pairs of red bands on the TW (2 for each fragment as it traverses both the Front and the Rear Walls) representing the TW slats that have been hit. The TW hits used to build the tracks are shown as tiny spots in green. The track bending happens in the grey box, representing the ALADIN magnet region; before and after that region the magnetic field is supposed to be almost 0 and the track trajectory is assumed to be a straight line.

5.1.1 Mass distributions

The mass of each fragment can be defined as:

$$m = Am_0\gamma = \frac{Am_0}{\sqrt{1-\beta^2}} \tag{5.4}$$

m_0 is the rest mass defined as $m_0 = m_u - \frac{Z}{A} * m_e + \frac{\Delta(A)}{A}$, where $m_u = 0.9315$ GeV/c^2 is the atomic mass unit, m_e is the electron mass and $\Delta(A)$ is the mass excess of the nuclide (A,Z). A good approximation is given by m_0 equal to the proton mass. A is the fragment atomic mass number and $\beta = \frac{v}{c}$, with v corresponding to the fragment speed. By combining equations 5.3 and 5.4, it is possible to derive the atomic mass number A, measured in the spectrometer:

$$A = \frac{0.3 * R * Z * \sqrt{1-\beta^2}}{m_0 * v} \tag{5.5}$$

where the factor 0.3 is due to the conversion between Tm and GeV/c and Z is the fragment charge.

After the reconstruction all the quantities in the right part of the equation 5.5 are known. R is measured through the momentum-reconstruction procedure, the charge and the time of flight are both measured by the ToF-Wall and thus velocity is obtained after the path-length has been reconstructed by the global tracking algorithm.

The relative error on this quantity is related to the time and rigidity resolutions. However, since rigidity R and momentum p are directly proportional (see equation 5.3), it is possible to write the formula of the relative error on A as a function of the momentum resolution:

$$\frac{\Delta A}{A} = \sqrt{(\frac{\Delta p}{p})^2 + \gamma^4(\frac{\Delta t}{t})^2} \tag{5.6}$$

$((\frac{\Delta p}{p}) = (\frac{\Delta R}{R}))$ has been assumed).

A maximum 10% relative error on the fragment mass is mandatory in order to have a clear separation of all the ions and isotopes under study.

Figure 5.4 illustrates preliminary mass spectra obtained for the different detected charged fragments.

As can be seen in the figure 5.4, the hydrogen (p, d, t) and helium (^{3}He, ^{4}He) isotopes are fairly well resolved in the mass spectra, while for the lithium (^{6}Li, ^{7}Li), beryllium (^{7}Be, ^{9}Be) and boron (^{10}B, ^{11}B) ones the resolution significantly worsens. This is due to the spatial granularity in the bending plane of the TW (2.5 cm wide slat), which produces the increase of the mass resolution as a function of the fragment charge. The resolution in mass varies
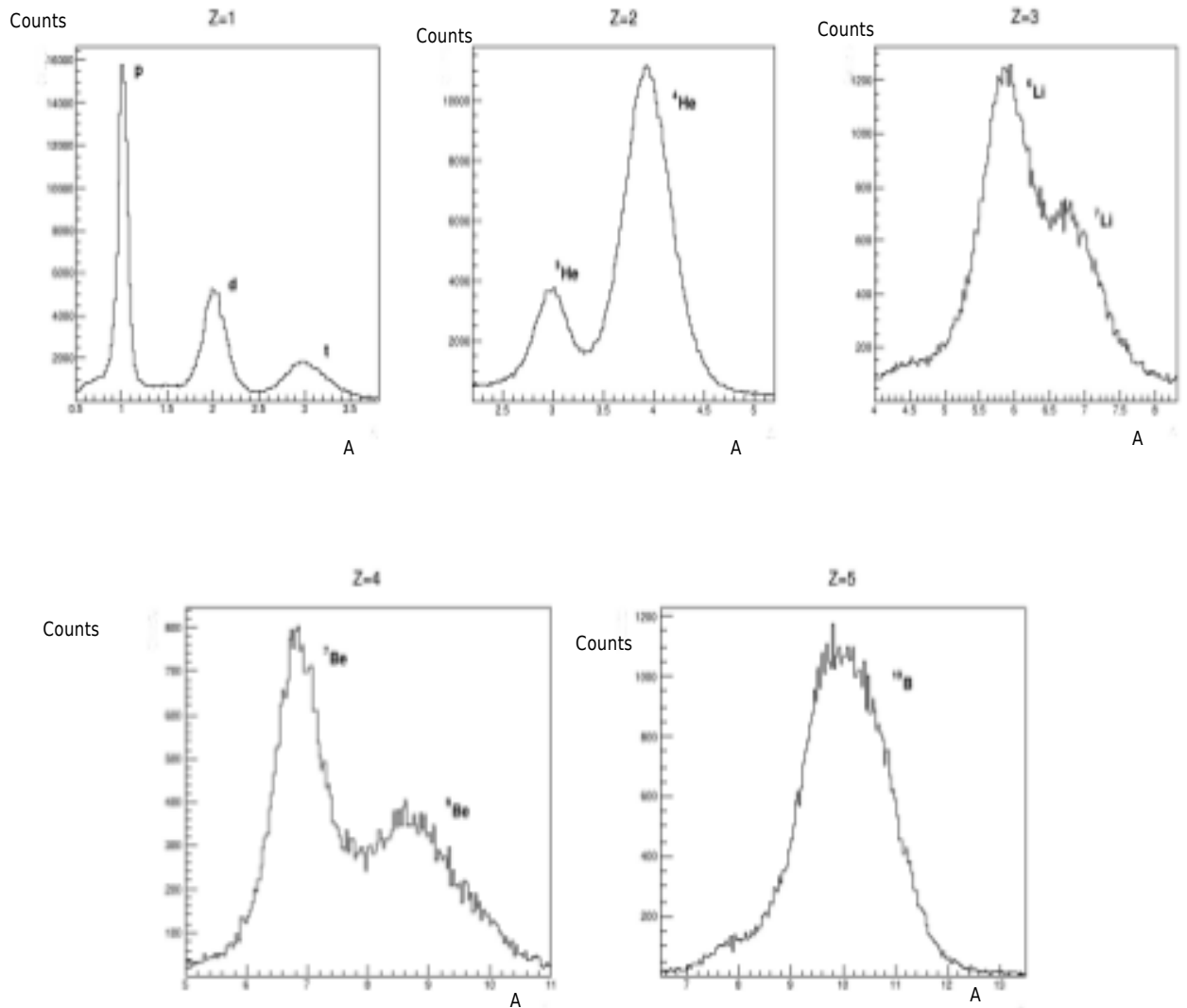
Figure 5.4: Reconstructed mass distributions of the detected fragments.

from 0.05–0.2 MeV for protons to 0.3–0.5 MeV for carbons. Background events are related to charges non correctly identified by the reconstruction algorithm (see section 5.1.3).

The principal cause of the mass uncertainty is the mass-dependent error of the time measurement, which is amplified by the relativistic Lorentz factor γ^2 (= 2 for ions at 400 MeV/n).

5.1.2   Algorithm performances

The global reconstruction algorithm has been validated through a comparison with the MC simulations. Improvements are still ongoing.

In particular, the two important quantities used to build the Single Differential Cross Sections (SDCS), which are the fragment normalized kinetic energy (E_{kin}/n, i.e the fragment kinetic energy over the atomic number) and their production angle with respect to the beam axis (θ), were reconstructed and their resolutions were measured to estimate possible bias due to the reconstruction process.

In addition, an evaluation of the tracking efficiency and the background was made on the full MC simulation sample. The discrepancies between the simulated and the reconstructed events have been considered when evaluating systematic uncertainties.

Kinetic energy and angular resolutions

Both the angular and the kinetic energy resolutions have been measured starting from a MC sample of 24 million events and applying the reconstruction algorithm on those events, in order to have the possibility of comparing the results of the tracking code with the MC simulated events.

For what concerns the kinetic energy resolution (σ_{Ek}), its distribution is composed by two main contributions: the events in which the tracks are built using the correct combinations of VTX tracks and TW hits and those in which a wrong pair of VTX segments and TW hits is used. Both the contributions have been estimated: from the first, the reconstruction efficiency and resolutions can be evaluated; the second instead, is a combinatorial background to be subtracted on statistical bases from the sample of reconstructed tracks.

Figure 5.5 represents the resolution $\sigma_{Ek} \equiv E_k^{MC} - E_k^{rec}$, as a function of the kinetic energy per nucleon E_k/n (normalized energy), for tracks with a proper matching between VTX tracks and TW hits. The resolution increases for higher values of E_k/n because of the reduced bending of the trajectory by the magnetic field and the limited spatial resolution of the TW detector.

In figure 5.6, instead, the angular resolution $\sigma_\theta \equiv \theta^{MC} - \theta^{rec}$ is shown, as a function of the azimuthal angle, for the different fragments. It can be seen that it is stable with respect to the track angle.

The angular resolution has been estimated (for all the ion types) through the comparison of the true MC fragment direction with the one reconstructed
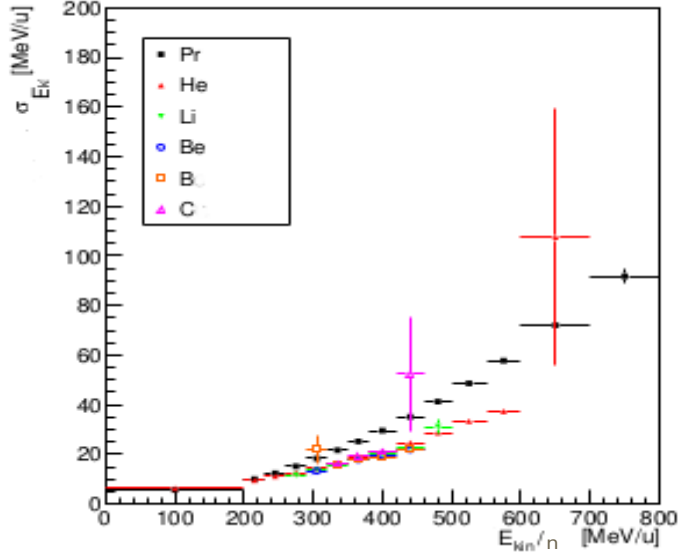
Figure 5.5: Resolution in E_k/n for tracks of different charges: from 1 to 6, with right VTX/TW matches. The size of the total error bar is twice the estimated resolution.

using the FIRST tracking code. For ions from carbon and boron to protons, the mean values obtained for the angular resolutions are in the range 0.054 deg to 0.076 deg, respectively. These numbers are completely dominated by the resolution of the VTX detector.

Tracking efficiency

The tracking efficiency of the algorithm has been estimated with the evaluation of its performances on the full sample of the available MC simulation. All charged fragments emerging from the target region and resulting within the ALADiN geometrical acceptance are considered. n_{Prod} is their number. The reconstruction algorithm has been run on the TW hits and VTX tracks provided at generator level by the simulation, for each fragment. This avoids any source of error not related to the reconstruction algorithm itself (e.g. pile-up, VTX-TW mismatching). The number of properly reconstructed tracks (i.e. when the outcomes of the reconstruction code coincide with the MC data – impulse, mass, charge – associated with a fragment track) is indicated with n_{Rec}.
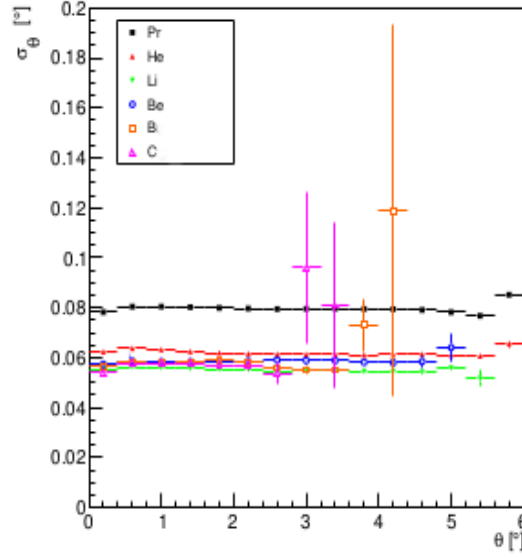
Figure 5.6: Angular resolution as a function of the fragment azimuthal angle. The size of the total error bar is twice the estimated resolution.

Hence the tracking efficiency is defined as:

$$\epsilon_{trk} = \frac{n_{Rec}}{n_{Prod}} \qquad (5.7)$$

Figure 5.7 shows the tracking efficiency as a function of the measured angle θ, for different ions. Similar distributions have been obtained also as a function of the normalized kinetic energy.

Combinatorial background

When, in the VTX track and TW hit matching, hits and tracks are not correctly matched or background hits are paired to VTX tracks, they form random combinations that are considered in the scoring algorithm. Such candidates are defined as "combinatorial background". Two different components can be identified in the combinatorial background mass spectra: combinations of background/noise hits with VTX tracks generate a broad, nearly flat, component; instead, a peaking contribution, with peak position related to the charge assigned by the TW, is due to tracks and hits from real fragments that are wrongly paired by the reconstruction algorithm.
The mass spectrum due to this wrong contribution has to be properly taken into account in the measurement of the fragment production yields (fundamental in the cross section evaluation).
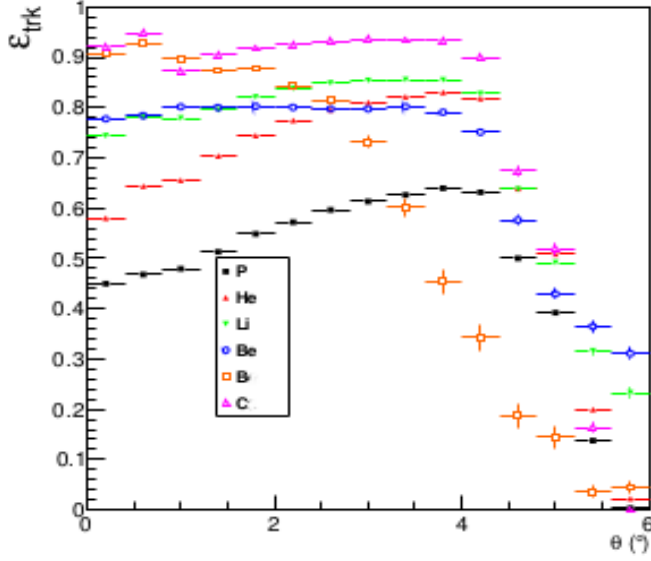
Figure 5.7: Tracking efficiency (ϵ_{trk}) as a function of fragment measured angle, for the different ion types. The uncertainties shown are statistical only. The observed drop around 5 deg is due to the geometrical acceptance of the ALADiN magnet entrance window.

5.1.3 Yield calculation and Cross Feed evaluation

The global reconstruction algorithm developed, allows the identification, for each fragment, of its physical quantities: charge Z, mass number A, impulse p, kinetic energy per nucleon E_k/n, polar and azimuthal emission angles θ and ϕ. Therefore, it is possible to evaluate the yields, i.e. the number of particles with a specific mass available in a definite angular or energy range. The number of reconstructed fragments with charge Z and mass number A in the normalized kinetic energy interval ΔE_i, is defined as $\Upsilon_i^{Z,A}$.

The number of reconstructed fragments with charge Z and mass number A in the polar angle interval $\Delta\theta_j$, instead, is defined as $\chi_j^{Z,A}$.

However, the evaluation of these quantities is contaminated by an effect called "cross feed", that comes from inaccuracies of the charge identification process[2] and of the global reconstruction itself. Both the procedures are affected by errors. Therefore there is the possibility of misidentification of a fragment charge: this is the "cross feed" phenomenon.

The MC simulation has been exploited for the evaluation of the probability of this phenomenon. Simulated events have been fed to the global

---

[2]The charge identification process is described in section 3.3.

reconstruction process to evaluate its performances. Each simulated fragment is generated by the MC with its (Z_{mc}, A_{mc}) pair. When the simulated events are reconstructed through the reconstruction code, each fragment will be provided with a new (Z_{rec}, A_{rec}) couple. Hence the reconstructed pair can be checked versus the MC one; in this way it is possible to understand if a given particle is reconstructed properly. Whenever the (Z_{rec}, A_{rec}) pair coincides with the (Z_{mc}, A_{mc}) couple, the fragment is correctly identified, otherwise not.

Let us introduce the following quantities:

- $g_i^{Z,A}$ is the number of fragments with $(Z_{rec}, A_{rec})=(Z,A)=(Z_{mc}, A_{mc})$ in the energy interval ΔE_i;

- $u_i^{Z,A}$ is the number of fragments with $(Z_{rec}, A_{rec})=(Z,A)\neq(Z_{mc}, A_{mc})$ in the energy interval ΔE_i.

$g_j^{Z,A}$ and $u_j^{Z,A}$ indicate the equivalent quantities for the angular interval $\Delta\theta_j$. Starting from the above quantities, it is possible to evaluate the cross feed correction factor $Xfeed_i^{Z,A}$, for each isotope, in a given energy interval as:

$$Xfeed_i^{Z,A} = \frac{g_i^{Z,A}}{g_i^{Z,A} + u_i^{Z,A}} \quad (5.8)$$

Analogously, the cross feed correction factor $Xfeed_j^{Z,A}$, for each isotope, in a given angular interval is:

$$Xfeed_j^{Z,A} = \frac{g_j^{Z,A}}{g_j^{Z,A} + u_j^{Z,A}} \quad (5.9)$$

Through these corrective factors, the real amount of each isotope, in a given energy or angular interval can be estimated as:

$$Y_i^{Z,A} = Xfeed_i^{Z,A}\Upsilon_i^{Z,A} \quad (5.10)$$

and

$$X_j^{Z,A} = Xfeed_j^{Z,A}\chi_j^{Z,A} \quad (5.11)$$

respectively.

Chapter 6

Cross Section Measurements: preliminary results

The analysis performed on the collected data allowed to determine, for each event, the physical quantities characterizing each fragment: the charge Z, the mass number A, the impulse p together with the polar and azimuthal angles of emission θ and ϕ. This information can be exploited to reckon the following quantities:

- $Y_i^{Z,A}$ that is the number of reconstructed fragments with charge Z and mass number A in the normalized kinetic energy (E_{kin}/n) interval ΔE_i

- $X_j^{Z,A}$, which is the number of reconstructed fragments with charge Z and mass number A in the polar angle interval $\Delta \theta_j$

that are already corrected for the cross-feed phenomenon (as described in section 5.1.3).

These numbers are the experimental quantities necessary to calculate the 2 Single Differential Cross Sections (SDCS) in energy and solid angle, respectively:

$$\frac{d\sigma^{Z,A}}{dE} = \frac{Y_i^{Z,A}}{N_{^{12}C} * N_{t,S} * \Delta E_i * \epsilon_{trk}(E_i)} \tag{6.1}$$

and

$$\frac{d\sigma^{Z,A}}{d\Omega} = \frac{1}{2\pi} \frac{X_j^{Z,A}}{N_{^{12}C} * N_{t,S} * \Delta(cos\theta_j) * \epsilon_{trk}(\theta_j)} \tag{6.2}$$

where:

- $N_{^{12}C}$ is the number of carbon ions impinging on the target. It has been calculated counting the physical unbiased triggers collected with the carbon target: $24*10^6$. This number has been corrected only by the

SC efficiency: $\epsilon_{SC} = (99.7 \pm 0.15)\%$. The Poissonian error given by $\delta N_{^{12}C} = \sqrt{N_{^{12}C}}$ has been considered for the total incident carbon ion number;

- $N_{t,S}$ is the surface nuclear density of the target, calculated as:

$$N_{t,S} = \frac{N_A * \rho}{A} \delta x \qquad (6.3)$$

where N_A is the Avogadro's number, ρ is the target density, measured to be ≈ 4.48 g/cm^3, A is the carbon mass number and δx is the target thickness: (8.00 ± 0.08)mm;

- $\Delta(cos\theta_j)$ is the cosine interval corresponding to the polar angle interval $\Delta\theta_j$: $\Delta(cos\theta_j) = cos(\theta_j - \Delta\theta_j/2) - cos(\theta_j + \Delta\theta_j/2)$.
  Actually, the same angular width $\Delta\theta_j = \Delta\theta$ has been chosen for statistical reasons;

- $\epsilon_{trk}(E)$ and $\epsilon_{trk}(\theta)$ are the tracking reconstruction efficiencies: they have been described in section 5.1.2.

The azimuthal symmetry of the fragmentation process allows to evaluate the double angular differential cross section simply by dividing the data in equation 6.2 by the factor 2π.

The cross sections in equations 6.1 and 6.2 are reported in the tables 6.1 and 6.2 as a function of the normalized kinetic energy and of the polar angle, respectively, per each charge and, within a charge, per the most frequent isotopes.

Concerning the Z=6 fragments, it must be remarked that the tables contain only the so called "fragmentation events", i.e. events for which at least one vertex has been reconstructed in the VTX detector and more than one track is associated to it (these are the fragments detected by the ToF-Wall (TW) when also another signal, created by another charge, was present in the IR detectors). The whole statistic of the ions with Z=6 contains a huge amount of data in which only the signal on the TW was present, without any other particle in the IR. These last events are interpreted as "scattered ^{12}C ions". The Z=6 data including both the "fragmentation events" and the "scattered" ones are reported in tables 6.3 and 6.4, as a function of the normalized kinetic energy and of the polar angle, respectively.

Table 6.1: Normalized kinetic energy differential cross section (b/(MeV/u)). The numbers in brackets represent the total error (both systematic and statistical). For details see section "The cross section errors".

Energy (MeV/u)	^1H $d\sigma/dE(b/(MeV/u))$	^2H $d\sigma/E(b/(MeV/u))$	^3H $d\sigma/E(b/(MeV/u))$	^3He $d\sigma/E(b/(MeV/u))$	^4He $d\sigma/E(b/(MeV/u))$	^6He $d\sigma/E(b/(MeV/u))$
100(100)	1.21e-05 (9.96e-07)	1.64e-05 (1.09e-06)	5.17e-06 (3.73e-07)	1.97e-06 (8.81e-08)	1.40e-06 (5.53e-08)	1.86e-07 (3.93e-08)
215(15)	5.10e-05 (2.65e-06)	3.71e-05 (2.00e-06)	1.62e-05 (1.96e-06)	9.35e-06 (4.41e-07)	7.22e-06 (4.19e-07)	6.20e-07 (1.62e-07)
245(15)	8.09e-05 (3.20e-06)	6.12e-05 (4.37e-06)	3.67e-05 (4.81e-06)	2.02e-05 (9.25e-07)	2.14e-05 (1.15e-06)	1.77e-07 (3.60e-07)
275(15)	1.46e-04 (4.10e-06)	1.16e-04 (8.43e-06)	7.84e-05 (8.55e-06)	4.49e-05 (1.73e-06)	8.17e-05 (4.15e-06)	1.95e-06 (3.26e-07)
305(15)	2.30e-04 (5.67e-06)	1.90e-04 (1.29e-05)	1.46e-04 (1.13e-05)	9.49e-05 (2.82e-06)	3.23e-04 (1.65e-05)	1.95e-06 (1.39e-06)
335(15)	3.00e-04 (6.62e-06)	2.41e-04 (1.25e-05)	1.93e-04 (8.90e-06)	1.49e-04 (2.49e-05)	8.71e-04 (2.76e-05)	5.34e-06 (5.82e-06)
365(15)	3.14e-04 (6.58e-06)	2.30e-04 (1.03e-05)	1.85e-04 (5.06e-06)	1.80e-04 (5.57e-06)	1.21e-03 (3.13e-05)	6.38e-06 (5.13e-06)
400(20)	2.58e-04 (4.73e-06)	1.70e-04 (7.97e-06)	1.28e-04 (3.32e-06)	1.51e-04 (6.03e-06)	8.37e-04 (3.30e-05)	6.33e-06 (2.27e-06)
440(20)	1.72e-04 (6.11e-06)	1.03e-04 (9.23e-06)	7.02e-05 (4.92e-06)	7.57e-05 (1.87e-06)	3.26e-04 (6.41e-06)	1.62e-06 (7.45e-07)
480(20)	1.10e-04 (1.01e-05)	6.35e-05 (1.01e-05)	3.77e-05 (6.32e-06)	3.09e-05 (9.24e-07)	1.04e-04 (9.06e-06)	4.86e-07 (2.83e-07)
525(25)	7.01e-05 (1.14e-05)	3.68e-05 (9.10e-06)	2.36e-05 (6.50e-06)	1.08e-05 (9.02e-07)	3.32e-05 (6.12e-06)	1.68e-07 (4.85e-08)
575(25)	4.37e-05 (1.01e-05)	2.31e-05 (7.10e-06)	1.65e-05 (5.82e-06)	1.10e-05 (3.80e-06)	3.71e-06 (5.39e-06)	2.72e-07 (1.13e-07)
650(50)	5.58e-05 (7.40e-06)	1.59e-05 (5.65e-06)	9.63e-06 (3.67e-06)	1.94e-06 (2.28e-06)	2.57e-07 (2.25e-07)	6.30e-08 (3.78e-08)
750(50)	1.39e-05 (4.54e-06)	9.20e-06 (3.61e-06)	5.67e-06 (2.16e-06)	1.61e-06 (9.96e-07)	1.48e-07 (5.45e-08)	4.03e-08 (2.66e-08)

Energy (MeV/u)	^6Li $d\sigma/E(b/(MeV/u))$	^7Li $d\sigma/E(b/(MeV/u))$	^8Li $d\sigma/E(b/(MeV/u))$	^7Be $d\sigma/E(b/(MeV/u))$	^9Be $d\sigma/E(b/(MeV/u))$	^{10}Be $d\sigma/E(b/(MeV/u))$
100(100)	8.13e-08 (2.31e-08)	8.42e-09 (1.94e-08)	1.17e-08 (5.59e-09)	3.19e-08 (8.43e-09)	1.59e-08 (5.47e-09)	1.59e-08 (5.47e-09)
215(15)	2.16e-07 (5.72e-08)	1.08e-07 (6.84e-08)	8.80e-08 (3.98e-08)	1.14e-07 (4.64e-08)	5.72e-08 (2.88e-08)	5.72e-08 (2.88e-08)
245(15)	9.59e-07 (1.91e-07)	2.69e-07 (1.13e-07)	2.26e-07 (7.95e-08)	2.16e-07 (6.24e-08)	1.08e-07 (3.91e-08)	1.08e-07 (3.91e-08)
275(15)	4.06e-06 (4.66e-07)	6.02e-07 (4.83e-07)	1.12e-06 (4.69e-07)	9.31e-07 (1.35e-07)	3.67e-07 (7.78e-08)	2.13e-12 (3.37e-08)
305(15)	1.86e-05 (1.21e-06)	1.10e-05 (1.07e-06)	1.59e-06 (2.33e-07)	7.05e-06 (6.07e-07)	1.40e-06 (5.12e-07)	1.77e-06 (4.42e-07)
335(15)	5.29e-05 (3.67e-06)	5.62e-05 (3.81e-06)	8.28e-06 (6.66e-07)	3.94e-05 (2.25e-06)	1.11e-05 (2.35e-06)	1.66e-05 (1.12e-06)
365(15)	5.44e-05 (3.11e-06)	1.05e-04 (5.22e-06)	1.24e-05 (5.70e-07)	7.66e-05 (2.62e-06)	3.10e-05 (1.50e-05)	4.75e-05 (1.14e-05)
400(20)	3.72e-05 (2.20e-06)	6.66e-05 (2.88e-06)	8.32e-06 (5.35e-07)	5.39e-05 (2.01e-06)	4.79e-05 (4.93e-06)	4.74e-06 (1.53e-06)
440(20)	1.69e-05 (5.72e-07)	1.99e-05 (1.02e-06)	1.05e-06 (3.00e-07)	1.57e-05 (6.15e-07)	1.44e-05 (7.29e-07)	4.51e-07 (2.96e-07)
480(20)	1.03e-05 (9.72e-07)	3.40e-06 (5.81e-07)	2.66e-07 (1.35e-07)	1.96e-06 (2.51e-06)	1.77e-06 (4.73e-07)	2.12e-16 (1.41e-12)
525(25)	6.91e-07 (9.60e-07)	0.00e+00 (0.00e+00)	0.00e+00 (0.00e+00)	1.34e-06 (1.28e-07)	1.24e-07 (1.05e-07)	5.06e-08 (2.02e-08)
575(25)	1.85e-07 (2.35e-07)	0.00e+00 (0.00e+00)	0.00e+00 (0.00e+00)	2.23e-07 (6.33e-08)	1.11e-07 (4.52e-08)	1.11e-07 (4.74e-08)
650(50)	1.03e-08 (1.17e-08)	0.00e+00 (0.00e+00)	0.00e+00 (0.00e+00)	6.00e-08 (1.50e-08)	3.00e-08 (1.01e-08)	3.00e-08 (1.01e-08)
750(50)	5.14e-09 (5.70e-09)	0.00e+00 (0.00e+00)	0.00e+00 (0.00e+00)	1.96e-08 (9.81e-09)	9.80e-09 (6.25e-09)	9.80e-09 (6.25e-09)

Energy (MeV/u)	^8B $d\sigma/E(b/(MeV/u))$	^{10}B $d\sigma/E(b/(MeV/u))$	^{11}B $d\sigma/E(b/(MeV/u))$	^{10}C $d\sigma/E(b/(MeV/u))$	^{11}C $d\sigma/E(b/(MeV/u))$	^{12}C $d\sigma/E(b/(MeV/u))$
100(100)	1.45e-08 (1.06e-08)	1.45e-08 (1.06e-08)	1.45e-08 (1.06e-08)	2.65e-09 (2.62e-09)	2.65e-09 (2.62e-09)	1.59e-08 (1.19e-08)
215(15)	4.84e-08 (4.40e-08)	4.84e-08 (4.40e-08)	4.84e-08 (4.40e-08)	8.84e-09 (9.52e-09)	8.84e-09 (9.52e-09)	5.30e-08 (3.03e-08)
245(15)	1.11e-07 (7.52e-08)	1.11e-07 (7.52e-08)	1.11e-07 (7.52e-08)	1.50e-08 (1.21e-08)	1.50e-08 (1.21e-08)	9.01e-08 (3.62e-08)
275(15)	3.39e-07 (1.29e-07)	3.39e-07 (1.29e-07)	3.39e-07 (1.29e-07)	3.09e-08 (1.85e-08)	3.09e-08 (1.85e-08)	1.86e-07 (6.39e-08)
305(15)	1.77e-06 (4.30e-07)	7.96e-07 (5.84e-07)	3.84e-06 (1.19e-06)	2.76e-07 (6.87e-08)	1.62e-07 (4.16e-08)	8.10e-08 (1.38e-07)
335(15)	3.21e-06 (3.54e-07)	6.24e-07 (4.61e-07)	3.53e-05 (6.76e-06)	2.58e-06 (3.18e-07)	3.56e-06 (6.67e-07)	1.75e-05 (7.79e-06)
365(15)	8.71e-06 (7.15e-07)	1.34e-05 (4.67e-06)	1.45e-04 (1.96e-05)	1.66e-05 (2.21e-06)	2.33e-06 (9.76e-07)	1.61e-04 (7.15e-05)
400(20)	7.17e-06 (6.38e-07)	8.98e-06 (1.53e-06)	8.71e-05 (6.00e-06)	2.13e-05 (3.72e-06)	8.04e-06 (2.40e-06)	9.53e-05 (4.01e-05)
440(20)	3.23e-06 (3.13e-07)	2.71e-06 (2.72e-06)	5.56e-07 (1.38e-07)	6.25e-06 (1.35e-06)	4.64e-06 (7.10e-07)	1.77e-05 (6.35e-06)
480(20)	1.99e-06 (2.98e-07)	2.47e-05 (6.80e-06)	2.51e-07 (1.02e-07)	1.40e-06 (2.10e-07)	3.89e-06 (1.02e-06)	0.00e+00 (0.00e+00)
525(25)	2.24e-06 (5.34e-07)	3.13e-06 (2.28e-06)	1.06e-07 (6.06e-08)	2.54e-07 (2.59e-07)	0.00e+00 (0.00e+00)	0.00e+00 (0.00e+00)
575(25)	1.87e-07 (1.00e-07)	1.87e-07 (1.00e-07)	1.87e-07 (1.00e-07)	0.00e+00 (0.00e+00)	0.00e+00 (0.00e+00)	0.00e+00 (0.00e+00)
650(50)	5.40e-08 (2.49e-08)	5.40e-08 (2.49e-08)	5.40e-08 (2.49e-08)	0.00e+00 (0.00e+00)	0.00e+00 (0.00e+00)	0.00e+00 (0.00e+00)
750(50)	8.31e-09 (9.51e-09)	8.31e-09 (9.51e-09)	8.30e-09 (9.51e-09)	0.00e+00 (0.00e+00)	0.00e+00 (0.00e+00)	0.00e+00 (0.00e+00)

The cross section errors

The cross section values reported in tables 6.1, 6.2, 6.3 and 6.4 are affected by an overall error, which includes both the statistical and the systematic contributions:

$$err_{tot} = \sqrt{err_{stat}^2 + err_{syst}^2} \qquad (6.4)$$

The systematic error is dominant everywhere. It ranges from 70% to 85% of the total.

The sources of the systematic contribution of the error are numerous; they can be divided in two main categories:

1. errors due to the tracking algorithm, deriving from: criteria for the selection of data, particle identification process and cross feed reliability

Table 6.2: Angular differential cross section (b/sr). The numbers in brackets represent the total error (both systematic and statistical). For details see section "The cross section errors".

θ (deg)	^1H $d\sigma/d\Omega(b/sr)$	^2H $d\sigma/d\Omega(b/sr)$	^3H $d\sigma/d\Omega(b/sr)$	^3He $d\sigma/d\Omega(b/sr)$	^4He $d\sigma/d\Omega(b/sr)$	^6He $d\sigma/d\Omega(b/sr)$
0.2(0.2)	3.8 (3.1)	7.2 (1.8)	2.65 (1.325)	1.8 (0.28)	18.9 (4.7)	0.29 (0.23)
0.6(0.2)	3.6 (0.29)	4.4 (1.1)	2.5 (1.235)	1.7 (0.85)	18.2 (3.65)	0.29 (0.23)
1(0.2)	3.5 (0.2)	2.6 (0.655)	2.0 (1.0)	1.8 (0.31)	15.0 (1.1)	0.13 (0.10)
1.4(0.2)	3.2 (0.18)	2.25 (1.2)	1.8 (0.66)	1.8 (0.14)	12.4 (0.72)	0.18 (0.071)
1.8(0.2)	2.9 (0.2)	2.1 (0.26)	1.6 (0.28)	1.7 (0.14)	10.2 (0.58)	0.21 (0.033)
2.2(0.2)	2.4 (0.17)	1.9 (0.18)	1.4 (0.12)	1.5 (0.13)	8.2 (0.47)	0.12 (0.021)
2.6(0.2)	2.1 (0.14)	1.7 (0.14)	1.3 (0.076)	1.4 (0.11)	6.4 (0.37)	0.091 (0.013)
3(0.2)	1.8 (0.13)	1.5 (0.1)	0.97 (0.073)	1.2 (0.086)	5.1 (0.29)	0.051 (0.0081)
3.4(0.2)	1.6 (0.13)	1.3 (0.083)	0.77 (0.067)	1.1 (0.076)	3.75 (0.22)	0.018 (0.0052)
3.8(0.2)	1.5 (0.12)	1.1 (0.075)	0.69 (0.063)	0.95 (0.064)	2.9 (0.17)	0.011 (0.0033)
4.2(0.2)	1.4 (0.11)	1 (0.072)	0.61 (0.07)	0.78 (0.053)	2.2 (0.13)	0.014 (0.0026)
4.6(0.2)	1.6 (0.13)	1.1 (0.069)	0.66 (0.066)	0.725 (0.046)	1.95 (0.11)	0.023 (0.0042)
5(0.2)	1.6 (0.16)	1.1 (0.082)	0.665 (0.056)	0.44 (0.03)	1.25 (0.075)	0.017 (0.0038)

θ (deg)	^6Li $d\sigma/d\Omega(b/sr)$	^7Li $d\sigma/d\Omega(b/sr)$	^8Li $d\sigma/d\Omega(b/sr)$	^7Be $d\sigma/d\Omega(b/sr)$	^9Be $d\sigma/d\Omega(b/sr)$	^{10}Be $d\sigma/d\Omega(b/sr)$
0.2(0.2)	0.76 (0.95)	2.1 (0.64)	0.28 (0.084)	1.75 (1.21)	2.3 (1.8)	0.51 (0.43)
0.6(0.2)	2.35 (1.1)	1.4 (0.42)	0.22 (0.066)	1.2 (0.87)	0.77 (0.62)	1.3 (0.455)
1(0.2)	2.05 (0.42)	1.3 (0.46)	0.17 (0.086)	1.2 (0.27)	0.61 (0.34)	0.94 (0.18)
1.4(0.2)	1.7 (0.26)	0.96 (0.17)	0.16 (0.029)	1 (0.098)	0.54 (0.16)	0.47 (0.12)
1.8(0.2)	1.3 (0.099)	0.66 (0.047)	0.15 (0.056)	0.78 (0.055)	0.33 (0.077)	0.27 (0.047)
2.2(0.2)	0.985 (0.085)	0.39 (0.034)	0.13 (0.025)	0.59 (0.043)	0.28 (0.02)	0.061 (0.019)
2.6(0.2)	0.62 (0.058)	0.30 (0.037)	0.054 (0.0053)	0.41 (0.025)	0.14 (0.051)	0.069 (0.028)
3(0.2)	0.47 (0.053)	0.25 (0.025)	0.0089 (0.00765)	0.27 (0.019)	0.065 (0.014)	0.047 (0.012)
3.4(0.2)	0.26 (0.032)	0.20 (0.029)	0.00001 (0.000011)	0.17 (0.011)	0.05 (0.0081)	0.0033 (0.0016)
3.8(0.2)	0.12 (0.032)	0.19 (0.026)	0.0009 (0.011)	0.12 (0.01)	0.025 (0.0057)	0.0035 (0.0037)
4.2(0.2)	0.08 (0.0075)	0.0079 (0.011)	0.075 (0.0018)	0.014 (0.0062)	0.0019 (0.0031)	0.0041 (0.0036)
4.6(0.2)	0.072 (0.014)	0.074 (0.013)	0.0012 (0.00095)	0.037 (0.0035)	0.011 (0.0041)	0.0028 (0.0012)
5(0.2)	0.048 (0.0077)	0.036 (0.0052)	0.006 (0.0019)	0.02 (0.0018)	0.0036 (0.0016)	0.0006 (0.00026)

θ (deg)	^8B $d\sigma/d\Omega(b/sr)$	^{10}B $d\sigma/d\Omega(b/sr)$	^{11}B $d\sigma/d\Omega(b/sr)$	^{10}C $d\sigma/d\Omega(b/sr)$	^{11}C $d\sigma/d\Omega(b/sr)$	^{12}C $d\sigma/d\Omega(b/sr)$
0.2(0.2)	0.046 (0.037)	2.2 (1.8)	6.5 (3.255)	4.2 (5.74)	25.1 (3.21)	6.6 (8.1)
0.6(0.2)	0.078 (0.062)	0.62 (0.49)	4.9 (2.465)	2.6 (3.24)	6.9 (8.93)	19.3 (25.1)
1(0.2)	0.1 (0.017)	1.7 (0.55)	2.3 (1.2)	0.35 (0.44)	0.96 (1.25)	4.7 (6.03)
1.4(0.2)	0.12 (0.029)	1.1 (0.27)	1.15 (0.64)	0.1 (0.074)	0.79 (0.52)	0.42 (0.52)
1.8(0.2)	0.076 (0.027)	0.82 (0.37)	0.41 (0.22)	0.061 (0.04)	0.39 (0.055)	0.073 (0.088)
2.2(0.2)	0.04 (0.0091)	0.12 (0.094)	0.49 (0.19)	0.06 (0.023)	0.16 (0.059)	0.026 (0.0265)
2.6(0.2)	0.039 (0.0051)	0.09 (0.074)	0.22 (0.12)	0.038 (0.0065)	0.062 (0.031)	0.0065 (0.0048)
3(0.2)	0.021 (0.0041)	0.16 (0.031)	0.0082 (0.0043)	0.016 (0.0033)	0.03 (0.013)	0.0039 (0.0046)
3.4(0.2)	0.018 (0.0032)	0.057 (0.017)	0.014 (0.0061)	0.0057 (0.0022)	0.0067 (0.0046)	0.00017 (0.00030)
3.8(0.2)	0.0065 (0.003)	0.034 (0.01)	0.0044 (0.0016)	0.0072 (0.0047)	0.0015 (0.00082)	0.0007 (0.00055)
4.2(0.2)	0.0056 (0.003)	0.017 (0.0063)	0.0044 (0.0051)	0.0045 (0.0015)	0.0007 (0.00073)	0.0006 (0.00050)
4.6(0.2)	0.0048 (0.0015)	0.0064 (0.0021)	0.0016 (0.0013)	0.0014 (0.0000434)	0.0008 (0.00054)	0.0002 (0.00012)
5(0.2)	0.0013 (0.00057)	0.0039 (0.00077)	0.0003 (0.00018)	0.0015 (0.0000555)	0.0002 (0.000092)	0.0006 (0.00026)

Table 6.3: Normalized kinetic energy differential cross section (b/(MeV/u)) for Z=6 fragmented (left) and scattered (right) events. The numbers in brackets represent the total error (both systematic and statistical). For details see section "The cross section errors".

Energy (MeV/u)	$^{10}C_{frag}$ $d\sigma/E\left(\frac{b}{MeV/u}\right)$	$^{11}C_{frag}$ $d\sigma/E\left(\frac{b}{MeV/u}\right)$	$^{12}C_{frag}$ $d\sigma/E\left(\frac{b}{MeV/u}\right)$	$^{10}C_{scat}$ $d\sigma/E\left(\frac{b}{MeV/u}\right)$	$^{11}C_{scat}$ $d\sigma/E\left(\frac{b}{MeV/u}\right)$	$^{12}C_{scat}$ $d\sigma/E\left(\frac{b}{MeV/u}\right)$
100(100)	2.65e-9 (2.62e-9)	2.65e-9 (2.62e-9)	1.59e-8 (1.19e-8)	0.0e+0 (0.0e+0)	0.0e+0 (0.0e+0)	0.0e+0 (0.0e+0)
215(15)	8.84e-9 (9.52e-9)	8.84e-9 (9.52e-9)	5.30e-8 (3.03e-8)	0.0e+0 (0.0e+0)	0.0e+0 (0.0e+0)	0.0e+0 (0.0e+0)
245(15)	1.50e-8 (1.21e-8)	1.50e-8 (1.21e-8)	9.01e-8 (3.62e-8)	0.0e+0 (0.0e+0)	0.0e+0 (0.0e+0)	0.0e+0 (0.0e+0)
275(15)	3.09e-8 (1.85e-8)	3.09e-8 (1.85e-8)	1.86e-7 (6.39e-8)	0.0e+0 (0.0e+0)	0.0e+0 (0.0e+0)	0.0e+0 (0.0e+0)
305(15)	2.76e-7 (6.87e-8)	1.62e-7 (4.16e-8)	8.10e-8 (1.38e-7)	0.0e+0 (0.0e+0)	0.0e+0 (0.0e+0)	1.01e-4 (7.93e-6)
335(15)	2.58e-6 (3.18e-7)	3.56e-6 (6.67e-7)	1.75e-5 (7.79e-6)	0.0e+0 (0.0e+0)	0.0e+0 (0.0e+0)	6.36e-3 (2.14e-4)
365(15)	1.66e-6 (2.21e-6)	2.33e-6 (9.76e-7)	1.61e-4 (7.15e-5)	5.67e-5 (3.18e-5)	0.0e+0 (0.0e+0)	5.51e-2 (2.25e-3)
400(20)	2.13e-6 (3.72e-6)	8.04e-6 (2.40e-6)	9.53e-5 (4.01e-5)	1.41e-4 (6.91e-5)	9.33e-4 (4.20e-4)	4.08e-2 (2.38e-3)
440(20)	6.25e-6 (1.35e-6)	4.64e-6 (7.10e-7)	1.77e-5 (6.35e-6)	8.78e-5 (3.25e-5)	9.97e-6 (1.40e-5)	0.0e+0 (0.0e+0)
480(20)	1.40e-6 (2.10e-7)	3.89e-6 (1.02e-6)	0.0e+0 (0.0e+0)	1.67e-5 (1.77e-5)	1.85e-5 (1.55e-5)	0.0e+0 (0.0e+0)
525(25)	2.54e-7 (2.59e-7)	0.0e+0 (0.0e+0)	0.0e+0 (0.0e+0)	0.0e+0 (0.0e+0)	0.0e+0 (0.0e+0)	0.0e+0 (0.0e+0)
575(25)	0.0e+0 (0.0e+0)	0.0e+0 (0.0e+0)	0.0e+0 (0.0e+0)	0.0e+0 (0.0e+0)	0.0e+0 (0.0e+0)	0.0e+0 (0.0e+0)
650(50)	0.0e+0 (0.0e+0)	0.0e+0 (0.0e+0)	0.0e+0 (0.0e+0)	0.0e+0 (0.0e+0)	0.0e+0 (0.0e+0)	0.0e+0 (0.0e+0)
750(50)	0.0e+0 (0.0e+0)	0.0e+0 (0.0e+0)	0.0e+0 (0.0e+0)	0.0e+0 (0.0e+0)	0.0e+0 (0.0e+0)	0.0e+0 (0.0e+0)

Table 6.4: Angular differential cross section (b/sr) for Z=6 fragmented (left) and scattered (right) events. The numbers in brackets represent the total error (both systematic and statistical). For details see section "The cross section errors".

θ (deg)	$^{10}C_{frag}$ $d\sigma/d\Omega(bsr^{-}1)$	$^{11}C_{frag}$ $d\sigma/d\Omega(bsr^{-}1)$	$^{12}C_{frag}$ $d\sigma/d\Omega(bsr^{-}1)$	$^{10}C_{scat}$ $d\sigma/d\Omega(bsr^{-}1)$	$^{11}C_{scat}$ $d\sigma/d\Omega(bsr^{-}1)$	$^{12}C_{scat}$ $d\sigma/d\Omega(bsr^{-}1)$
0.2(0.2)	4.2 (5.74)	25.1 (3.21)	6.6 (8.1)	0.00e+00 (0.00e+00)	0.00e+00 (0.00e+00)	0.00e+00 (0.00e+00)
0.6(0.2)	2.6 (3.24)	6.9 (8.93)	19.3 (25.1)	77.5 (27.1)	1395 (84)	3189 (170)
1 (0.2)	0.35 (0.44)	0.96 (1.25)	4.7 (6.03)	7.49 (1.6)	51.6 (15.0)	542 (37)
1.4(0.2)	0.1 (0.074)	0.79 (0.52)	0.42 (0.52)	0.71 (0.18)	2.84 (0.29)	43.7 (2.5)
1.8(0.2)	0.061 (0.04)	0.39 (0.055)	0.073 (0.0883)	0.089 (0.24)	3.62 (1.2)	1.46 (0.60)
2.2(0.2)	0.06 (0.023)	0.16 (0.059)	0.026 (0.0265)	0.195(0.021)	0.66 (0.068)	0.64 (0.062)
2.6(0.2)	0.038 (0.0065)	0.062 (0.031)	0.0065 (0.0048)	0.10 (0.012)	0.33 (0.026)	0.04 (0.013)
3 (0.2)	0.016 (0.0033)	0.03 (0.013)	0.0039 (0.0046)	0.028 (0.0038)	0.13 (0.01)	0.0056 (0.0044)
3.4(0.2)	0.0057 (0.0022)	0.0067 (0.0046)	0.00017 (0.00030)	0.011 (0.0057)	0.055 (0.014)	0.0008 (0.00050)
3.8(0.2)	0.0072 (0.0047)	0.0015 (0.00082)	0.0007 (0.00055)	0.021 (0.0049)	0.019 (0.0061)	0.0024 (0.0017)
4.2(0.2)	0.0045 (0.0015)	0.0007 (0.00073)	0.0006 (0.00050)	0.0059 (0.0023)	0.012 (0.0044)	0.0052 (0.0024)
4.6(0.2)	0.0014 (0.0000434)	0.0008 (0.00054)	0.0002 (0.0001)	0.0037 (0.0011)	0.0054 (0.00086)	0.0005 (0.00021)
5 (0.2)	0.0015 (0.0000555)	0.0002 (0.000092)	0.0006 (0.00026)	0.003 (0.00055)	0.0022 (0.00081)	0.0003 (0.00020)

evaluation, second level trigger in matching the information from the different sub-detectors (mainly BM and VTX);

2. errors due to the detector sizes and alignments: they can be due to uncertainties in the measurements of the detector positioning or in the evaluation of the positions of the magnetic field maps inside ALADiN.

6.0.4 Discussion on the achieved results

For the discussion of the results, the values in the previous tables (6.1, 6.2, 6.3, 6.4) have been summarized in several plots.

The charge distribution

The total forward cross section $\sigma^Z(\theta \leq 5deg)$ for the production of fragments with the same charge Z, in the angular range $(0 \leq \theta \leq 5$ deg) can be obtained from table 6.2 by summing up the contributions of all the isotopes and integrating in the θ range as:

$$\sigma^Z(\theta \leq 5deg) \equiv 2\pi \int_{cos(\theta=5deg)}^{0} \sum_A \frac{d\sigma^{Z,A}}{d\Omega} d(cos\theta) =$$

$$= 2\pi \sum_A \sum_j [\frac{X_j^{Z,A}}{N_{^{12}C} * N_{t,S} * \Delta(cos\theta_j) * \epsilon_{trk}(\theta_j)}]\Delta(cos\theta_j) \qquad (6.5)$$

These total forward cross sections are plotted in figure 6.1 as a function of the charge Z: it is clearly visible that the forward direction $(0 \leq \theta \leq 5$ deg) is mostly populated by low charge fragments (Z=1,2). In other words, the

fragmentation process emits forward protons, deuterons, tritons, ^{3}He and α particles nearly one order of magnitude more than isotopes of Li, Be, B and C.
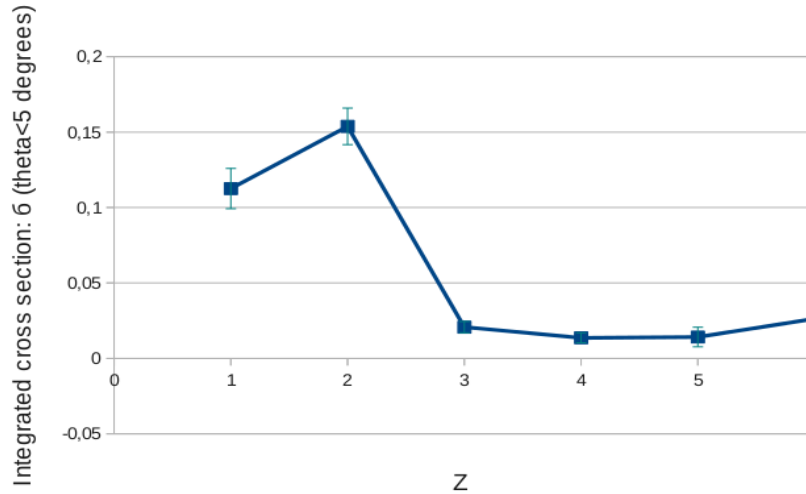

Figure 6.1: The integrated cross sections as a function of Z. The error bars take into account both the systematic and the statistic errors. For details see section "The cross section errors".

The contribution of each single isotope of the charges Z=1,2,3,4,5 can be seen in figure 6.2, where the Single Differential Cross Sections $\frac{d\sigma^{Z,A}}{d\Omega}$ are plotted as a function of the polar angle.

It is interesting to observe that for each Z the most frequent isotopes are the ones with the highest natural abundance or the lowest binding energy.
Let us look in a little bit more detailed way the cases Z=1 and Z=2.
The ratio of deuteron to proton abundance shows (figure 6.2, panel a) an enhancement at very low angles, while it remains nearly constant, around 60-70%, at higher angles. The tritium abundance is lower than protons and deuterons in the whole angular range.
The abundance of the isotopes of charge Z=2 is reported in figure 6.2, panel b and shows a strong dominance of the α particles with respect to ^{3}He and ^{6}He. This is related to the property of the α particles to be a strongly bound system.
For what concerns Z=3, the lithium fragments, reported in figure 6.2, panel c, are mainly the naturally abundant A=6 and A=7. Nevertheless, their ratio is in favor of A=6 (contrary to the abundance in nature) with the exception of the minimum angle $\theta = 0.2$ degrees. However, it must be remarked that,
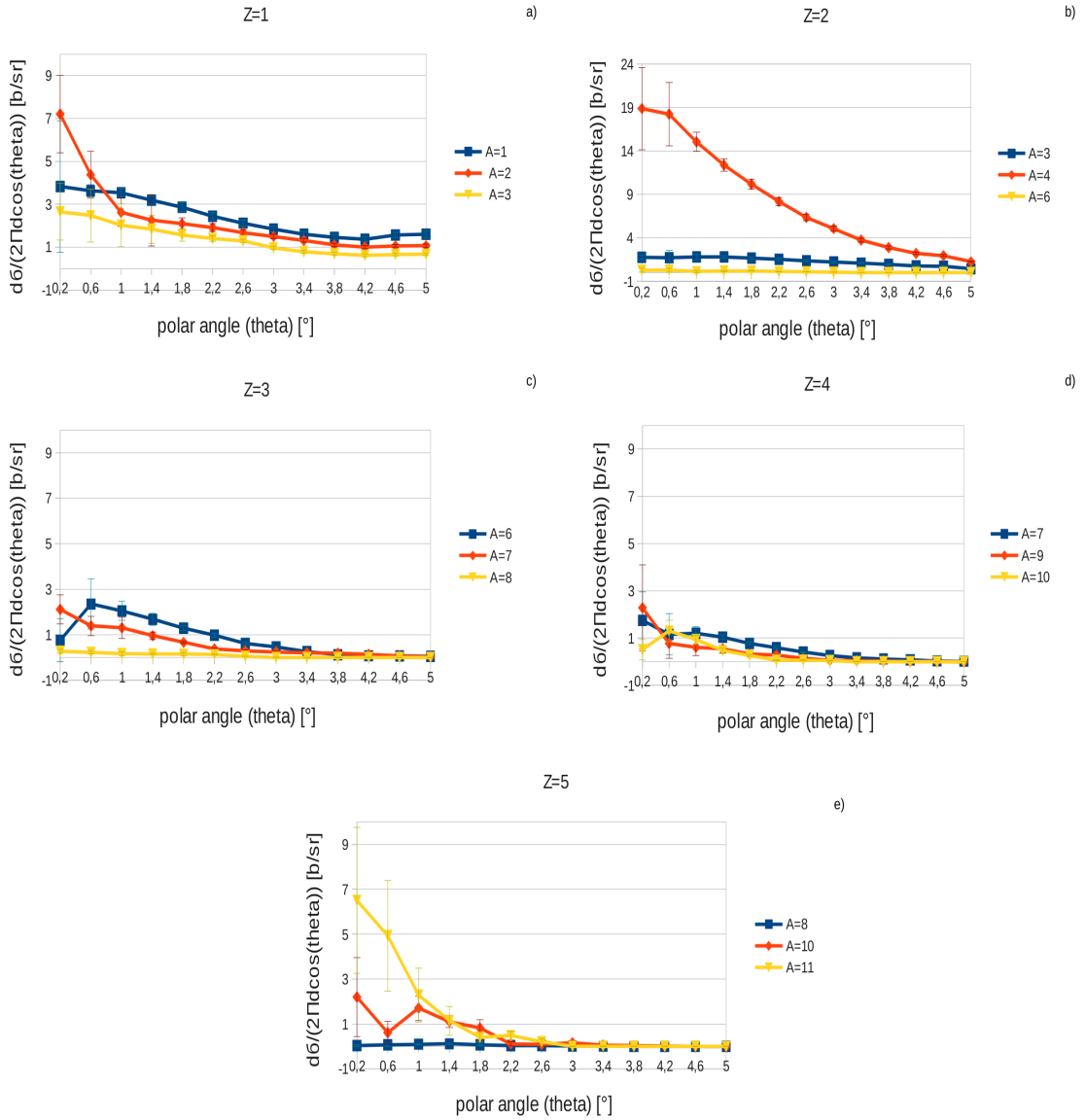
Figure 6.2: Single Differential Cross Sections $\frac{d\sigma^{Z,A}}{d\Omega}$ as a function of the polar angle. From left to right and from top to bottom: Z=1 isotopes (panel a); Z=2 isotopes (panel b); Z=3 isotopes (panel c); Z=4 isotopes (panel d); Z=5 isotopes (panel e). The range on the vertical axis is common for all the panels with the exception of panel b, where the values are larger requiring a different scale. The error bars take into account both the systematic and the statistic errors. For details see section "The cross section errors".

especially at low angles, the error bars are very large. The presence of the ^{8}Li isotope, moreover, is significantly lower than the one of the other two isotopes.

The isotopes of the charge Z=4 (Be), reported in figure 6.2, panel d, are affected by quite large errors at low angles. The lightest isotope, A=7, seems to be the most produced in the fragmentation. The other two, instead, equally contribute.

In the distributions of the Z=5 fragments (figure 6.2, panel e), the dominance of the most naturally abundant isotope, A=11, is evident over the A=10 (second abundant) and A=8 (unstable) isotopes.

A common feature of the angular distributions of all the isotopes is the emission at very low angles. In fact, it can be observed in the figure 6.2 that for angles larger than 1.5 degrees, the cross section is lower at least of an order of magnitude that in the very forward direction.

A more detailed look inside the forward angular range ($0 \leq \theta \leq 5$ deg) can be given in figure 6.3, where the angular double differential cross sections, summed over the isotopes,

$$\frac{d\sigma^Z}{d\Omega} \equiv \sum_A \frac{d\sigma^{Z,A}}{d\Omega} \tag{6.6}$$

are plotted as a function of the polar angle θ for each Z. The Z=6 sample contains the "fragmentation events" only. It is quite evident that the heaviest fragments (Z=3,4,5,6) are more forwardly focused (nearly within 2 degrees) than H and He. From the point of view of the energy loss (relevant to the hadrontherapy) the heavier fragments release energy close to the trajectory of the primary beam. Moreover, their smaller angular range suggests to expect them to be absent at large angle. Such a hypothesis will be confirmed or declined by further analyses including the data from the IR detectors (expecially KENTROS).

Other interesting features of the forward fragmentation can be observed looking at the differential cross sections:

$$\frac{d\sigma^Z}{dE} \equiv \sum_A \frac{d\sigma^{Z,A}}{dE} \tag{6.7}$$

of each Z, reported in figure 6.4 as a function of the normalized energy.

The distributions of all the charges are bell-shaped in semilogarithmic scale, their widths, at the contrary, are wider for the lighter fragments (H,
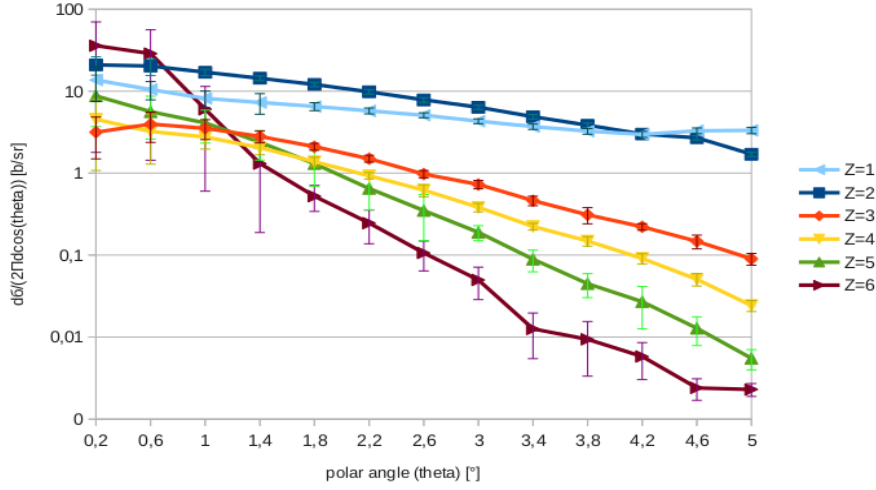
Figure 6.3: Angular Single Differential Cross Sections $\frac{d\sigma^Z}{d\Omega}$ as a function of the polar angle, for the H, He, Li, Be, B, C ions. The error bars take into account both the systematic and the statistic errors. For details see section "The cross section errors".
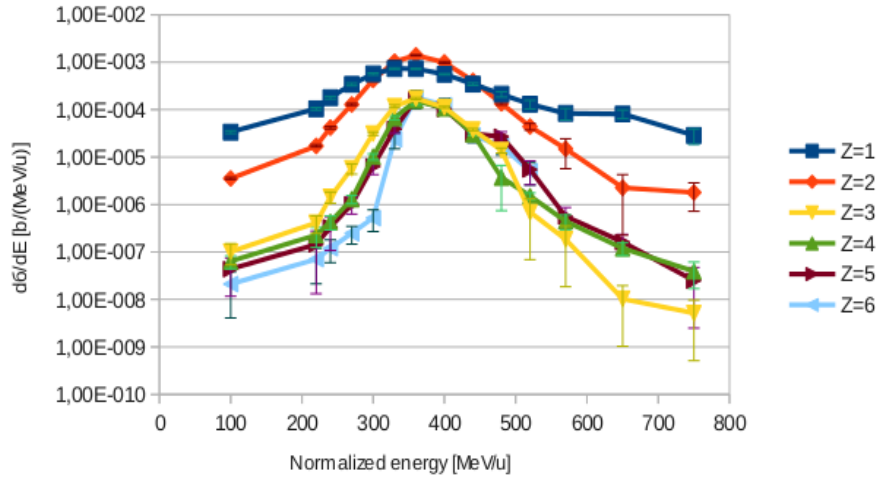

Figure 6.4: Energy Single Differential Cross Sections $\frac{d\sigma^Z}{dE}$ as a function of the normalized kinetic energy, for the H, He, Li, Be, B, C ions. The error bars take into account both the systematic and the statistic errors. For details see section "The cross section errors".

He). Therefore the peculiarity of such fragments with respect to the other

ones is confirmed also from the point of view of the energy. Another striking feature is the position of the peak of the distributions, close to about 360 MeV/n. This value, slightly lower than the one of the primary beam (400 MeV/n), is common to all the charges. Since the highest charges (Z=3,4,5,6) are narrower distributed, it is possible to deduce that such fragments are mostly residuals of the ^{12}C projectiles, which almost conserve the normalized energy (and impulse). On the other side, H and He isotopes seem to cover a larger range of energy and look like real fragments, spread out in the projectile-target interaction.

Let us examine the energy distributions of the isotopes for each charge.

The Z=1 isotopes are reported in figure 6.5, panel a. As a first remark, the errors are smaller than few percent approximately, in the whole energetic range. The 3 distributions are similar in shape and clearly show that the contents of hydrogen, deuterium and tritium are progressively decreasing with increasing A, as in the natural abundance. The distributions of the 3 isotopes have a maximum around 350 MeV/n and a FWHM around 170 MeV/n.

Figure 6.5, panel b, shows the isotopes of charge Z=2. The errors are of the same order of magnitude of the Z=1 distributions. It can be noticed that the α particles are strongly dominant (as seen also in the angular distribution) and their distribution has a FWHM of about 120 MeV/n and is centered at 360 MeV/n.

The isotopes of charge Z=3 (shown in figure 6.5, panel c) also present small errors (few percent). The most naturally abundant isotope, A=7, is dominant with respect to the other two: A=6 and A=8. The distributions are peaked at 360 MeV/n and their FWHM is around 100 MeV/n.

The isotopes of Berillium are shown in figure 6.5, panel d: in this case only A=7 is measured with errors of the order of few percent. Unfortunately the most common isotopes in nature, A=9 and A=10, show quite large error bars ($\approx 50\%$) in the central part of the distributions. The experimental data show that the most abundant isotope is ^{7}Be; the other two, on the other hand, equally contribute. The ^{7}Be distribution is peaked at 360 MeV/n as ^{10}Be and has a FWHM of about 100 MeV/n as the Li isotopes. The FWHM for ^{10}Be is smaller: it is around 70 MeV/n. The ^{9}Be instead is centered at 400 MeV/n: however it must be considered that the error in the kinetic energy is 40 MeV/n (for the 400 MeV/n bin), therefore this energy value of the peak can be still compatible with the one of the other two isotopes. The FWHM is approximately 100 MeV/n.

For what concern the isotopes of charge Z=5, in figure 6.5, panel e, it can be noticed that ^{11}B is largely dominant with a distribution centered at 360 MeV/n and FWHM around 80 MeV/n. The presence of ^{8}B is practically

negligible, while ^{10}B has a distribution with the peak shifted of about 90 MeV/n with respect to the maximum peak (of ^{11}B). Since the error bars are small, this feature can be considered reliable and needs more careful investigations.

The case of the Carbon fragments

A particular attention must be dedicated to the data containing C fragments. As said in the previous paragraph, two kinds of Z=6 fragments have been observed in the experiment: the Carbon "fragmentation events", whose observation was always accompanied by the presence of other particles in the IR detectors and the so called "scattered isotopes", for which other particles were absent.
In figures 6.6 and 6.7, the differential cross sections $\frac{d\sigma^{Z=6}}{d\Omega}(\theta)$ and $\frac{d\sigma^{Z=6}}{dE}(E)$ are reported as a function of the polar angle and of the normalized kinetic energy, for the fragmented (panel a) and the scattered (panel b) C events.

The error bars in energy are around 12%, while in angle the errors are around 0.2 degrees.

By comparing the two panels in figures 6.6 and 6.7, it is possible to notice that the population of the C fragmentation events is much lower (about 3 order of magnitudes for the cross sections both as a function of the polar angle and of the kinetic energy) than the scattered C ions. Such a low percentage lies within the errors of the IR detector efficiencies, therefore the C fragmented events have a high probability to be spurious signals. The very large error bars reported in figure 6.6, panel a, confirm such a hypothesis. Hence, for the moment, it is possible to neglect the C fragmented events.
Looking at figure 6.6, panel b, three different isotopes can be seen: the ^{12}C nuclide, which is identical to the primary beam ions and ^{11}C and ^{10}C, which have 1 and 2 neutrons less. Of course, the ^{12}C nuclides did not undergo any fragmentation process. The only difference with respect to the primary beam is their spread in direction. In fact, the aperture of the primary beam is 0.25±0.2 degrees. The angular distribution in figure 6.6, panel b instead, starts from $\theta = 0.6 \pm 0.2$ degrees. Of course, a contribution deriving from the tails of the ^{12}C ions of the primary beam can not be excluded in the first angular bin of figure 6.6, panel b. Nevertheless, the contents of the following two bins (0.8–1.6 degrees) are much higher than the ones of all the lower charge fragments (in the corresponding angular bins). Therefore these ^{12}C isotopes do not belong to the primary beam and are not accompanied by any particle in the IR detectors. The only process they could undergo is the scattering.
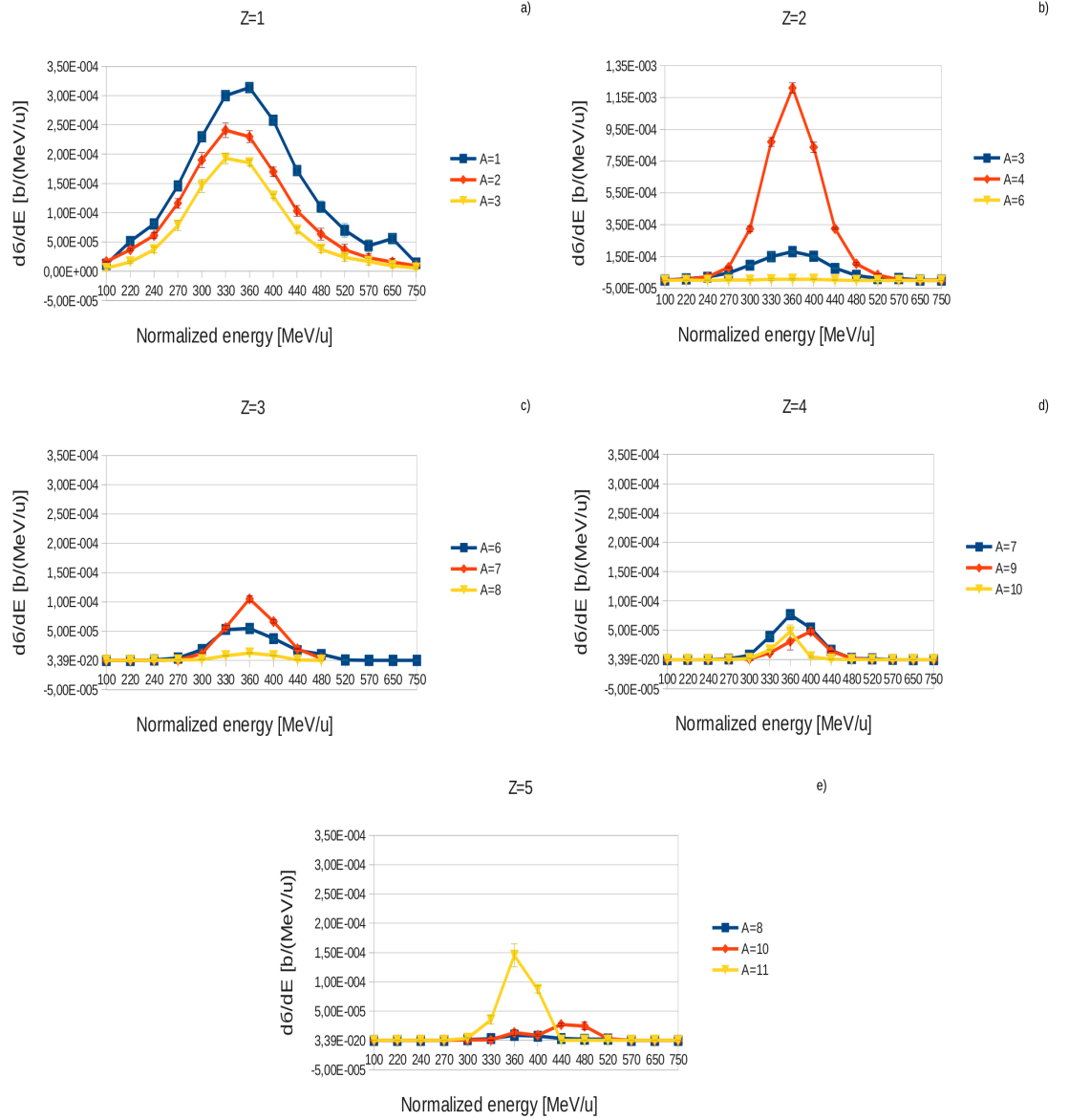Also figure 6.7, panel b shows a spread in energy larger than the one of the

Figure 6.5: Single Differential Cross Sections $\frac{d\sigma^{Z,A}}{dE}$ as a function of the polar angle. From left to right and from top to bottom: Z=1 isotopes (panel a); Z=2 isotopes (panel b); Z=3 isotopes (panel c); Z=4 isotopes (panel d); Z=5 isotopes (panel e). The range on the vertical axis is common for all the panels with the exception of panel b, where the values are larger requiring a different interval. The error bars take into account both the systematic and the statistic errors. For details see section "The cross section errors".
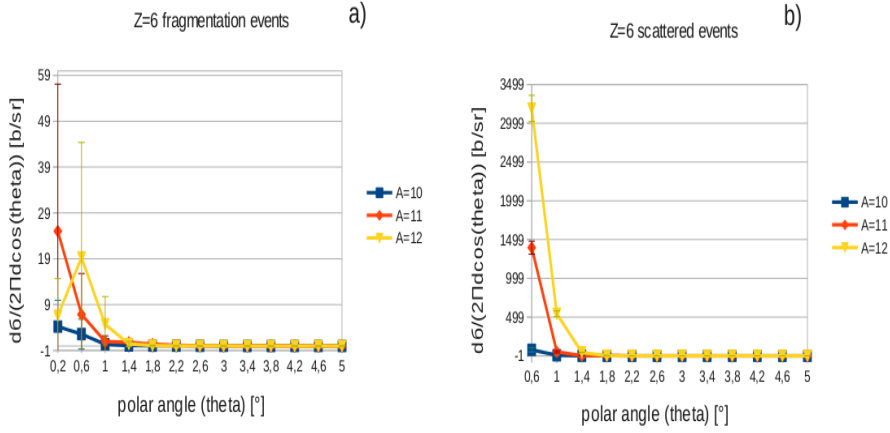
Figure 6.6: Single Differential Cross Sections $\frac{d\sigma^{Z=6}}{d\Omega}(\theta)$ as a function of the polar angle, for the Z=6 isotopes: A=10,11,12. Panel a shows the case of fragmented events, panel b the one of scattered events. The error bars take into account both the systematic and the statistic errors. For details see section "The cross section errors".
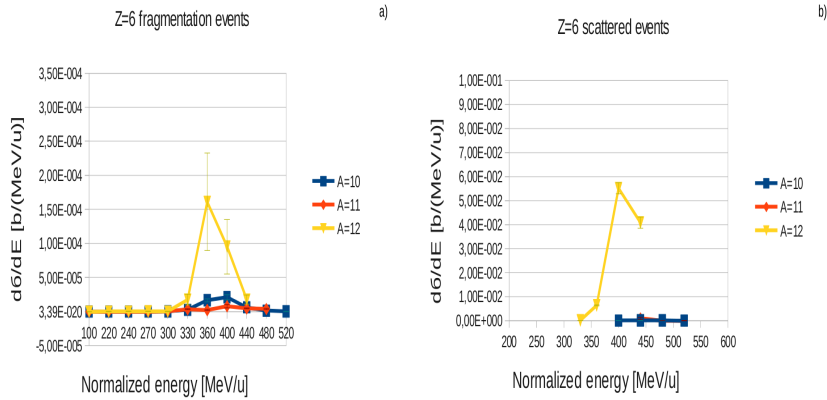

Figure 6.7: Single Differential Cross Sections $\frac{d\sigma^{Z=6}}{dE}(E)$ as a function of the normalized kinetic energy, for the Z=6 isotopes: A=10,11,12. Panel a shows the case of fragmented events, panel b the one of scattered events. The error bars take into account both the systematic and the statistic errors. For details see section "The cross section errors".

primary beam. This aspect is consistent with the hypothesis of a scattering process among the ^{12}C ions of the primary beam and the nuclei of the target. The scattering is elastic or inelastic: the second one can be due to meson

production and release of energy to the target nucleus. In the elementary reaction p-p, the elastic to inelastic cross section ratio is dominant and the same can be assumed in a first approximation for nuclei, taking into account that the charged meson production is not revealed in FIRST. Therefore, the scattered ^{12}C data are assumed to be elastically scattered carbon ions.

It must be remarked that an indication of the presence of elastic scattering has been discussed in chapter 3. In this chapter, dedicated to the TW calibrations, a smaller set of data was used to validate the calibrations.

The elastic scattering is mainly due to the single and multiple Coulomb scattering. Since both occur at small angles, their energy should be very close to the incident ^{12}C projectiles, due to kinematic laws. In figure 6.7, panel b, the energy has a maximum around 400 MeV/n and a FWHM around 60 MeV/n: such values are consistent with the Coulomb forward scatterings.

Moreover, by comparing figures 6.7 (panel b) and 6.3 it is possible to deduce that the Coulomb scattering is the dominant process (about 2 orders of magnitude larger) with respect to the fragmentation in the ion-ion interaction at 400 MeV/n.

Finally, it comes the discussion of ^{11}C and ^{10}C nuclides. They are, within the reliability of the experimental apparatus, heavy fragments that have lost 1 or 2 neutrons in the fragmentation process. The mechanism of this interaction looks similar to a "nuclear, single or double, stripping".

6.0.5   Final Remarks

The data discussed in this chapter are still preliminary and need some refinements.

A first improvement that is ongoing on the results, is the finalization of the systematic studies: in particular an enhancement is needed in the evaluation of the impact on the systematic errors of the match between the information of VTX and BM. Furthermore, studies are ongoing to test the ALADiN positioning and the magnetic field scale inside the magnet area. However, this contribution to the errors should be of minor impact.

Moreover, a huge effort is in progress within the FIRST collaboration to improve the data analysis with the aim of collecting a bigger statistic, by retrieving data, previously discarded. In fact, the very final goal of FIRST is the calculation of the Double Differential Cross Sections (DDCS) $\frac{d^2\sigma}{d\Omega dE}$, for each fragment type. This objective can be reached only if a sufficient statistic will be gathered to allow the evaluation of the DDCS in simultaneous intervals of energy and angle.

Nevertheless, even if improvements are still needed, the differential cross sections in angle and energy calculated until now supply a first rough information about:

1. the main ^{12}C-^{12}C interactions (fragmentation and scattering) at 400 MeV/n and their relative weights;

2. the distribution of the charges of the fragments:

3. the distributions of the fragments in polar angle;

4. the distributions of the fragments in energy;

5. the angular and energy distributions of the isotopes for each charge.

Even if a theoretical model is missing, the data can be used directly in the simulations with a good degree of reliability.

Chapter 7

Conclusions and outlooks

The experiment FIRST is carried out by an international collaboration including different countries: Italy, Germany, France and Spain. The experimental purpose is to investigate the effects of the ion fragmentation in their passage through matter. In particular, the main goal of the experiment is to extend the carbon fragmentation cross section databases. These experimental results are intensely needed for several reasons.

The main one is related to the understanding of the drawbacks of hadrontherapy in the tumor treatments. The use of hadrontherapy for curing deep seated tumors is increasing day by day. The advantage of this kind of therapy is the high accuracy of the dose deposition resulting from the physical properties of ions, in particular the carbon ones. Their radio-biological effectiveness, higher than the one of protons and γ, makes the hadrontherapy a better tool for cancer treatment. However, the main drawback in carbon therapy is related to the fragmentation reactions, which occur along the beam penetration path in the tissue. The fragmentation leads to the attenuation of the primary ion flux and to the build-up of secondary lower-charge fragments. This effect gives rise to the characteristic dose tail behind the Bragg peak. The alterations induced in the beam quality have to be considered in the Treatment Planning Systems (TPS) based on carbon beams. Another problematic aspect concerns the simulation codes. MC simulations are fundamental for TPSs because they must be used for accurate calculations of dose deposition. Nevertheless, this can be done only if they can achieve a very realistic description of the physical processes. They must take into account the effects due to the primary particles as well as to the secondary ones produced along the path in the matter. Nowadays, the real problem in MCs is that different codes produce simulations that differ up to an order of magnitude in their predictions. This is due to the fact that the accuracy of nucleus-nucleus interaction models, crucial in carbon ion therapy to have a

reliable prediction of the produced nuclear fragments, is not sufficiently high.
It has to be stressed that the cross section measurements performed, before
FIRST, in order to benchmark the reaction models were insufficient.
In addition, also the National Aeronautics and Space Administration (NASA)
is interested in evaluating the effects of the cosmic rays on human bodies from
the point of view of the nuclear fragmentation and to analyze the produced
damage onto the electronic circuits in space-crafts.
For these reasons, experiments able to fulfill the lack of information about
fragmentation cross sections, especially at high energies (400 MeV/n), are
really necessary.
The FIRST experiment performed measurements of fragmentation cross sec-
tions as a function of emission angles and kinetic energies of the fragments
and produced a data sample of several million collisions of ^{12}C ions impinging
on a thin carbon target. These were the first measurements ever made in an
experimental configuration involving carbon ion energy of 400 MeV/n.
In this thesis are presented the preliminary results obtained until now.
The results have been achieved after a careful work of data analysis divided
in several steps:

- calibration of all the detectors that form the experimental setup,

- implementation of the MC codes (that includes the parameters re-
  trieved from the calibrations) to simulate the experimental apparatus,
  in order to determine its efficiencies and acceptances,

- development of a reconstruction algorithm able to reconstruct the frag-
  ment path through the detector and to identify the fragmented ions
  together with their angular and energy distributions.

The plots of the single differential cross sections, as a function of the an-
gle with respect to the beam axis and of the normalized kinetic energy, for
the different measured charges, pointed out some important preliminary out-
comes. For what concerns the cross section as a function of the polar angle,
the production of fragments falls down exponentially with increasing angle,
except for the lighter isotopes (Z=1,2). These latter are spread out over the
whole angular acceptance of the experimental setup ($0 \leq \theta \leq 5$ degrees).
This result confirms that the lightest fragments are the main source of dose
scattering far from the original beam direction. The heavier ions, instead,
being more forward emitted, will essentially contribute to the dose deposition
close to the primary beam trajectory.
The cross sections as a function of the kinetic energy, instead, showed a peak
centered close to the beam energy (400 MeV/n). This confirms that the

greatest part of the detected particles comes from the projectile fragmentation, as expected.

Finally, the very detailed analysis performed on the data of this experiment, highlighted that a large fraction of the ^{12}C ion-ion interactions produce ^{12}C ions in the small angular range ($0 \leq \theta \lesssim 2$ degrees), with energy close to the one of the primary beam. Their origin is probably associated to elastic Coulomb Scattering, mainly single Coulomb Scattering. Also this process can play a major role in the hadrontherapy treatments.

Concluding, preliminary results about differential cross sections in an energy range not covered by the data previously available in literature, have been obtained. However, it has to be noted that the presented preliminary results refer to a small angular range, i.e. for $\theta < 5$ deg. The large angle data analysis is still on going. When the results of the two angular regions will be combined, the carbon fragmentation cross-sections at 400 MeV/n, with respect to energy and angle, will be accurately known, for the first time, in a wide angular range.

Looking at the future, the FIRST project foresees to perform measurements with different ion beams (He, Li) on different targets. In this way, the effects of different projectile fragmentation on other nuclei of human tissues will be investigated.

Appendix 1

Acronym List

In the following a list of the acronyms used in this thesis, with their meaning, is given, in alphabetical order.

ADC: Analog to Digital Converter
ALADiN: A LArge Dipole magNet
BM: Beam Monitor detector
BME: Boltzmann Master Equation
CAM: Computerized Anatomical Models
CFD: Costant Fraction Discriminator
CNS: Central Nervous System
CR: Cosmic Ray
DAQ: Data AcQuisition system
DDCS: Double Differential Cross Section
DDREF: Dose and Dose-Rate Effectiveness Factors
DSB: Double Strand Breaks
EMF: ElectroMagnetic Fluka
FIRST: Fragmentation of Ions Relevant for Space and Therapy experiment
FLUKA: FLUktuierende KAskade
GCR: Galactic Cosmic Ray
GSI: Gesellschaft für SchwerIonenforschung
GTC: Global Track Candidates
HIMAC: Heavy Ion Medical Accelerator
HZE: High charge (Z) and Energy particles
HZETRN: High charge (Z) and Energy TRaNsport code
IARC: International Agency for Research on Cancer
INFN: Istituto Nazionale di Fisica Nucleare
IR: Interaction Region
ISS: International Space Station

KENTROS: Kinetic ENergy and Time Resolution Optimized in Scintillator:
proton tagger detector
LEM: Local Effect Model
LET: Linear Energy Transfer
LINAC: LINear ACcellerator
LNF: Laboratori Nazionali di Frascati
LNS: Laboratori Nazionali del Sud
LoF: Length of Flight
LSS: Life Span Study
M26: Mimosa 26
MBS: Multi Branch System
MC: Monte Carlo
MIP: Minimum Ionizing Particle
NASA: National Aeronautics and Space Administration
NIRS: National Institute of Radiological Science
NSRL: NASA Space Radiation Laboratory
NTCP: Normal Tissue Complication Probability
OAR: Organs At Risk
OER: Oxygen Enhancement Ratio
PCB: Printed Circuit Board
PDF: Probability Density Function
PEANUT: PreEquilibrium Approach to NUclear Thermalization model
PET: Positron Emission Tomography
PMT: PhotoMultiplier Tube
PU: Pile-Up
QMD: Quantum Molecular Dynamics
QMSFRG: Quantum Multiple Scattering FRaGmentation
RBE: Relative Biological Effectiveness
rQMD: relativistic Quantum Molecular Dynamics model
SC: Start Counter detector
SCS: Single Coulomb Scattering
SDCS: Single Differential Cross Section
SEU: Single Event Upset
SF: Scoring Function
SiPM: Silicon PhotoMultiplier
SOBP: Spread Out Bragg Peak
SPE: Solar Particle Events
SSB: Single Strand Break
TCP: Tumor Control Probability
TDC: Time to Digital Converter
TLD: ThermoLuminescence Dosimeter

ToF: Time of Flight
TPS: Treatment Planning System
TRiP: TReatment Planning for particles code
TW: ToF-Wall detector
VC: Veto Counter detector
VTX: VerTeX detector

Appendix 2

Energy loss of a heavy charged particle passing through matter.
The Bethe-Bloch formula: a demonstration

A particle of charge ze and velocity $v = \beta c$ enters into a monoatomic material (the absorber), whose atomic and mass numbers are Z and A, respectively. In the following, the calculation of the energy, which is lost, in a unit path, during the passage through the absorber will be performed (following the approach of Segrè in [124]).

As a first step we consider the interaction of the particle with one single electron.

Two fundamental hypotheses must be taken into account in the analysis.

1. The particle interacts with the electron without changing appreciably neither its direction nor the modulus of its velocity, during the whole interaction time.
   This hypothesis is realistic because:

   a) the particle mass M is much greater than the electron mass m_e,

   b) the spatial distribution of the electrons is nearly uniform; therefore the attraction/repulsion of the particle-electron interactions occurs in all directions, maintaining the particle trajectory nearly straight.

2. The electron is supposed initially at rest, moreover it remains in the same position during the interaction and it just acquires energy from the particle; at the end of the interaction only, when the particle is far, the electron starts moving.

> This second hypothesis is reliable when the kinetic energy of the particle is high with respect to the energy of the atomic levels of the absorber.

Let us choose a cylindrical reference frame with the x-axis along the direction of the particle velocity v but with opposite orientation and with the origin on the particle itself (see figure 1). The plane perpendicular to x contains the radial and azimuthal coordinates r and θ. In this system the electron travels with a velocity v in modulus, along a trajectory parallel to x. The distance between the electron trajectory and the x-axis is called b. (This reference system is inertial since the particle velocity is assumed as constant.)
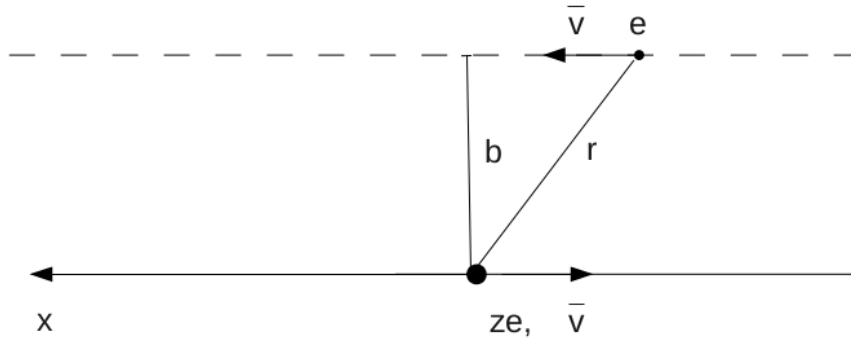

Figure 1: Sketch of the cylindrical reference frame considered in this calculation.

The electron acquires a momentum $\vec{p}$ as a consequence of the impulse generated by the particle electrostatic force on it.

$$\vec{p} = p_x\hat{i} = \int_{-\infty}^{\infty} e\vec{E}dt = \int_{-\infty}^{\infty}(eE_x\hat{i} + eE_T\hat{\lambda})dt \Rightarrow p = \int_{-\infty}^{\infty} eE_Tdt \quad (1)$$

The x component of the impulse in negligible when considering the above assumptions. In fact, in this case, the accelerations/decelerations along x before and after the minimum distance b compensate each others.
The time boundaries of the integral are assumed to be $\pm\infty$, however, in reality the electrostatic interaction vanishes quite early, at distances of about an atomic dimension (i.e. of the order of nm).
The infinitesimal time dt can be written as $dt = \frac{dx}{v}$, hence the impulse becomes:

$$p = \int_{-\infty}^{\infty} eE_T\frac{dx}{v} = \frac{e}{v}\int_{-\infty}^{\infty} E_Tdx \quad (2)$$

Again, the boundaries in x have been taken as $\pm\infty$ but actually the contribution after few nanometers becomes negligible. This feature of the electrostatic force is fundamental for the validity of the hypothesis of constant velocity. In fact, at infinite distance, the velocity surely changes but we consider the interaction as 0, beyond a distance of few nm.

In order to evaluate the integral given in equation 2, it is possible to apply the Gauss theorem to a cylindrical surface S, with axis along x, from $x = -\infty$ to $x = \infty$ and radius b (see figure 2).

$$\Phi_S(\vec{E}) = \frac{ze}{\epsilon_0} = \int_{-\infty}^{\infty} \vec{E} \cdot \vec{n} dS = \int_{S_B} 2\, E_x \hat{i} \cdot \hat{i} dS_B + \int_{S_L} E_T \hat{\lambda} \cdot \hat{\lambda} dS_L \qquad (3)$$

where S_B and S_L are the basis surfaces and the lateral surface of the cylinder, respectively. In equation 3, the basis surfaces are at $\pm\infty$, but the field (and in particular its x component) vanishes at such distances (actually an atomic distance is sufficient), therefore the term of the integral containing E_x disappears. Moreover, the infinitesimal lateral surface dS_L can be expressed as $2\pi b dx$.
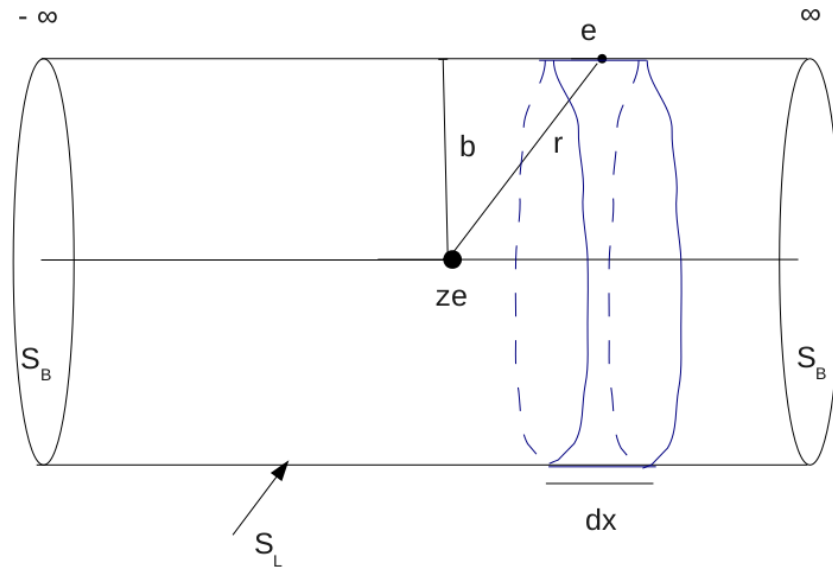

Figure 2: Sketch of the cylindrical surface used to apply the Gauss theorem for the equation 2 evaluation.

Equation 3 thus, becomes:

$$\Phi_S(\vec{E}) = \frac{ze}{\epsilon_0} = \int_{-\infty}^{\infty} E_T \hat{\lambda} \cdot \hat{\lambda}\, 2\pi\, bdx = 2\pi\, b \int_{-\infty}^{\infty} E_T\, dx \qquad (4)$$

since $\hat{\lambda} \cdot \hat{\lambda} = 1$.

From equations 2 and 4 it is possible to obtain:

$$p = \frac{ze^2}{2\pi b\epsilon_0 v} \Rightarrow \Delta E_k = \frac{p^2}{2m_e} = \frac{z^2 e^4}{8\pi^2 b^2 \epsilon_0^2 v^2 m_e} \tag{5}$$

ΔE_k is the kinetic energy acquired by the electron during the interaction with the particle; furthermore, ΔE_k is the energy lost by the particle also, because the field is conservative and the potential vanishes at long distances. Up to now, the energy loss of the particle is evaluated considering the interaction with a single electron only. This loss depends on the distance b (impact parameter).

However around the particle, several electrons are present, with density $n_e = \frac{N_e}{cm^3} \approx constant$. Inside the infinitesimal volume $dV = 2\pi b \, db \, dx$ of a crown of radius b, thickness db and length dx (see figure 3), the electron number is $n_e dV$.
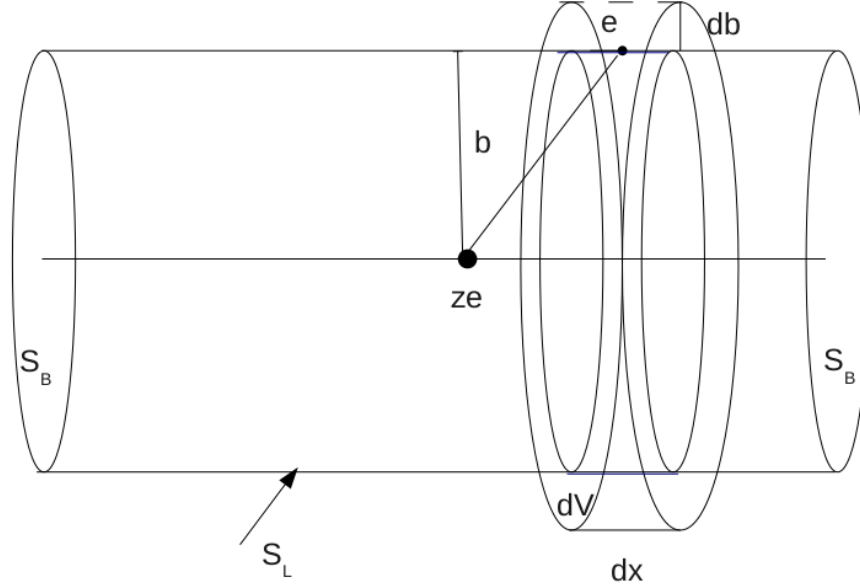

Figure 3: Sketch of the infinitesimal volume dV of the crown considered in the calculations.

The energy lost $d^2 E$ due to these electrons is given by:

$$d^2 E = \frac{p^2}{2m_e} * n_e * dV = \frac{z^2 e^4}{8\pi^2 b^2 \epsilon_0^2 v^2 m_e} * n_e * 2\pi b \, db \, dx = \frac{z^2 e^4}{4\pi b m_e \epsilon_0^2 v^2} * n_e \, db \, dx \tag{6}$$

Integrating over all the crowns, finally we get:

$$\frac{dE}{dx} = \frac{z^2 e^4}{4\pi m_e \epsilon_0^2 v^2} * n_e \int_{b_m}^{b_M} \frac{db}{b} = \frac{z^2 e^4}{4\pi m_e \epsilon_0^2 v^2} * n_e * ln(\frac{b_M}{b_m}) \qquad (7)$$

Both the boundaries b_M and b_m assume finite values and are related to the minimum and maximum energies, respectively, that the particle can transfer to the electron.

Let us define the electronic density n_e as a function of the atomic density n_{atoms}. The two quantities are directly proportional, with proportionality constant equal to the absorber atomic number Z. Therefore $n_e = Z * n_{atoms}$. Moreover, the atomic density is defined as $n_{atoms} = \frac{N_{atoms}}{V} = \frac{N_{Av}*n_{mol}}{V}$. N_{atoms} is the number of atoms contained in a volume V, N_{Av} is the Avogadro's number.

Since the number of moles is defined as $n_{mol} = \frac{m(g)}{A}$, the atomic density becomes $n_{atoms} = \frac{N_{Av}}{V} * \frac{m(g)}{A} = \frac{N_{Av}}{A} * \rho$. A and ρ are the absorber mass number and density.

In this way n_e can be written as: $n_e = Z * \frac{N_{Av}}{A} * \rho$.

By substituting the formula found for n_e in equation 7 and using the relationship $v = \beta c$, the energy loss turns to:

$$\frac{dE}{dx} = \frac{e^4 * N_{Av}}{4\pi m_e \epsilon_0^2 c^2} * \frac{z^2}{\beta^2} * \frac{Z}{A} * \rho * ln(\frac{b_M}{b_m}) \qquad (8)$$

Recalling that the classical electron radius is $r_e = \frac{e^2}{4\pi\epsilon_0 m_e c^2}$ it is possible to write:

$$\frac{dE}{dx} = 4\pi m_e c^2 * r_e^2 * N_{Av} * \frac{z^2}{\beta^2} * \frac{Z}{A} * \rho * ln(\frac{b_M}{b_m})$$

and calling k the term which collects all the constants i.e.
$k = 4\pi m_e c^2 * r_e^2 * N_{Av}$, the energy loss becomes:

$$\frac{dE}{dx} = k * \frac{z^2}{\beta^2} * \frac{Z}{A} * \rho * ln(\frac{b_M}{b_m}).$$

The evaluation of the integration boundaries, b_m and b_M, is a rather difficult task, because different phenomena occur depending on the energy range (low, intermediate or high range).

The commonly used formula for the term $ln(\frac{b_M}{b_m})$ is given by [27]:

$$ln(\frac{b_M}{b_m}) = \frac{1}{2}ln(\frac{2m_e c^2 * \beta^2 * \gamma^2 * T_{max}}{<I>^2}) - \beta^2 - \frac{\delta}{2} \qquad (9)$$

where $\gamma^2 = \frac{1}{1-\beta^2}$ takes into account the relativistic corrections; T_{max} represents the maximum energy transfer possible, from the particle to the electron, in a single collision; $<I>$ is the mean excitation energy of the absorber atoms and δ is a parameter giving the density-effect correction.

The energy loss in mixtures and compounds

The materials in which the energy loss of a particle occurs are not always made by pure elements but they can also be mixtures and compounds. In this case, it is anyway possible to think the mixtures/compounds as made up of thin layers of pure elements in the right proportion [27]. In these materials, the atomic and mass numbers Z and A must be changed to take into account the presence of different elements in the same material. Calling s_i the weight fraction of the i-th element in a compound or mixture, we have:

$$\sum_i s_i * Z_i$$

which is the number of electrons in the molecule of the mixture/compound and

$$\sum_i s_i * A_i$$

that is the molecular weight. The electronic density, fundamental in the evaluation of the energy loss, in case of compounds/mixtures, becomes:
$n_e = (\sum_i s_i * Z_i) * \frac{N_{Av}}{\sum_i s_i * A_i} * \rho$.
The other terms in the Bethe-Bloch formula do not vary significantly. The only exception is $< I >$, that is higher, in compounds, because the electrons are more tightly bound than in the free elements. In reference [125], tables, which report the $< I >$ values for different substances, are given.

Acknowledgements

The first person I want to thank, since he has been my mentor from the beginning of my Ph.D., is my tutor, professor Felice Iazzi.

Of course, together with him, I must thank all the people who worked with me, during these three years, in my group, for the teaching activity or working together for conferences or exams: Hannan Younis, Kanudha Sharda, Federico Scozzi, Cecilia Bennati. It was really a pleasure to spend time with you, working together but also sharing happy moments outside Politecnico. In particular, I really thank Riccardo Introzzi, who followed me every day from the beginning of my Ph.D., working side by side and always encouraging me. Without you these three years wouldn't have been the same. Thanks to you all my life will be better.

Since during the Ph.D. I have had the opportunity to work as a part of a scientific collaboration, I would like to especially thank those people who shared their experience and their time with me and who helped me in completing this Ph.D.. I would like to thank the group of the University "La Sapienza", in Rome: Vincenzo Patera, Alessio Sarti and Marco Toppi. All them welcomed me during my stays in Rome and working with them was really useful, but also enjoyable, for me. Moreover I want to thank the group of the Torino University: Dr Vincenzo Monaco and Abdul Haneefa Kummali. Many thanks also to all the people of the LNS in Catania, in particular to Stefania Tropea: working with you both in Torino and in Catania was really nice.

Finally the biggest thanks go to my family and to my friends, who always supported me with their love!

Bibliography

[1] American Cancer Society, "Global Cancer Facts & Figures 2nd Edition", Atlanta, (2011).

[2] International Atomic Energy Agency, "Relative biological effectiveness in ion beam therapy", jointly sponsored by the International Atomic Energy Agency and the International Commission on Radiation Units and Measurements. *Technical reports series* **461**, Vienna, (2008).

[3] R. Pötter, T. Auberger, A. Wambersie (Eds), "Hadrons A challenge for high-precision radiotherapy", *Strahlenther. Onkol.*, **175 Suppl. II**, (1999).

[4] A. Wambersie, R. Gahbauer, "Hadrons (protons, neutrons, heavy ions) in radiation therapy: Rationale, achievements and expectations", *Radiochem. Acta*, **89**, pp. 245 – 253, (2001).

[5] W.C. Röntgen,"Über eine neue Art von Strahlen." Vorläufige Mitteilung. *Sitzungsberichte der physikalisch-medicinischen Gesellschaft zu Würzburg*, **30**, pp. 132 – 141, (1895).

[6] W.D. Coolidge, "A powerful Röntgen ray tube with a pure electron discharge.", *Physical Review*, **2**, pp. 409–413, (1913).

[7] R.J. Van de Graaff, "A 1.500.000 volt electrostatic generator.", *Physical Review*, **38**, pp. 1919–1920, (1931).

[8] D.W. Kerst, "The acceleration of electrons by magnetic induction.", *Physical Review*, **60**, pp. 47–53, (1941).

[9] C.W. Miller, "Travelling-Wave Linear Accelerator for X-Ray Therapy", *Nature*, **171**, pp. 297–298, (1953).

[10] E.O. Lawrence, M.S. Livingston, "Production of high speed light ions without the use of high voltages", *Physical Review*, **40**, pp. 19–35, (1932).

[11] R. Wilson, "Radiological use of fast protons", *Radiology*, **47**, pp. 487–491, (1946).

[12] E. C. Halperin, "Particle therapy and treatment of cancer.", *Lancet Oncol.*, **7**, pp. 676–685, (2006).

[13] C. A. Tobias et al., "Radiological physics characteristics of the extracted heavy ion beams of the Bevatron.", *Science*, **174**, pp. 1131–1134, (1971).

[14] F. A. Cucinotta, M. Durante, "Cancer risk from exposure to galactic cosmic rays: implications for space exploration by human beings." *Lancet Oncol.*, **7**, pp. 431–435, (2006).

[15] Y. Hirao et al., "Heavy ion synchrotron for medical use - HIMAC project at NIRS - Japan", *Nuclear Physics A*, **538**, pp. 541–550, (1992).

[16] D. Schardt et al., "Tumor therapy with high-energy carbon ion beams", *Nuclear Physics A*, **787**, pp. 633c–641c, (2007).

[17] M. Jermann, "Particle Therapy Statistics in 2013", *International Journal of Particle Therapy*, **1, Issue 1**, (2014).

[18] ICRU Report 51, "Quantities and Units in Radiation Protection Dosimetry", International Commission on Radiation Units and Measurements (ICRU), Bethesda, (1993).

[19] M. Durante, J. S. Loeffler, "Charged particles in radiation oncology", *Nat. Rev. Clin. Oncol.*, **7**, pp. 37–43, (2010).

[20] E. B. Podgorsak et al., "Radiation oncology physics: a handbook for teachers and students", International Atomic Energy Agency, Vienna, (2005).

[21] U. Amaldi and M. Silari, "The Blue Book: the TERA Project and the Centre of Oncological Hadrontherapy", **I-II**, INFN-LNF, Frascati, Italy, (1995).

[22] W.H. Bragg, "On the α-particles of radium and their loss of range in passing through various atoms and molecules", *Philosophical Magazine*, **10**, pp. 318–340, (1905).

[23] D. Schardt et al., "Heavy-ion tumor therapy: Physical and radiobiological benefits", *Review of Modern Physics*, **82**, pp. 383–425, (2010).

[24] W.K. Weyrather, "Medical Applications of Accelerated Ions", *Lecture Notes in Physics*, **651**, pp. 469–490, (2004).

[25] H. Bethe, "Zur theorie des durchgangs schneller korpuskularstrahlen durch materie.", *Annalen der Physik*, **397(3)**, pp. 325–400, (1930).

[26] F. Bloch, "Bremsvermögen von Atomen mit mehreren elektronen", *Zeitschrift für Physik A: Hadrons Nuclei*, **81**, pp. 363–376, (1933).

[27] K.A. Olive et al. (Particle Data Group), "Review of Particle Physics", *Chin. Phys. C*, **38**, 090001 (2014).

[28] H. W. Barkas, *Nuclear Research Emulsions*, **1**, Academic Press New York and London, (1963).

[29] T. Elsässer et al., "The relevance of very low energy ions for heavy-iontherapy", *Physics in Medicine and Biology*, **54**, pp. 101–106, (2009).

[30] J.F. Ziegler, "Beam Interactions with Materials and Atoms", *Nuclear Instruments and Methods in Physics Research B*, pp. 1027–1036, (2004).

[31] P. V. Vavilov, "Ionizational losses of high energy heavy particles", *Zh. Eksp. Teor. Fiz.*, **32**, pp. 920–923, (1957).

[32] S. P. Ahlen, "Theoretical and experimental aspects of the energy loss of relativistic heavily ionizing particles", *Review of Modern Physics*, **52**, pp. 121–173, (1980).

[33] G. Molière, "Theorie der Streuung schneller geladener Teilchen II, Mehrfach-und Vielfachstreuung", *Z. Naturforschung A*, **3A**, pp. 78–97, (1948).

[34] H. A. Bethe, "Moliere's theory of multiple scattering", *Physical Review*, **89(6)**, pp. 1256–1266, (1952).

[35] B. Gottschalk et al., "Multiple Coulomb Scattering of 160 MeV Protons", *Nuclear Instruments and Methods*, **B74**, pp. 467–490, (1992).

[36] Y. S. Tsai, "Pair production and bremsstrahlung of charged leptons", *Review of Modern Physics*, **46**, pp. 815-851, (1974).

[37] G. Kraft, "Tumor therapy with heavy charged particles", *Progress in Particle and Nuclear Physics*, **45**, pp. S473–S544, (2000).

[38] U. Amaldi and G. Kraft, "Radiotherapy with beams of carbon ions", *Report on Progress in Physics*, **68**, pp. 1861–1882, (2005).

[39] T. Kanai et al., "Biological and physical proposal for a heavy-ion clinical trial", *Proc. 3rd Workshop on Physics Biological Research with Heavy Ions (2-3 September 1993)*, **NIRS M 99, HIMAC 006**, pp. 7–11.

[40] E. Hall, "Radiobiology for the Radiologist", 5th ed., (Lippincott Williams and Wilkins), Philadelphia, (2000).

[41] D.L. Bailey et al., "Positron Emission Tomography: Basic Sciences.", (Secaucus, NJ: Springer-Verlag), (2005).

[42] R. Serber, "Nuclear reactions at high energies", *Physical Review*, **72**, pp. 1114–5, (1947).

[43] J. J. Bevelacqua, "Systematics of heavy ion radiotherapy", *Radiation Protection managment*, **22**, pp. 4–13, (2005).

[44] S. Kox et al., "Trends of total reaction cross sections for heavy ion collisions in the intermediate energy range", *Physical Review*, **C35**, p. 1678, (1987).

[45] M. Krämer, "Swift ions in radiotherapy - Treatment planning with TRiP98", *Nuclear Instruments and Methods in Physics Research B*, **267**, pp. 989-992, (2009).

[46] M. Krämer and M. Durante, "Ion beam transport calculations and treatment plans in particle therapy", *The European Physical Journal*, **D60**, p. 195, (2010).

[47] L. Sihver and D. Mancusi, "Present staus and validation of HIBRAC", *Radiation Measurements*, **44**, p. 38, (2009).

[48] D. Schardt et al., "Precision Bragg-curve measurements for light ion beams in water", *GSI-Report*, **373**, (2008).

[49] G. Battistoni et al., "The FLUKA code: description and benchmarking", *Proceedings of the Hadronic Shower Simulation Workshop 2006, AIP Conference Proceedings*, **896**, p. 31, (2007).

[50] S. Agostinelli et al. (Geant4 Collaboration), "GEANT4 – A simulation toolkit", *Nuclear Instruments and Methods*, **506**, pp. 250–303, (2003).

[51] J. Allison et al. (Geant4 Collaboration), "Geant4 Developments and Applications", *IEEE Transactions On Nuclear Science* **53**, pp. 270–8, (2006).

[52] A. Mairani, "Nucleus-nucleus interaction modelling and applications in ion therapy treatment planning", Ph.D. Thesis, University of Pavia, (2007).

[53] F. Sommerer et al., "Investigating the accuracy of the FLUKA code for transport of therapeutic ion beams in matter", *Physics in Medicine and Biology*, **51**, pp. 4385–98, (2006).

[54] I. Pshenichnov et al., "Nuclear fragmentation reactions in extended media studied with Geant4 toolkit", *Nuclear Instruments and Methods B*, **268**, pp. 604–15, (2010).

[55] J.H. Heinbockel et al., "Comparison of the transport codes HZETRN, HETC and FLUKA for a solar particle event", *Advances in Space Research*, **47**, pp. 1079-1088, (2011).

[56] M. Krämer and M. Scholz, "Treatment planning for heavy ion therapy", *Phys. Med. Biol.*, **45**, pp. 3319–30, (2000).

[57] O. Jäkel, "Treatment planning for heavy ion radiotherapy: Clinical implementation and application", *Physics in Medicine and Biology*, **46**, pp. 1101–1116, (2001).

[58] G.A.P. Cirrone et al., "A 62-MeV Proton Beam for the Treatment of Ocular Melanoma at Laboratori Nazionali del Sud-INFN", *IEEE Transactions On Nuclear Science*, **51**, pp. 860–865, (2004).

[59] S. Rossi and R. Orecchia, "The National Centre of Oncological Hadrontherapy (CNAO) project", *Rivista Medica*, **14 N.1**, pp. 69–79, (2008).

[60] C. Agodi et al., "The INFN TPS project", *Il Nuovo Cimento 31*, **1**, pp. 99–108, (2008).

[61] M. Durante and F. A. Cucinotta, "Physical basis of radiation protection in space travel", *Reviews of Modern Physics*, **83**, pp. 1245–1281, (2011).

[62] R. J. White and M. Averner, *Nature*, **409**, p. 1115, (2001).

[63] NASA, NASA/SP-2004-6113, (2005).

[64] http://humanresearchroadmap.nasa.gov/.

[65] NASA, NASA/SP-2009-3405, (2009).

[66] NASA, (NASA HQ, Washington, DC), (1998).

[67] W. Schimmerling, J. Wilson, F. Cucinotta and M. Kim, "Requirements for Simulating Space Radiations with Particle Accelerators", (Kodansha Scientific Ltd., Tokyo), p. 1, (1999).

[68] M. Durante and F. A. Cucinotta, *Nat. Rev. Cancer*, **8**, p. 465, (2008).

[69] J. W. Wilson et al., *Health Phys.*, **68**, p. 50, (1995).

[70] NCRP, Report No. 132 (NCRP, Bethesda, MD), (2000).

[71] ESA, "Investigation on Biological Effects of Space Radiation (IBER) Study", *Final Report ESA publication*, **CR-P-4585**, (2006).

[72] M. Maalouf, M. Durante and N. Foray, *J. Radiat. Res.*, **52**, p. 126, (2011).

[73] P. Dodd et al., *IEEE Trans. Nucl. Sci.*, **54**, p. 2303, (2007).

[74] L. W. Connell et al., *IEEE Trans. Nucl. Sci.*, **43**, p. 2814, (1996).

[75] S. Metzger et al., "Investigation of Single Event Effects with Very High Energy Ions", *GSI Report No. 2011-1*, p. 1438, (2011).

[76] J. Pellish et al., *IEEE Trans. Nucl. Sci.*, **57**, p. 2948, (2010).

[77] ICRP, Publication 103. Ann. ICRP 37, (2007).

[78] M. Durante and C. Bruno, *Eur. Phys. J. D*, **60**, p. 215, (2010).

[79] ESA, "HUMEX: Study on the Survivability and Adaptation of Humans to Long-Duration Interplanetary and Planetary Environments", Report No. ESA-ESTEC SP-1264, (2003).

[80] F. A. Cucinotta et al., *Space Weather*, **8**, S00E09, (2010).

[81] U. Straube et al., *Acta Astronaut.*, **66**, p. 963, (2010).

[82] M. P. Billings, W. R. Yucker, and B. R. Heckman, "Body Self-Shielding Data Analysis", (McDonald Douglas Astronautics Company West), MDC-G4131, (1973).

[83] W. Atwell, *Adv. Space Res.*, **14**, p. 415, (1994).

[84] G. Reitz et al., *Radiat. Res.*, **171**, p. 225, (2009).

[85] J. Wilson et al., "Transport Methods and Interactions for Space Radiations", *NASA RP*, **1257**, (1991).

[86] F. A. Cucinotta, M. Y. Kim and L. Ren, *Radiation Measurements*, **41**, p. 1173, (2006).

[87] F. A. Cucinotta et al., *Radiat. Meas.*, **32**, p. 18, (2000).

[88] F. A. Cucinotta et al., *Radiat. Res.*, **170**, p. 127, (2008).

[89] M. S. Clowdsley et al., *Physica Medica*, **17**, p. 94, Supplement 1, (2001).

[90] S. R. Blattnig et al., "MESTRN: A Deterministic Mesons-Muon Transport Code for Space Radiation", *NASA Technical Report No. TM-2004-212995*, (National Aeronautics and Space Administration, Washington, DC), (2004).

[91] K. Niita et al., *Radiation Measurements*, **41**, p. 1080, (2006).

[92] I. Plante and F. A. Cucinotta, *New J. Phys.*, **10**, 125020, (2008).

[93] I. Plante and F. A. Cucinotta, *New J. Phys.*, **11**, 063047, (2009).

[94] M. Krämer and G. Kraft, *Radiat. Environ. Biophys.*, **33**, p. 91, (1994).

[95] M. Rudd, "HZE Interactions in Biological Materials", (NASA CP 3360), (1997).

[96] F. A. Cucinotta, I. Plante, A. Ponomarev and M. Y. Kim, *Radiation Protection Dosimetry*, **143**, p. 384, (2011).

[97] J. H. Heinbockel et al., *Adv. Space Res.*, **47**, p. 1089, (2011).

[98] M.C. Morone et al., "Monte Carlo simulation to evaluate the contamination in an energy modulated carbon ion beam for hadron therapy delivered by cyclotron", *Physics in Medicine and Biology*, **53**, p. 6045, (2008).

[99] R. Pleskac et al., "The FIRST Experiment at GSI", *Nucl. Instr. Methods in Phys. Res. A*, **687**, p. 130, (2012).

[100] J. Hubele et al.,"Fragmentation of gold projectiles: from evaporation to total disassembly", *Zeitschrift fur Physik A*, **340**, p. 263, (1991).

[101] A. Ferrari, P.R. Sala, A. Fasso, J. Ranft, "FLUKA: A Multi Particle Transport Code", *Technical Report CERN-2005-10*, INFN/TC05/11, SLAC-R-773, (2005).

[102] Z. Abou-Haidar et al., "Performance of upstream interaction region detectors for the FIRST experiment at GSI", *Journal of Instrumentation*, **7**, P02006, (2012).

[103] E. Spiriti, M. De Napoli, F. Romano et al., "The FIRST experiment: interaction region and MAPS vertex detector", *Nuclear Physics B - Proceedings Supplements*, **215**, Issue 1, pp. 157-161, (2011).

[104] http://www.iphc.cnrs.fr/-CMOS-ILC-.html

[105] M. De Napoli et al., "The KENTROS Detector for Identification and Kinetic Energy Measurements of Nuclear Fragments at Polar Angles Between 5 and 90 Degrees", *IEEE MIC*, (2012)

[106] A. Schuttauf et al., "Universality of spectator fragmentation at relativistic bombarding energies", *Nuclear Physics A*, **607**, p. 457, (1996)

[107] H.G. Essel, N. Kurz, "The general purpose data acquisition system MBS", *IEEE Transactions on Nuclear Science*, **47 (2)**, p. 337, (2000).

[108] J.B. Birks, "The Theory and Practice of Scintillation Counting.", (London: Pergamo), (1964).

[109] R. L. Burden, J. D. Faires, "Numerical Analysis (3rd ed.)", (PWS Publishers), (1985).

[110] E. Rutherford, "The Scattering of α and β rays by Matter and the Structure of the Atom", *Philos. Mag.*, **6**, p. 21, (1911).

[111] T.T. Böhlen et al., "Benchmarking nuclear models of FLUKA and GEANT4 for carbon ion therapy", *Physics in Medicine and Biology*, **55 (19)**, p. 5833, (2010).

[112] M.B. Chadwick et al., "ENDF/B-VII.1 Nuclear Data for Science and Technology: Cross Sections, Covariances, Fission Product Yields and Decay Data", *Nuclear Data Sheets*, **112, issue 12**, pp. 2887–2996, (2011).

[113] T. Fukahori et al., "JENDL High Energy File", *Journal of Nuclear Science and Technology*, **2**, pp.25-30, (2002).

[114] G. Battistoni et al., "Hadron production simulation by FLUKA", *Journal of Physics: Conference Series*, **408**, (2013).

[115] V. Andersen et al., "The FLUKA code for space applications: recent developments", *Advances in Space Research*, **34**, pp. 1302–10, (2004).

[116] H. Sorge, H. Stocker and W. Greiner, "Relativistic Quantum Molecular Dynamics Approach to Nuclear Collisions at Ultrarelativistic Energies", *Nuclear Physics A*, **498**, pp. 567c-576c, (1989).

[117] F. Cerutti, G. Battistoni et al., "Low energy nucleus-nucleus reactions: the BME approach and its interface with FLUKA", *Proc. 11th Int. Conf. on Nucl. React. Mech.*, pp. 507–11, (2006).

[118] J. Aichelin, "Quantum molecular dinamics - A dynamical microscopic n-body approach to investigate fragment formation and the nuclear equation of state in heavy ion collisions", *Physics reports (Review Section of Physics Letters)*, **202**, pp. 233–360, (1991).

[119] M. Cavinato et al., "Boltzmann master equation theory of angular distributions in heavy-ion reactions", *Nuclear Physics A*, **643**, p. 15, (1998).

[120] R.K. Tripathi, F.A. Cucinotta and J.W. Wilson, "Accurate universal parameterization of absorption cross-sections III-light systems", *Nuclear Instruments and Methods B*, **155**, pp. 349–56, (1999).

[121] http://root.cern.ch/drupal/content/about.

[122] C. Sfienti et al., "Mass and Isospin Effects in Multifragmentation", *Nuclear Physics A*, **749**, pp. 83c–92c, (2005)

[123] R.D. Woods, D.S. Saxon, "Diffuse Surface Optical Model for Nucleon-Nuclei Scattering", *Physical Review*, **95 (2)**, pp. 577–578, (1954).

[124] E. Segrè, "Nuclei e particelle", (Zanichelli, Bologna), (1966).

[125] R.M. Sternheimer, S.M. Seltzer and M.J. Berger, "The Density Effect for the Ionization Loss of Charged Particles in Various Substances", *Atomic Data and Nuclear Data Tables*, **30**, p. 261, (1984).